Dissertation
submitted to the
Combined Faculties for the Natural Sciences and for Mathematics
of the Ruperto-Carola University of Heidelberg, Germany
for the degree of
Doctor of Natural Sciences

presented by

Falco Krüger, Master of Science (M.Sc.)

born in: Pasewalk

Oral-examination: 8th September 2017

Vacuole biogenesis in *Arabidopsis thaliana*.

Referees: Prof. Dr. Karin Schumacher

Prof. Dr. Jan U. Lohmann

At the last dim horizon, we search among ghostly errors of observations for landmarks that are scarcely more substantial. The search will continue. The urge is older than history. It is not satisfied and it will not be oppressed.

Edwin Hubble

Table of Contents

Zusammenfassung

Alle höheren Pflanzen bilden Blätter und Wurzeln, Organe die darauf spezialisiert sind Kohlenstoffdioxid zu binden, Energie aus dem Sonnenlicht zu absorbieren und Wasser sowie Mineralien aufzunehmen. Diese Gewebe haben in der Regel eine große Oberfläche, die aus großen Zellen aufgebaut ist. Um diesen Raum möglichst ressourcenschonend auszufüllen, haben Pflanzenzellen einzigartige Kompartimente entwickelt, zentrale Vakuolen, die fast das gesamte Zellvolumen einnehmen können. Der Transport von Wasser in die Vakuolen ist viel ökonomischer als eine vergleichbare Menge an Zytosol zu erzeugen. Dadurch werden die Stoffwechselkosten des Pflanzenwachstums erheblich gesenkt. Neben der Funktion als Wasserreservoir, spielen Vakuolen auch eine zentrale Rolle bei der Speicherung von Nährstoffen und Sekundärmetaboliten, der Entgiftung des Zytosols und dem Abbau von sowohl endozytiertem als auch autophagischen Material. Der Großteil der Forschung konzentrierte sich bisher vor allem auf die physiologischen Funktionen von Vakuolen, aber detaillierte Kenntnisse darüber, wie sie sich entwickeln, sind begrenzt. Aufgrund der enormen Kompartimentgröße ist Vakuolenbiogenese in Pflanzen nicht nur eine Frage der Balance zwischen ankommenden Vesikeln und Membranumsatz, sondern erfordert außerdem enorme Membranmengen, um überhaupt eine ausreichende Vakuolenexpansion zu ermöglichen, vor allem während des Zellwachstums. Das aktuelle Modell besagt, dass zentrale Vakuolen durch das Verschmelzen von mehreren kleinen Vakuolen entstehen, die anfänglich aus einer Kombination von späten Endosomen und Autophagie gebildet wurden. Allerdings wurden diese mechanistischen Details vor allem aus zweidimensionalen elektronenmikroskopischen Aufnahmen abgeleitet und beinhalten keine Quantifizierung. In dieser Arbeit haben wir die Biogenese von lytischen Vakuolen in Wurzelspitzen von *Arabidopsis thaliana* im Detail analysiert. Durch die Berechnung von dreidimensionalen Oberflächenmodellen von Vakuolen rekonstruierten wir ihre komplexen röhrenförmigen Netzwerke in meristematischen Zellen und entdeckten, dass sich Vakuolen entgegen dem existierenden Modell als ein einziges zusammenhängendes Kompartiment entwickeln. Dies wurde durch "Fluorescence Recovery After Photobleaching" (FRAP) -basierte Messungen von Vakuolenvolumen weiter untermauert. Anstatt durch Verschmelzung von kleineren Volumina zu wachsen, blasen sich Vakuolen im Laufe der Zeit vielmehr auf, bis sie ihre endgültige Größe und Form in differenzierten Zellen erreichen. Dennoch fanden wir heraus, dass diese Vakuolenentwicklung entscheidend von der durch CORVET / HOPS -vermittelten Membranfusion abhängt, was durch stark fragmentierte Vakuolen bei induziertem Knockdown der strukturellen Untereinheit VPS16 gezeigt wurde. Außerdem ergab die

Berechnung der Anzahl und Lebensdauer von späten Endosomen in sich streckenden Zellen, dass ihr Membranbeitrag nicht die beobachtete Wachstumsrate von Vakuolen zulässt, was auf einen zusätzlichen Membranzulieferer hindeutete. Diesen haben wir über einen bislang unentdeckten Transportweg identifiziert, der V-ATPasen und V-PPasen über ein intermediäres Kompartiment, welches wir als Provokuole bezeichnet haben, an den Tonoplasten liefert. Durch die Verwendung unterschiedlicher genetischer und chemischer Verfahren, um bekannte vakuoläre Transportwege zu blockieren, haben wir festgestellt, dass der Provokuolentransport Golgi- und Post-Golgi Kompartimente umgeht und weder COPII-vermittelten Export aus dem ER noch die Autophagie-Maschinerie erfordert. Vor allem haben wir mit einem maßgeschneiderten, induzierbaren Expressionssystem und mithilfe von dreidimensionaler konfokaler Hochauflösungs-Laser-Scanning-Mikroskopie berechnen konnten, dass Provokuolen bei der Zellstreckung den Großteil des benötigten Tonoplastenmaterials liefern. Mit den in dieser Arbeit präsentierten Ergebnissen wird das Modell der Vakuolenbiogenese in *Arabidopsis thaliana* neu definiert.

Summary

All higher plants form leaves and roots, organs specialized to efficiently absorb carbon dioxide, collect energy from the sunlight and take up water as well as minerals. These tissues usually have a large surface area made up of big cells. To fill the space most resourcefully plant cells developed unique compartments, central vacuoles, which can occupy almost the entire cell volume. The transport of water into vacuoles is much more economical than to generate a similar amount of cytosol, decreasing the metabolic cost of plant growth substantially. Besides, vacuoles fulfill vital functions in storage of nutrients, detoxification of the cytosol, and protein degradation. The physiological roles of vacuoles are well studied but detailed knowledge about how they develop is limited. Due to their gigantic size vacuole biogenesis in plants is not only a matter of balancing incoming vesicle trafficking and membrane turnover, but also requires enormous amounts of membrane in order to enable proper vacuole expansion. The consensus model states that central vacuoles arise by fusion of multiple small organelles, initially formed by a combination of late endosomes and autophagy. However, the mechanistic details are mostly reasoned from 2D electron microscopy images and lack any quantification. In this thesis we analyzed the biogenesis of lytic vacuoles in root tips of *Arabidopsis thaliana* in more detail. By computing 3D surface renderings of vacuoles we reconstituted their complex tubular network in meristematic cells and discovered that in contrast to the existing model vacuoles develop as a single compartment. This was further substantiated by FRAP-based measurements of vacuolar volumes. Instead of growing by fusion of smaller volumes vacuoles inflate over time until they reach their final size in differentiated cells. Still, we found that vacuole development depends on CORVET/HOPS mediated membrane fusion as indicated by vacuole fragmentation upon induced knockdown of the subunit VPS16. Also, calculating the number and lifetime of late endosomes in elongating cells revealed that their membrane contribution does not allow for the growth rate of vacuoles, suggesting an additional membrane donor. We identified a so far undiscovered pathway that delivers V-ATPases and V-PPases to the tonoplast via an intermediate compartment we termed provacuole. By using different genetic and chemical means to block known vacuolar transport routes we found that provacuole trafficking bypasses Golgi and post-Golgi compartments and does neither require COPII-mediated ER export nor the core autophagy machinery. Most importantly, with a custom-built inducible expression system and 3D super-resolution confocal laser scanning microscopy we were able to calculate that in elongating cells provacuoles provide the majority of the required tonoplast material. In conclusion, the evidence provided in this thesis redefines the model of vacuole biogenesis in *Arabidopsis thaliana*.

Contribution to this work

The author declares that this work was written independently only with the sources indicated and not by services of a third party. Where the work of others has been quoted or reproduced, the source is always given.

Parts of the results which are presented have been published before (Viotti et al., 2013).

The introduction of this thesis was written independently and served as template (including Figure 3) for a review article entitled "Vacuole biogenesis in *Arabidopsis thaliana*" submitted to the journal "Seminars in Cell and Developmental Biology". The authors of this article are Falco Krüger and Prof. Dr. Karin Schumacher.

Apart from the author and the supervisor the following persons contributed to the work presented in this thesis.

Quantification of MVB/LE number per cell: with Taslima Nahar (under supervision).

CLSM time lapse imaging of elongating root tips: Dr. Melanie Krebs.

Crossing and generation of VHA-a3-mRFP VHA-a1-GFP in *gnl1*;GNL1 BFA-sens.: Fabian Fink and Beate Schöfer.

Crossing of VHA-a3-GFP in *pat2-2*: Dr. Corrado Viotti, Beate Schöfer.

Sample preparation and imaging for EM and IEM experiments: with Steffi Gold, Dr. Corrado Viotti and Dr. Stefan Hillmer.

Cloning of DEX-inducible VHA-a3-mCherry and transformation into VHA-AP2-GFP in *vha-a2 vha-a3*: Philipp Bellon (cloning, under supervision) and together with Jana Christin Askani.

Cloning of DEX-inducible amiR-*vps16*: with Taslima Nahar (under supervision).

Crossings of DEX-inducible amiR-*vps16* with VHA-a3-mRFP and VHA-a3-mRFP VMA21-GFP: together with Jana Christin Askani.

Introduction

Plants are sessile organisms that form specialized organs to explore their environment. Leaves are extensive flat sheets that collect sunlight and absorb carbon dioxide for photosynthesis. Roots are highly branched networks of tubes within the soil that take up water, ions and nutrients. Simply put, the bigger the surface of these organs the better plants can adapt to environmental stresses. To effectively balance the cost-benefit ratio of a large surface area, plant tissues are formed with a comparatively small number of big cells instead of a high number of small cells. In contrast to yeast and animal cells, plant cells on average grow much larger. This difference in both volume and surface area is directly reflected in the size of the contained vacuoles (Figure 1). Central vacuoles are the economic masterpiece that allow to fill vast cell volumes with minimal metabolic effort as compared to synthesizing the same amount of cytosol.

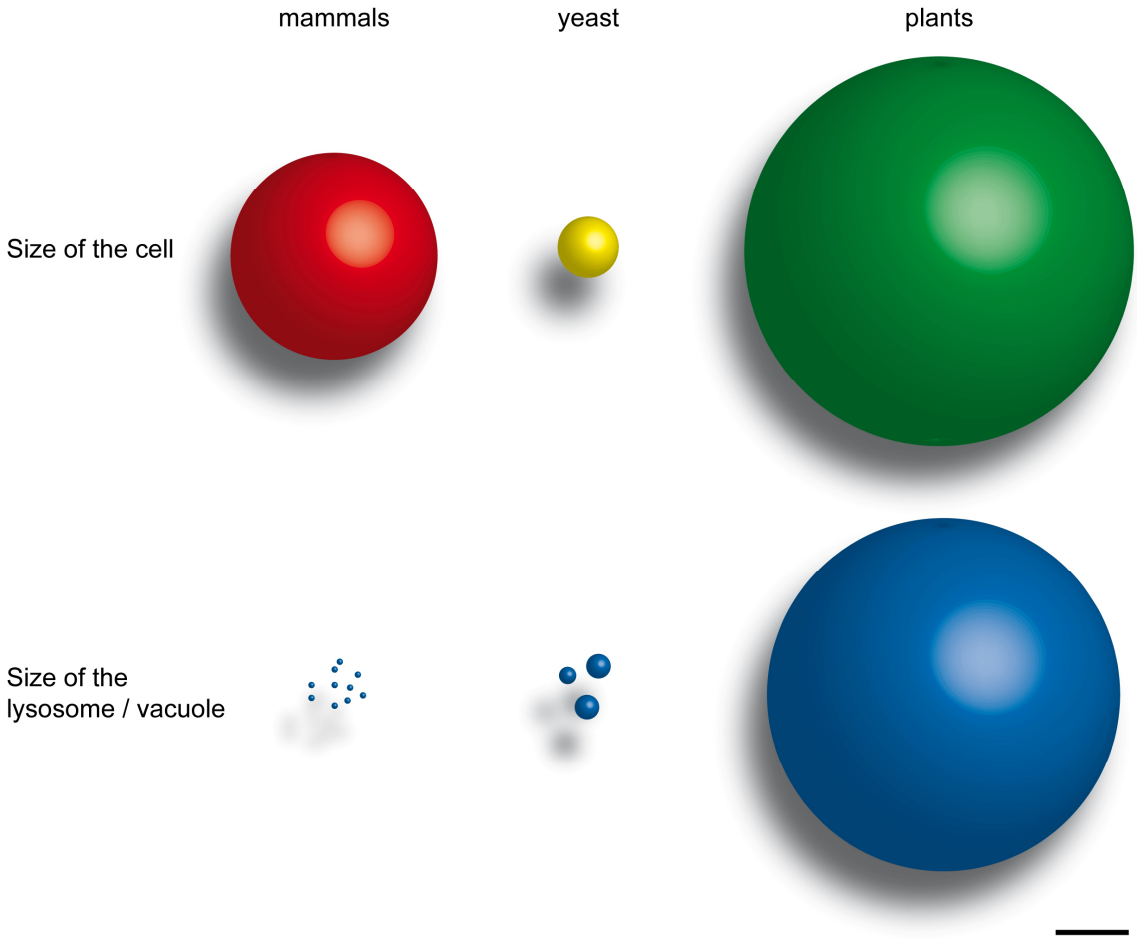

Figure 1: Schematic representation of typical cell sizes as well as the contained lysosomes / vacuoles of mammals, yeast and plants. For better comparability all bodies are depicted as spheres. Relative differences of individual lysosomes / vacuoles in volume (V) and surface area (A_O) are given (arrows). The scale bar indicates 10 µm.

Plant vacuoles can be roughly grouped into two different classes, protein storage vacuoles (PSV) and lytic vacuoles (LV). PSVs exist temporarily; they form during embryogenesis and provide energy throughout germination. LVs share the important lytic function with vacuoles of algae, yeast, and lysosomes in animal cells and are important during the whole plant lifecycle. In addition to many vital functions such as storage of nutrients and secondary metabolites, cytosol detoxification, and protein degradation vacuoles also play a mechanic role. Stomata movement relies on drastic but reversible morphological changes of vacuoles whereby plants can regulate gas exchange and transpiration in response to environmental stimuli. Together with the cytoplasm, vacuoles also create a certain cell-internal pressure, i.e. turgor, which in combination with the rigid cell walls provide hydrostatic stiffness to the whole plant.

The discovery of vacuoles

In 1776, Spallanzani described star-like structures in protozoa that were constantly inflating and deflating which was why he mistakenly assumed to look at respiratory organs (Spallanzani, 1776). These "opuscoli", in fact contractile vacuoles, were the first vacuoles ever described. In plant cells though, vacuoles remained unnoticed for many decades. This seems surprising, since vacuoles can take up such vast volumes in plant cells. However, biologists of the 18th and early 19th century were far more fascinated by cellular processes like cytoplasmic streaming. Interestingly, very detailed illustrations of this process in plant cells clearly outlined big empty areas within the cells along which the cytoplasm was flowing (Meyen, 1938). It was Felix Dujardin who first used the term "vacuole" (from Latin *vacuus* for "empty") to describe the allegedly void spaces within cells (Dujardin, 1841). One year later, Schleiden applied this term to plant cells in order to discriminate between cytoplasm and cell sap (Schleiden, 1842). Hugo deVries was the first scientist to discover and investigate the osmotic properties of vacuoles and realized that they are surrounded by a semi-permeable membrane which he later called tonoplast (deVries, 1877, 1885). By that time it was clear that vacuoles are not at all empty spaces but cellular organelles containing a mixture of different fluids and compounds. However, early studies investigating vacuoles were purely descriptive as there was nothing known about their cellular function but already back then the question came up where vacuoles originate from.

The biogenesis of vacuole biogenesis

At the end of the 19th century it was the general idea that vacuoles arise *de novo* when there is just enough water present in the cytoplasm to form distinct droplets. In contrast to this, deVries argued that vacuoles develop from special plastid-like precursors,

"tonoplasts", which can subdivide to form new organelles if necessary. By taking up water the tonoplasts would inflate and become vacuoles (deVries, 1885). In 1888, Went proposed that all plant cells contain vacuoles and thus always originate from already existing vacuoles by division (Went, 1888). However, this idea did not win much recognition after it was shown that vacuoles formation can be experimentally induced *de novo* (Pfeffer, 1890).

Studies of intact plant roots demonstrated that in meristematic cells several small tubular vacuoles are present (Bensley, 1910). Moreover, Bensley (1910) showed that vacuoles can increase in size and fuse to form big central vacuoles. In the following years many plant cell biologists preferably investigated intact tissues and made use of the natural coloring of vacuoles in flower petals e.g. by tannins and anthocyanins. Additionally, the discovery of vital stains, especially Neutral red, allowed scientists to study also early stages of vacuole biogenesis. Between 1914 and 1933 Guilliermond as well as P.A. and P. Dangeard (father and son) described the morphological development of vacuoles in different plant species. Their studies confirmed vacuoles to be present already in the earliest meristematic cells and revealed that they develop from small spherical, rod-like or tubular compartments into large central vacuoles present in differentiated cells (Guilliermond, 1929, reviewed in Zirkle, 1937). Furthermore, they observed that vacuoles, especially in meristematic cells, are very dynamic organelles that not only constantly change their morphology, but also fragment and fuse again due to cytoplasmic streaming. They further observed the transition of lytic vacuoles into protein storage vacuoles in maturing seeds and the reversed process during germination (Dangeard, 1923; Guilliermond, 1929, 1941). In fact, during this developmental stage lytic vacuoles and protein storage vacuoles do exist simultaneously (Zheng and Staehelin, 2011).

Biogenesis of vacuoles/lysosomes in yeast and mammals

As in plant cells, lysosomes in mammalian cells and vacuoles of yeast represent the final destination for several endosomal trafficking pathways. They generate a variety of Golgi and post-Golgi derived vesicles, late endosomes and autophagosomes which fuse with the vacuole/lysosome. Their boundary membrane becomes part of the vacuolar membrane thus contributing to its expansion. In the end, trafficking towards the vacuole/lysosome facilitates its biogenesis. On top of that, next to heterotypic fusion, vacuoles can also undergo homotypic fusion. Regardless from which trafficking route membrane material arrives, the order of events and the required fusion machinery seems to be largely conserved among eukaryotes and is best studied in mammals and

yeast (reviewed in Wickner, 2010; Balderhaar and Ungermann, 2013; Kümmel and Ungermann, 2014; Guerra and Bucci, 2016). According to the yeast model system, the donor membrane and acceptor membrane are first reversibly tethered, followed by membrane docking before membrane fusion finally occurs (Figure 2).

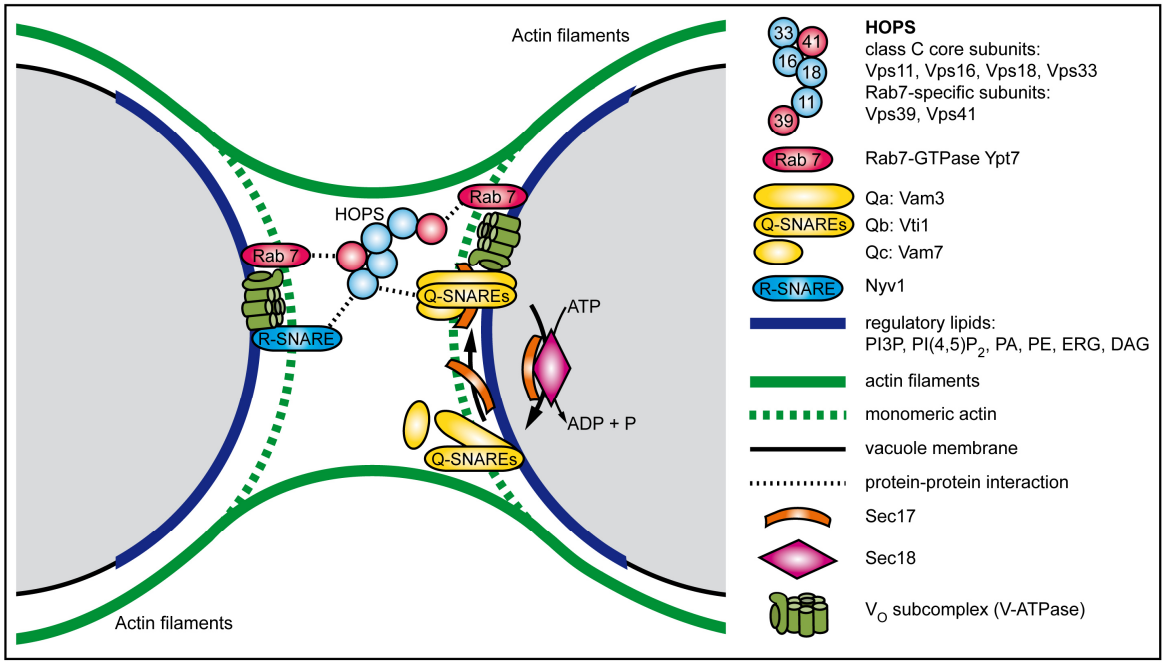

Figure 2: Schematic model of homotypic vacuole fusion in yeast. The drawing illustrates the state in which both membranes are tethered and depicts the most important factors that are necessary to undergo vacuole membrane fusion.

The first requirement for both vacuolar membranes are activated (GTP-bound) Rab7 GTPases (Ypt7p) that are recruited to a phosphatidylinositol-3-phosphate (PI3P)-positive membrane surface by their respective guanine exchange factor (GEF) complex Mon1-Ccz1. A so-called vertex ring forms, i.e. a microdomain enclosed only by Ypt7p excluding unnecessary proteins from the future membrane fusion site. Subsequently, the effector protein complex homotypic vacuole fusion and protein sorting (HOPS) is recruited. HOPS complexes consist of 6 members of the vacuole protein sorting (Vps) class, namely Vps11, Vps16, Vps18, Vps33, Vps39 and Vps41p. The specificity to bind Rab7-GTPases and PI3P is provided by Vps39p (which is also a GEF of Ypt7p) and Vps41p, whereas Vps33p coordinates the SNARE [soluble N-ethylmaleimide-sensitive factor (NSF) attachment receptor] proteins between donor and acceptor membrane. Vps33p is a Sec1/Munc18 (SM) protein that promotes *cis*- to *trans*- SNARE complex formation together with Vps1p (Dynamin), Sec17p (soluble NSF attachment protein, α-SNAP), Sec18p (NSF, AAA-ATPase) and ATP hydrolysis. This is crucial for the fusion as the *cis*-SNARE complex only leads to membrane docking, but not fusion. Actually, after a completed membrane fusion cycle Sec17p and Sec18p activity is also required to open

the *cis*-SNARE complexes on the vacuole/lysosome membrane prior to Ypt7p recruitment.

Besides its function in membrane fission, the dynamin-like protein Vps1p plays a crucial role in generating the necessary protein density required to form *trans*-SNARE complexes at the fusion site. One R-SNARE in the donor membrane and three Q-SNAREs (Qa, Qb and Qc) in the acceptor membrane have to be present. This 3:1 stoichiometry is mandatory, but which specific SNAREs are finally required depends on whether a heterotypic or homotypic fusion occurs. For the latter case, the R-SNARE Nyv1p is needed, whereas for heterotypic fusion events Ykt6p and Snc2p are employed. Vacuolar Q-SNAREs include Vam3p (Qa), Vti1p (Qb) and Vam7p (Qc). Vam7p is a soluble protein but binds to PI3P. Once a *trans*-SNARE complex is formed, it was proposed that homotyic vacuole fusion further requires membrane integral V_0 subcomplexes of the vacuolar H^+-ATPase (V-ATPase) in both opposing membranes to finalize the fusion. The two proteolipid V_0 rings themselves would create a *trans*-complex leading to a radial opening of a protein pore (Peters et al., 2001). Though the direct involvement of V-ATPase subcomplexes in membrane fusion was put into question (Coonrod et al., 2013), recent work demonstrated a pH gradient independent role of the V_0 subcomplex (Desfougères et al., 2016). The current model suggests conformational changes in the small c-subunit of the V_0 subcomplex when it is in contact with the *trans*-SNARE complex. This causes a membrane curvature change via the reorientation of lipid acyl chains and thus opens a membrane fusion pore (Strasser et al., 2011).

It is important to note that SNAREs alone do not provide the fusion specificity. The correct pairing of SNAREs in the *trans*-complex which is required for vacuole fusion is subject to the proof-reading activity of the HOPS complex. Furthermore, via phosphorylation of the Vps41 subunit by the tonoplast-localized casein kinase Yck3, the HOPS complex is able to recognize and specifically tether adaptor protein-3 (AP3) -dependent clathrin-coated vesicles (CCVs) originating from the Golgi. This trafficking route exclusively delivers the SNARE proteins Vam3 and Nyv1 to the vacuolar membrane. Without bypassing the post-Golgi route, CCVs could thus also fuse with late endosomes by mistake. This highlights the important concept that separated transport routes are crucial to deliver all necessary components for a fully functional membrane fusion machinery. Most importantly, it illustrates the interdependency that leads to fusion deficiencies if only one transport route is blocked. Another group of key regulatory factors for vacuole membrane fusion are lipids. As mentioned before, PI3P provides a binding surface for the Rab7-GTPase, the HOPS complex and for the vacuolar Qc-SNARE. In addition, phosphatidylinositol 4, 5- bisphosphate [$PI(4,5)P_2$], diacylglycerol

(DAG), ergosterol (ERG), phosphatidic acid (PA), and phosphatidylethanolamine (PE) were shown to be critical for efficient membrane fusion. They are enriched in the boundary membrane of the vertex ring and serve the purpose of stabilizing the fusion site as well as promote the recruitment of the aforementioned fusion factors.

Lastly, actin dynamics play an important role especially during homotypic vacuole membrane fusion, too. Before the initial tethering of the opposed membranes by Ypt7 and HOPS, actin filaments that run along the vacuole are depolymerized to monomeric actin (globular actin), enabling vertex ring emergence. However, during *trans*-SNARE complex formation the actin monomers polymerize again into filaments supporting the final step of membrane fusion. The underlying mechanism is not yet identified. It could be either trapping and thus accumulation SNARE proteins to the fusion site ("actin fence") or generating membrane tension.

In conclusion, many different factors have to play in concert to allow efficient fusion with the vacuole/lysosome and hence represent the cardinal point for protein and lipid delivery to permit vacuole biogenesis at all.

Arabidopsis mutants of vacuole biogenesis

HOPS complex

In metazoan and yeast, the hetero-hexameric HOPS complex is one of the key players in the process of vacuole/lysosome fusion and biogenesis. *Arabidopsis thaliana* (Arabidopsis) homologs for all subunits were identified (Klinger et al., 2013; Vukašinović and Žárský, 2016), but the number of functional studies in vacuole biogenesis is limited. To date, all reported homozygous loss-of-function mutants of HOPS subunits in Arabidopsis are lethal (Rojo et al., 2001; Niihama et al., 2009; Hao et al., 2016), indicating a vital role in membrane trafficking. *vacuoleless1* (*vcl1*) is a T-DNA knockout mutant of the Arabidopsis homolog of yeast Vps16p, a core subunit of the HOPS complex, and was described as essential for vacuole biogenesis in Arabidopsis (Rojo et al., 2001). VCL1 localizes to MVBs and the tonoplast and was shown to interact with VPS11, VPS33 and the SYP2-type syntaxins SYP21 and SYP22 (Rojo et al., 2003). Cells of *vcl1* fail to form a central vacuole. Instead, they accumulate structures that are morphologically similar to autophagosomes, next to strong defects in cell division orientation and elongation. Eventually, *vcl1* embryos die at the late torpedo stage (Rojo et al., 2001). VCL1 is further important for the function of male and female gametophytes, even though there were no affected pollen tubes observed *in vitro* (Hicks et al., 2004). Similarly, a recent study demonstrated that pollen tubes cannot penetrate

into the transmitting tract of the stigma in a *vps41* knockout mutant thus leading to male sterility (Hao et al., 2016). Interestingly, even though the authors reported fragmented vacuoles, the *in vitro* pollen tube growth assays of wildtype and *vps41* were similar. Possibly because the pollen tube elongation in liquid medium or on plate (Hicks et al., 2004) might not depend on an intact and turgescent vacuole. VPS41 was further found to interact with RabG3c (Rab7 GTPase) and VAMP711 (tonoplast R-SNARE; Hao et al., 2016). The most likely scenario for VCL1 and VPS41 knockout mutants is that due to the fusion deficiency caused by incomplete HOPS complexes cells fail to form a central vacuole along with retained and missorted proteins. However, this does not exclude the synthesis of membrane material destined for the tonoplast, leading to the accumulation e.g. of late endosomes and autophagosomes. Therefore, vacuole biogenesis in plants has to be considered as a two component process of trafficking and membrane contribution.

For the human Vps41 it was shown that through its clathrin heavy chain repeat (CHCR) domain together with AP3, it can act as a self-assembling coat factor necessary for the regulated secretion of large dense core vesicles (LDCVs, Asensio et al., 2013). The same domain was shown to be responsible for VPS41 tonoplast localization and pollen tube function in Arabidopsis (Hao et al., 2016). Previously, a point mutation in this domain was reported to suppress the zigzag-inflorescence phenotype of the VTI11 mutant *zig-1*, by admitting atypical pairings of tonoplast SYP2 Qa-SNAREs with VTI12, a usually TGN-localized Qb-SNARE (Niihama et al., 2009). This is probably due to a decreased proof-reading stringency of the mutated VPS41.

In *Medicago truncatula*, HOPS subunit expression is modulated to change vacuole morphology. To establish symbiosis with N_2-fixing bacteria in root nodules, the rhizobia enter the cells and form specialized compartments, symbiosomes. On one side, the fully differentiated cells have to accommodate the newly forming organelle and on the other side it is crucial that symbiosomes do not fuse with the lytic lumen of the vacuole. Interestingly, in the host cells which establish symbiosis the expression of VPS39 and VPS11 is temporarily suppressed (Gavrin et al., 2014). This leads to a drastic decrease in vacuolar volume and tonoplast surface area, thus providing space for the emerging symbiosome. Moreover, these symbiotic compartments acquire a unique two-faced membrane identity marked by the presence of a Rab7-GTPase and the plasma membrane specific SNARE SYP132 (Catalano et al., 2007; Limpens et al., 2009). This is accompanied by the retargeting of the tonoplast aquaporin TIP1g to the symbiosome which in turn enables its inflation and reestablishment of cellular turgescence (Gavrin et al., 2014). Only during symbiosome senescence, the membrane is equipped with the

vacuolar SNAREs SYP22 and VTI11, gets acidified and digested (Limpens et al., 2009; Gavrin et al., 2014). This example demonstrates how membrane identity is established by several interdependent factors, at least Rab-GTPases, SNAREs and membrane tethering complexes.

Rab-GTPases

Small Rab-GTPases can cycle between their active and inactive state in a guanine nucleotide dependent manner (reviewed in Grosshans et al., 2006). GTP-bound Rab-GTPases can recruit a variety of effectors, e.g. HOPS complexes, that act together to perform crucial steps in processes of membrane tethering, transport and fusion. Thus, Rab7-GTPases play a pivotal role in the biogenesis and trafficking to vacuoles and lysosomes (reviewed in Guerra and Bucci, 2016). In Arabidopsis, a total of 8 Rab7 members have been identified (Rutherford and Moore, 2002; Vernoud, 2003; Woollard and Moore, 2008) and their important functions in protein trafficking towards lytic and protein storage vacuoles as well as their biogenesis were analyzed (Cui et al., 2014; Ebine et al., 2014; Singh et al., 2014). Surprisingly, *rabg3a-f* sextuple mutants are viable and can rescue the growth phenotype of the tonoplast Qb-SNARE VTI11 (*zig1*; Ebine et al., 2014). A possible explanation might be that there is a functional overlap with the remaining Rab7-GTPases RabG1, RabG2 and the residual RabG3f activity. Though the auxiliaries might have a decreased specificity for the effectors, what under competitive conditions would lead to their displacement, their accuracy is sufficient to take over in this mutant background.

The activation of Rab-GTPases is necessary for their membrane recruitment and is executed by guanine nucleotide exchange factors (GEFs). The Mon1-Ccz1 complex is the main GEF for Rab7-GTPases in early-to-late endosomal maturation and trafficking in yeast (reviewed in Balderhaar and Ungermann, 2013). It was recently demonstrated that only GTP-bound RabG3f localizes to the tonoplast, whereas its inactive GDP-bound form is only recruited to MVBs. The expression of constitutively inactive (GDP-locked) RabG3f^{T22N} caused the formation of enlarged MVBs, fragmented vacuoles and led to the secretion of soluble PSV cargo (Cui et al., 2014). Activated canonical Rab5 [RHA1 (RABF2a) and ARA7 (RABF2b)] recruited SAND1-CCZ1 as a GEF effector complex that interacts with GDP-bound RabG3f (Cui et al., 2014; Singh et al., 2014). Moreover, although the function of the SAND1-CCZ1 complex in exchanging Rab5 with Rab7-GTPases is conserved in Arabidopsis, it was shown that unlike in yeast and mammals, it is required to render MVBs competent for vacuole fusion (Cui et al., 2014; Ebine et al., 2014; Singh et al., 2014). Similar to *vps41* (Hao et al., 2016), *mon1* mutants have strong

defects in pollen development caused by impaired cysteine protease transport to vacuoles and impaired pollen tube formation (Cui et al., 2016b).

The subtle analysis of several RabG3 multiple knockout lines, mutants impaired in activating Rab5 (*vps9a*, Goh et al., 2007), Rab7 (*sand* and *ccz1* mutants) as well as AP3 mutants in combination with the trafficking of different tonoplast SNAREs and soluble cargo proteins unraveled another trafficking way to the tonoplast (Ebine et al., 2014). Besides transport routes dependent on either consecutive VPS9a activation of Rab5-GTPases, SAND1-CCZ1 mediated Rab5-by-Rab7 exchange and Rab7 activation, or only on VPS9a activation of Rab5-GTPases without the requirement of Rab7 activity, there is at least one additional transport way to the vacuole important for vacuole biogenesis, the AP3-dependent route (Feraru et al., 2010; Wolfenstetter et al., 2012).

SNAREs

SNARE proteins drive membrane fusion by forming a hetero-tetrameric *trans*-SNARE complex out of Qa-, Qb-, Qc and R- SNAREs which are discretely located on the two opposing membranes involved. Efficient membrane fusion requires a 3Q:1R-SNARE ratio (Fasshauer et al., 1998; Figure 2). Depending on their subcellular localization, the composition of the SNARE complexes is specific for different compartment and vesicle combinations. *In vitro*, membrane fusion in a 4Q and 2Q:2R combination can be executed either with excessive amounts of SNAREs or with chemicals increasing membrane fluidity in order to lower the required force exerted by SNAREs (Fratti et al., 2007; Starai et al., 2008; Karunakaran and Fratti, 2013).

In Arabidopsis, about 60 members were identified, including the specific complexes that promote fusion with the tonoplast (Uemura et al., 2004; Lipka et al., 2007; Fujiwara et al., 2014). Different functions of individual vacuolar SNAREs of all groups (Q and R) in cargo trafficking to LVs and PSVs with their corresponding impact on growth and development have been studied widely. While single knockout mutants were usually viable, higher order mutants that eliminated a whole SNARE group were embryo lethal. This is true for the Qa-SNAREs SYP21 - SYP23 (Sanderfoot, 2001; Uemura et al., 2010; Shirakawa et al., 2010), the Qb-SNAREs VTI11 and VTI12 (Surpin et al., 2003); the activity of VTI13 is restricted to root hairs; Larson et al., 2014) and the SNARE complex containing VAMP727 (R-SNARE) and SYP22 (Ebine et al., 2008). Similar mutant analysis for the R-SNAREs VAMP711-714 and Qc-SNAREs SYP51 and SYP52 are not available yet. However, transient over-expression of SYP51 and SYP52 revealed that an imbalanced amount of these SNAREs strongly affect vacuole trafficking (De Benedictis et al., 2013). In conclusion, vacuole fusion requires at least one representative of Qa, Qb, Qc and R-

SNARE and members of each specific SNARE-group share a certain functional overlap beside their specific transport functions (Surpin et al., 2003; Sanmartín et al., 2007; Niihama et al., 2005).

Vacuolar SNAREs are separately transported to the tonoplast (reviewed in Uemura and Ueda, 2014). The Qa-SNARE SYP22 was shown to be transported in a VPS9a and Rab5-GTPase dependent manner but independent of AP3 or activated Rab7-GTPases (Ebine et al., 2014). Conversely, trafficking of the R-SNARE VAMP713 to the vacuole was only impaired in the AP3 mutants *ap3-μ* and *ap3-δ*/*zip4* (Ebine et al., 2014). This transport diversification allows to fine-tune specific cargo delivery during temporary developmental programs and also prevents premature membrane fusion along the vacuolar trafficking route. At the same time this interdependency is susceptible to general trafficking errors. For example, RNAi-mediated knockdown of VPS45, a protein which coordinates the SYP41/SYP61/VTI12 SNARE complex at the TGN (Sanderfoot et al., 2001; Zouhar et al., 2009), induces morphological defects of vacuoles. It was hypothesized that similar to the retromer complex mutants *vps35 b-1c-1* and *vps29-1/mag1-1* (Shimada et al., 2006; Yamazaki et al., 2008) impaired recycling of vacuolar sorting receptors (VSRs) upon VPS45 silencing leads to the accumulation of numerous small PSVs and LVs resulting in impaired cell elongation and severe dwarfism (Zouhar et al., 2009).

Regulatory lipids

Structural membrane lipids are composed of varieties of phosphatidylcholine (PC), phosphatidylethanolamine (PE), phosphatidylserine (PS), phosphatidylinositol (PI) and phosphatidic acid (PA) (van Meer et al., 2008). These groups differ in their biophysical properties, particularly the space occupied by their hydrophilic head and lipophilic tail, which promote the formation of positive (e.g. PI) or negative (e.g. PA, PE) membrane curvature (Thiam et al., 2013). The curvature is further enhanced by the steric pressure exerted by proteins present in the membrane (Stachowiak et al., 2013). Lipids can promote fusion and fission events, as shown for yeast vacuoles (Wickner, 2010).

In Arabidopsis, so far PI3P, PI(3,5)P_2 and their generating enzymes were shown to play a role in vacuole development. The class-III PI-3-kinase (PI3K) VPS34 produces PI3P which can be detected with a genetically encoded biosensor at MVBs and the tonoplast (Voigt et al., 2005; Vermeer et al., 2006). VPS34 knockdown or its chemical inhibition leads to strong developmental defects (Welters et al., 1994; Lee et al., 2008b). Homozygous PI3K knockout mutants are gametophytic lethal and show an abnormal vacuole phenotype in developing pollen (Lee et al., 2008a). Membrane recruitment of

yeast Vps34p requires Vps15p, which is an effector protein of Rab5 and Rab7 (Murray et al., 2002; Yan and Backer, 2007). Interestingly, the impaired pollen germination and development in Arabidopsis VPS15 mutants can be rescued *in vitro* by external PI3P application (Xu et al., 2011). WM and LY294002 (LY) inhibit PI3K activity and lead to homotypic fusion of MVBs eventually preventing their fusion with the tonoplast (Wang et al., 2009; Takáč et al., 2012, 2013). Accordingly, upon WM and LY treatment the fluorescent PI3P sensor 2xFYVE exerts an increased cytoplasmic signal with only very few but enlarged labeled MVBs (Vermeer et al., 2006; Takáč et al., 2013; Zheng et al., 2014b). The local generation of a PI3P-postive membrane surface on the emerging MVB and the tonoplast is likely to be one of the initial steps to recruit further membrane fusion factors. With new MVBs constantly originating from the TGN (Scheuring et al., 2011) and matured MVBs steadily fusing with the vacuole, their number might be at an equilibrium. Erasing PI3P from the membrane by chemical inhibition of PI3K probably resets the membrane identity by releasing all factors bound to PI3P, thereby shifting the balance towards homotypic MVB fusion (Wang et al., 2009). However, recent studies demonstrated that isolated vacuoles in *itt3*, a mutant allele of VTI11, refuse upon treatment with WM and LY (Zheng et al., 2014a, 2014b).

FAB1/PIKfyve kinases process PI3P to PI(3,5)P_2 at the tonoplast. Its activity and the corresponding PI(3,5)P_2 were shown to be important especially for vacuole reorganization during pollen development (Whitley et al., 2009) and stomata opening (Bak et al., 2013). Yet, recent attempts to link PI(3,5)P_2 depletion to vacuole morphology by chemical FAB1/PIKfyve inhibition were inconclusive (Hirano et al., 2016). The reverse reaction to produce PI3P from PI(3,5)P_2 is mediated by the tonoplast localized SUPRESSOR OF ACTIN (SAC) phosphatases 2-5 (Nováková et al., 2014). Their over-expression led to inflated vacuoles whereas the triple and quadruple knockout mutants contained multiple small vacuoles, probably a consequence of altered PI levels (Nováková et al., 2014). Though it remains elusive by which mechanism PIs are used to modulate the shape of vacuoles, PI3P seems to play an important role in vacuole fusion events.

Other factors that affect vacuole biogenesis

With MVBs a variety of endocytosed plasma membrane receptors responsible for hormone, nutrient and pathogen sensing are send to the vacuole for degradation. For this, intra-luminal vesicles are formed by the action of three hetero-multimeric protein complexes of the Endosomal Sorting Complex Required for Transport (ESCRT) machinery, ESCRT-I to ESCRT-III (Winter and Hauser, 2006; reviewed in Cui et al., 2016a). For all ESCRT complexes and their interacting proteins mutants have been

isolated that fail to internalize ubiquitinated cargo at different stages. This leads either to cargo missorting to the tonoplast or MVB maturation arrest and impaired fusion with the vacuole. ESCRT mutants often exhibit fragmented vacuoles and are mostly embryo or early seedling lethal, phenotypes they share with fusion factor mutants mentioned before. Prominent examples are *amsh3* (Isono et al., 2010; Katsiarimpa et al., 2011, 2013, 2014), *fyve1*/*free1* (Barberon et al., 2014; Gao et al., 2014; Kolb et al., 2015) and *alix* (Kalinowska et al., 2015; Cardona-López et al., 2015). These mutants are unable to form central vacuoles, but accumulate autophagosomes and numerous small and highly constricted vacuoles instead (Kolb et al., 2015; Kalinowska et al., 2015). This supports the idea that a single impaired vacuolar transport route can have deleterious effects on vacuole development if e.g. SNARE abundance at the tonoplast is disturbed. However, the phenotypes have to be considered as the result of additive effects of protein missorting and fusion incompetence. Though the vacuole morphology in these mutants has been reported to be strongly affected, there was still a considerable amount of tonoplast produced. Intriguingly, cells of the root elongation zone and hypocotyl in *amsh3-1* and *alix4* continued to be extended properly, demonstrating that a fully inflated vacuole is not necessarily needed for cell elongation as long as the missing volume is occupied, or complemented by cytoplasm.

Interestingly, the development of male and female gametophytes seems to rely on the formation of a central vacuole. During the first mitotic division of wild type pollen grains a big vegetative cell and a small generative cell are generated by an asymmetric division where the polar localization of the microspore nucleus is supported by the central vacuole (Twell, 2011). Similarly, during the consecutive mitotic divisions of the functional megaspore and its development into the syncytium, the nuclei located at the opposite poles are separated by a central vacuole (Christensen et al., 1998; Drews and Koltunow, 2011). However, in mutants of *VACUOLELESS GAMETOPHYTES* (*VLG*) no central vacuoles form at these stages, leading to or at least coinciding with an early arrest of gametophyte development (D'Ippólito et al., 2017).

Vacuole development in Arabidopsis

Surprisingly little is known about the morphological development of vacuoles in Arabidopsis. In fully differentiated cells they exist as a single organelle (Hunter et al., 2007), i.e. the central vacuole, that usually takes up almost the entire cell volume and are generally believed to develop from smaller vacuoles by homotypic fusion (Taiz, 1992; Marty, 1999; Seguí-Simarro and Staehelin, 2006). The root tip of Arabidopsis is an excellent experimental system to study the process of vacuole biogenesis because it

exhibits a permanent developmental gradient originating from the quiescent center. As the cells divide in the meristem and increase in length over time also LVs develop from numerous small individual compartments into big central vacuoles. The accompanied water influx is mediated by specifically expressed aquaporins localized at the plasma membrane and the tonoplast (Gattolin et al., 2009, 2011). However, there are no detailed studies that follow their spatio-temporal development. Existing works investigating vacuole biogenesis in plants relied on 2-dimensional (2D) images from which effectual models were reasoned. Of course they are not necessarily wrong but might oversimplify the reality. 2D cross-sections of lytic vacuoles from electron microscopy (EM) and images acquired with confocal laser scanning microscopy (CLSM) often show circular areas. Hence, it is reasonable to assume that central vacuoles develop by homotypic fusion of many small individual vacuoles. At the same time one can argue that these spheres might be part of a widespread tubular system, as 3-dimensional (3D) reconstructions of EM tomograms of cytokinetic cells in Arabidopsis root tips already implied (Seguí-Simarro and Staehelin, 2006).

What would be the advantage of tubular vacuoles over one or more sphere-like or cuboid-shaped compartments? Cell divisions in root tips only occur in the meristematic and early elongation/transition zone. It was proposed that a constricted tubular conformation of LVs in these cells helps to accommodate the forming cell plate and phragmoplast-associated microtubule arrays during cytokinesis (Seguí-Simarro and Staehelin, 2006). During the early embryo development in *gravitropism defective 2* (*grv2*) mutants, after the first zygote division vacuoles in apical cells do not break down. As a direct consequence symmetric cell wall positioning is disturbed, leading to the formation of an abnormally large cell that persists until the embryo reaches the heart-stage (Silady et al., 2008). This demonstrates that bulky vacuoles in dividing cells can hinder the precise cell plate positioning that is necessary for symmetric cell divisions, especially in tissues like roots that rely on anisotropic growth.

How could a tubular morphology be established? It was recently demonstrated that exogenous application of synthetic auxin, 1-naphtylacetic acid (NAA), increases the abundance of vacuolar SNAREs, most importantly VTI11, and leads to strongly constricted vacuoles in elongating epidermal root cells (Löfke et al., 2015). Moreover, NAA treatment negatively affected the overall capability of atrichoblast cells to elongate and inhibition of auxin biosynthesis caused luminal expansion of vacuoles. The NAA induced modulation of vacuolar shape and cell elongation was rescued in auxin receptor mutants, pi4kß1/2 double mutants and by extended wortmannin (WM) treatment (Löfke et al., 2015). This work showed that the morphology of vacuoles in elongating cells can

be fine-tuned by the abundance of tonoplast SNAREs in an auxin-dependent manner and has an impact on cell expansion, especially when considering the differential cell growth and vacuole morphology in trichoblast and atrichoblast cells (Berger et al., 1998; Löfke et al., 2013). The NAA-induced constriction of vacuoles was further linked to the reorganization of the actin cytoskeleton (Scheuring et al., 2016). Genetic and pharmacological disruption of actin filaments, but not microtubules, showed a direct impact on vacuolar shape. Instead of forming tubules, round and sphere-like vacuoles were induced (Scheuring et al., 2016). Löfke et al. (2015) and Scheuring et al. (2016) demonstrated that the vacuole shape determination relies on an interplay of tonoplast integral proteins (SNAREs) and the outside actin/myosin cytoskeleton. It is not known how actin filaments establish the direct contact to the tonoplast (Wang and Hussey, 2015), but a prime candidate is NET4A, a member of the NETWORKED (NET) protein super family (Deeks et al., 2012). NET proteins share the plant-unique N-terminal NET actin-binding (NAB) domain, but their C-terminal coiled-coil regions are very diverse and provide membrane specificity.

What is the origin of the tonoplast?

In principal, the volume and surface area multiply several times during vacuole development. Therefore, vast amounts of newly synthesized tonoplast have to be delivered to the existing vacuole solely for the purpose of growing surface area and volume. This raises the question from which donor compartment the tonoplast originates. There exist basically two different models: one claiming the Endoplasmic Reticulum (ER), the other suggesting post-Golgi trafficking to be the donor membrane.

The idea of the ER providing membrane material for the tonoplast was proposed by Matile and Moor, who analyzed root tips of *Zea mays* by freeze-etching electron microscopy (Matile and Moor, 1968). They noticed a striking similarity of the membrane texture of both, ER and tonoplast, and further pointed out that there is no such membrane surface homology to the Golgi Apparatus (Golgi). These findings were in agreement with previous data accounting hydrolytic activity to vacuoles and small ER derived vesicles (Matile, 1966; Matile and Moor, 1968). A related model suggested cage-like enclosures of organelle-free cytoplasm by smooth ER that would then inflate, thereby forming the central lytic vacuole (Amelunxen and Heinze, 1984; Hilling and Amelunxen, 1985). In 1969, Mesquita described vacuole biogenesis in *Lupinus albus* root tips, also proposing the ER to be the origin of the vacuole membrane (Mesquita, 1969). He confirmed the development of small, usually spherical vacuoles into larger volumes by membrane fusion. In addition, he presented electron micrographs that show

stretches of rough ER transitioning into, or connecting, sphere-like enlargements reminiscent of lytic vacuoles. Mesquita further discussed that these concise prolongations of the rough ER which inflate over time to form vacuoles, are specialized precursors that he called provacuoles. Also, he hypothesized that central vacuoles form by fusion of smaller vacuoles thereby *displacing* the cytoplasm instead of engulfing and digesting it (Mesquita, 1969).

The most common model of vacuole biogenesis proposed that the origin of provacuoles are vesicles derived from so called "Golgi-associated Endoplasmic Reticulum from which Lysosomes form" (GERL; Marty, 1978). Analyzing root tips of *Euphorbia characias*, Marty (1978) described the GERL as "... a twisted, smooth-surfaced, polygonal meshwork of anastomosing tubules and saccules, ..." in which he detected acid phosphatase activity. In combination with the spatial organization of the observed structures, Marty assumed that GERL-derived provacuoles fuse with each other to enlarge and form ring-like autophagic vacuoles. These would enclose cytoplasmic content which then becomes digested and thus lytic vacuoles would form. Eventually, GERL was identified to be the *trans*-Golgi Network (TGN; Griffiths and Simons, 1986) and so the origin of tonoplast membrane was accordingly believed to arise from post-Golgi trafficking towards the vacuole (reviewed in Taiz, 1992; Marty, 1999).

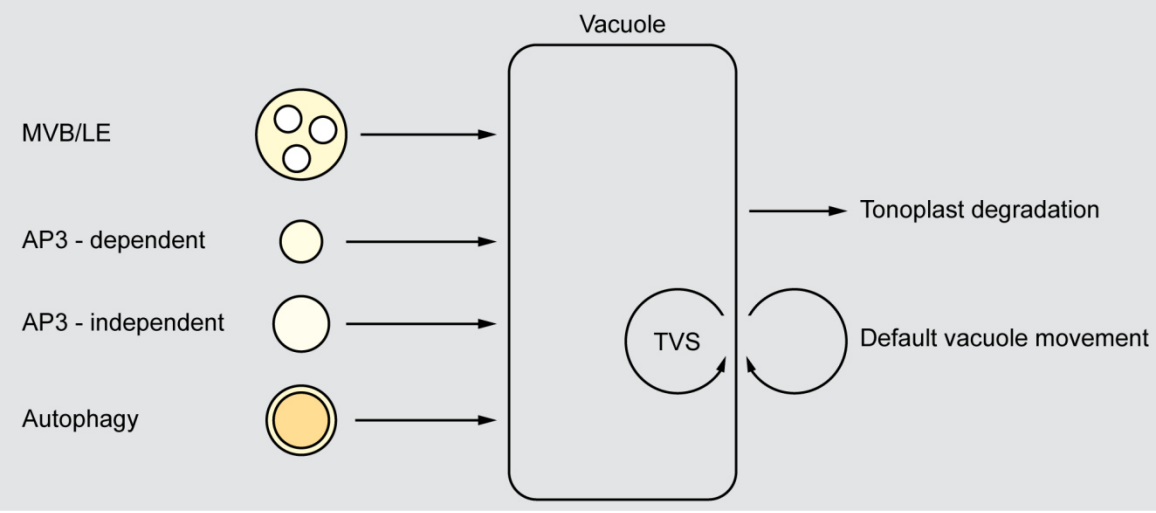

Figure 3: Membrane equilibrium at the tonoplast. The left side of the scheme features known vacuolar trafficking pathways that deliver membrane surface to the tonoplast and thus contribute to its expansion. Remodeling processes that lead to a reduction of tonoplast surface are put on the right side. MVB/LE = Multi-vesicular body/late endosome, AP3 = adaptor protein complex 3, TVS = trans-vacuolar strand(s).

It is important to note that due to the lack of quantitative measurements none of the aforementioned models can be supported or disproved. In the end, all vesicular trafficking routes that end in the LV contribute to its surface increase (Figure 3). These are late endosomes, vesicles of the AP3-dependent as well as AP3-independent

pathway and autophagosomes (reviewed in Uemura and Ueda, 2014; Viotti, 2014; Paez Valencia et al., 2016). Other processes, e.g. membrane and tonoplast protein turnover, that most likely reduce the tonoplast surface area are largely unknown in Arabidopsis.

The question is, whether the well-dosed network of vesicle-based vacuolar trafficking routes has the necessary capacity to provide enough new tonoplast surface during cell expansion.

Aims of the thesis

The first aim of this study was to describe the morphological development of lytic vacuoles in Arabidopsis in detail. For this, we made use of different CLSM techniques that allowed us to precisely render single vacuolar compartments in developing cells of seedling root tips. From these results we calculated both, surface area and volume of vacuoles during their development.

As a second objective we aimed to analyze whether default post-Golgi trafficking towards the vacuole can provide enough membrane surface to expanding vacuoles in the elongation zone of Arabidopsis roots or if a another, yet unknown transport route might be the main membrane source. Hence, we also studied the trafficking of the V-ATPase and vacuolar H^+-pyrophophatase (V-PPase), two of the most abundant proteins at the tonoplast (Carter et al., 2004).

The third goal was to investigate the role of membrane tethering complexes in the context of vacuoles biogenesis. To avoid the previously described embryo lethality of HOPS subunit knockout mutants (Rojo et al., 2001; Niihama et al., 2009; Hao et al., 2016), we employed an inducible knockdown system against the core subunit VPS16.

Results

Lytic vacuoles develop as single compartments

Our first aim was to precisely describe the 3D morphological development of lytic vacuoles in meristematic cells of the *Arabidopsis thaliana* root tip. This experimental system is particularly suitable as it allows to follow vacuole development gradually from the stem cells of the quiscent center (QC) up to differentiated cells. 5-days-old *Arabidopsis* wild-type seedlings were stained with 2',7'-bis(2-carboxyethyl)-5(6)-carboxyfluorescein acetoxymethyl ester (BCECF-AM), a fluorescent dye that specifically accumulates in the lumen of lytic vacuoles (Swanson and Jones, 1996; Krebs et al., 2010). The outline of individual cells was distinguished by applying the endocytic tracer FM4-64 which predominantly stains the plasma membrane and the TGN/EE 5 to 15 minutes after application (Dettmer et al., 2006). Using CLSM we detected stained vacuoles within most cell types including QC cells (Figure 4 A, white arrowhead). In contrast, lytic vacuoles in cells of the vasculature could not be stained by BCECF within the time of incubation. In all recorded single 2D optical sections we detected numerous separately stained vacuoles per cell. They displayed variable sizes and shapes, ranging from round to long tubular stretches (Figure 4 A).

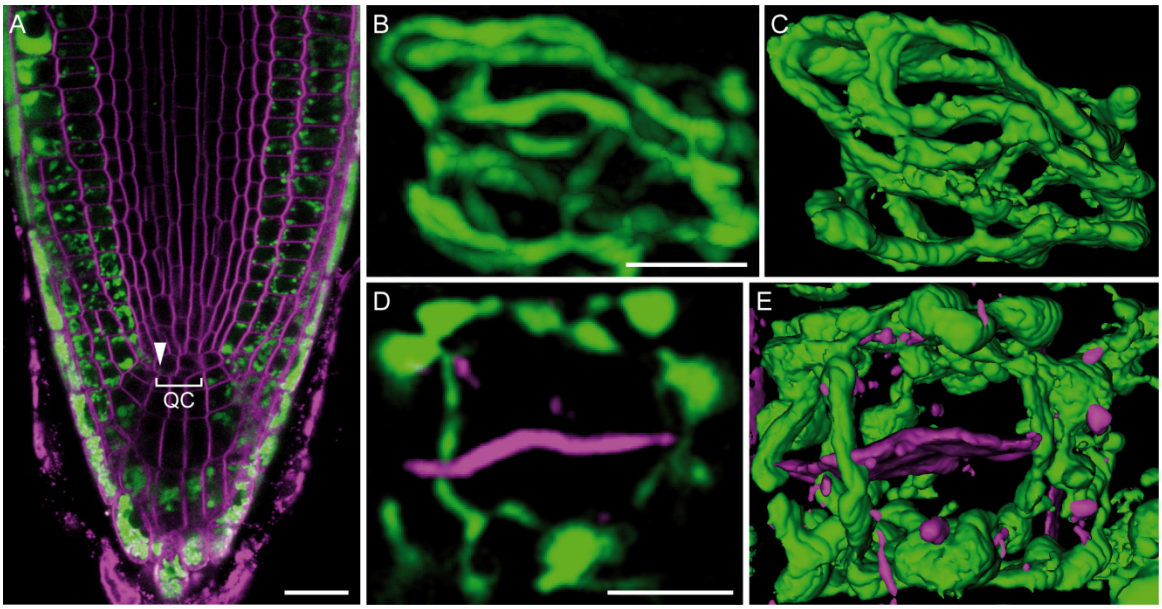

Figure 4: Vacuole morphology in meristematic cells of *Arabidopsis thaliana* root tips. CLSM images of 5-days-old *Arabidopsis thaliana* seedlings stained with BCECF-AM (green) and FM4-64 (magenta). (A): 2D overview image of a meristematic root tip zone. (B) and (D): Projections of Z-stacks of different volumes acquired from individual cells. (C) and (E): Surface renderings of corresponding Z-stacks shown in (B) and (D). Note that the vacuole forms a single tubular compartment that meanders through the cell also during cell plate formation (E). QC = quiescent center. Scale bars indicate 20 µm in (A) and 5 µm in (B) and (D). The presented images were published in Viotti et al., 2013 but colors and labels were modified.

We made similar observations by analyzing ultra-thin sections of high-pressure frozen and freeze-substituted samples using EM (Supplemental Figure 1 A to C). The same appearance of vacuoles was also found in dividing cells (Supplemental Figure 1 C).

In order to reconstruct vacuoles that are present within a single cell, we recorded series of images along the Z-axis (Z-stacks). This allowed us on one hand to specifically select optical planes of interest from more extensive datasets and on the other hand to project their 3D information into a 2D image. When the Z-stacks were projected, the BCECF signal of stained vacuoles within individual meristematic cells consistently seemed to form a single complex tubular network (Figure 4 B). However, a maximum projection usually integrates the spatial information only from a fixed angle. By using texture-based surface rendering ("3D Viewer", Schmid et al., 2010) we were able to display vacuolar networks independent of their original orientation, thereby visualizing the linked vacuole network more reliably (Figure 4 C). Interestingly, vacuoles in cytokinetic cells displayed the same morphological features. A maximum projection around the center of a forming cell plate revealed an interconnected tubular vacuole between the future daughter cells (Figure 4 D). In the corresponding surface rendering we found the tubular vacuole network to form a cage-like structure around the cell plate (Figure 4 E). Taken together, we showed that in meristematic cells of the root tip lytic vacuoles do not exist as individual compartments but rather form linked tubular networks. Based on these observations we were wondering if this complex morphology persists during cell elongation and differentiation.

Therefore, we systematically acquired Z-stacks of cells in the meristematic, elongation and early differentiation zone of BCECF-stained *Arabidopsis* root tips. Due to the developmental gradient along the root axis it was not necessary to follow distinct cells but analyze cells of specific zones instead. Figure 5 shows representative surface renderings. As observed before, meristematic cells displayed a linked tubular vacuole network (Figure 5 A). The same was true for vacuoles of cells in the elongation zone (Figure 5 B). Here, corresponding to the more developed state of the cells the vacuolar system appeared to be more inflated. Cells of the early differentiation zone already contained the well-described central vacuoles (Figure 5 C). They have a rectangular cuboid-like shape that makes up most of the cell volume. The improved post-processing further allowed us to calculate the volume of the surface-rendered lytic vacuoles. In combination with "BoneJ" (Doube et al., 2010) we compared both volume as well as surface area of cells and vacuoles, respectively. Comparing the surface areas and volumes of vacuoles in the three different root zones (Figure 5 D), we found that their ratio decreased from about 3.5 to 0.5. This corresponded to the progressively inflating

vacuoles along the developmental axis. Based on the average dimensions of cells and their vacuoles of each root zone, we calculated a drop in the proportion of cell to vacuole volume from around 7.0 down to 1.1 (V_{cell} and $V_{vacuole}$, Supplemental Figure 1 D). This reflected the typical observation that the cell volume of differentiated root cells is occupied up to 90 % by the lytic vacuole.

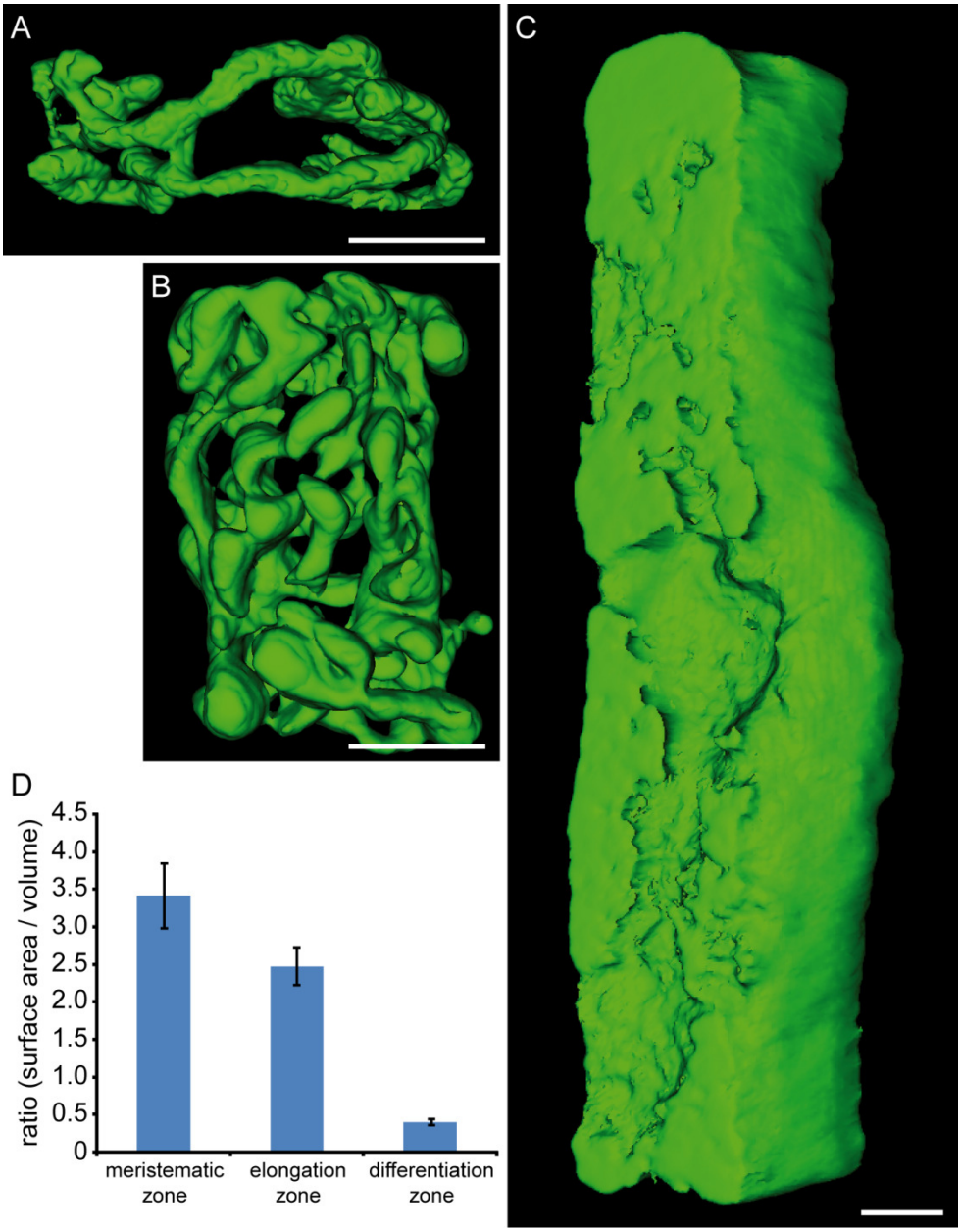

Figure 5: Vacuole morphology during root development. 5-days-old seedlings of *Arabidopsis thaliana* were stained with BCECF-AM and subsequently imaged with CLSM. Z-stacks of individual cells in different root tip zones were acquired. The contained vacuolar networks were extracted and surface-rendered using the "3D Viewer" plug-in in ImageJ. The images show representative examples of lytic vacuoles from cells of the meristematic (A), elongation (B) and differentiation zone (C). The ratio of the surface area and the occupied volume of all extracted vacuoles was calculated for the indicated zones (D) using "BoneJ". Error bars represent standard deviation of n ≥ 3 cells per root zone. Scale bars indicate 5 µm. The presented images were published in Viotti et al., 2013, but (C) was scaled down to 60 %.

At the same time the ratio of the cell surface area and its vacuoles remained virtually constant with an average of 1.04 (A_{cell} and $A_{vacuole}$, Supplemental Figure 1 E). This indicated that the portion of cytoplasmic content does not change regardless of the total cell volume.

Lytic vacuoles are highly dynamic compartments

With texture-based surface rendering we were able to precisely visualize the complex 3D vacuolar shape at a given time point. To describe vacuole movements over time, we recorded Z-stack series of the root elongation zone in seedlings expressing the tonoplast marker protein VHP1-GFP (Segami et al., 2014; Figure 6). The projected movies revealed that under normal conditions vacuoles continuously revolve in a very complex 3-dimensional manner (Figure 6 A).

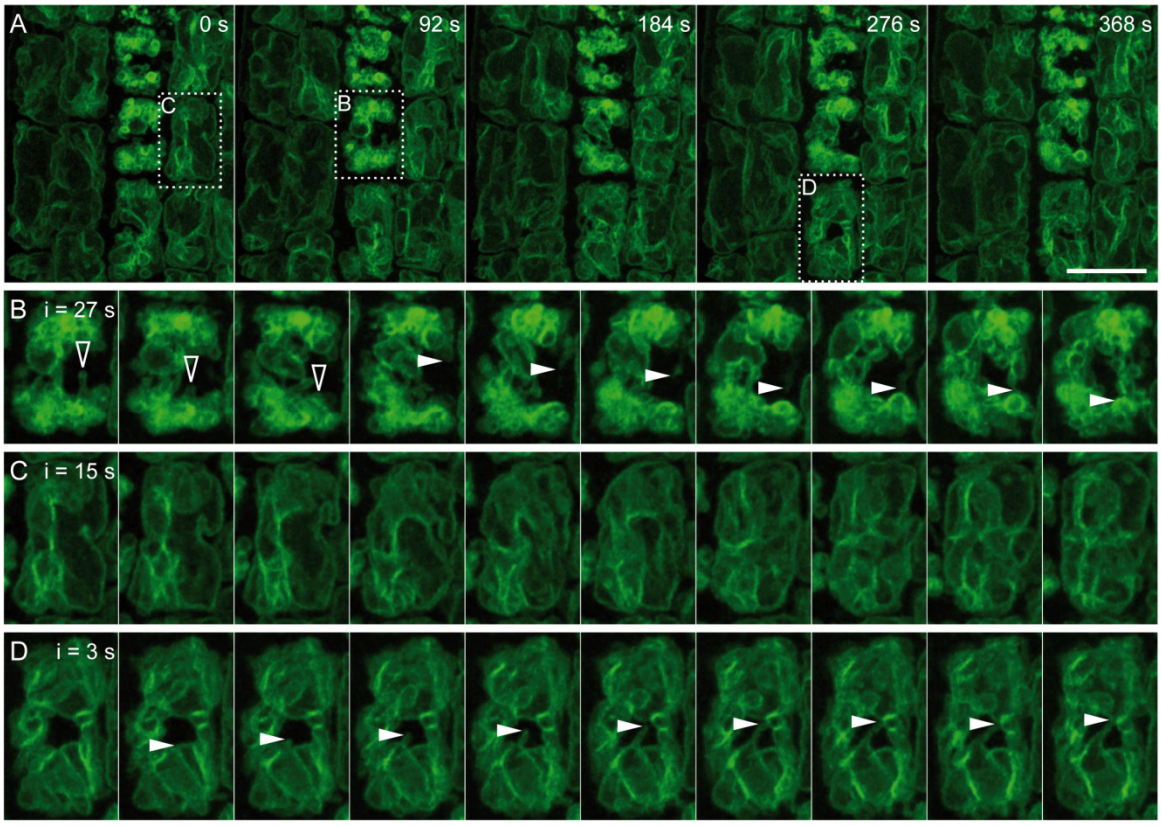

Figure 6: Lytic vacuoles constantly change their morphology. Individual frames of a time lapse recording in the elongation zone of 5-days-old *Arabidopsis thaliana* seedlings expressing VHP1-GFP (A). The depicted images are maximum projected Z-stacks of the indicated time points. White dotted boxes in (A) indicate the start frame of the respective time series shown in (B) to (D). The interval (i) between the individual frames is given in the first picture. Open and closed arrowheads point to individual events of significant morphology changes of the respective vacuoles. Scale bar indicates 20µm.

We observed that tubules constantly protruded and retracted from the main vacuole volume (open arrowheads, Figure 6 B) and established new connections over time by homotypic fusion (closed arrowheads, Figure 6 B). Moreover, other vacuoles were moving like rolling barrels (Figure 6 C). Interestingly, during this global movement tubular

crosslinks were still established within seconds (arrowheads, Figure 6 D). Taken together, 4D imaging of the tonoplast revealed a surprisingly active motion of vacuoles.

vaccFRAP: Quantification of vacuole connectivity by Fluorescence Recovery After Photobleaching

Our surface renderings demonstrated that lytic vacuoles can form a continuous compartment. In contrast, their dynamic default movement made us wonder whether this is only a transient state or if isolated vacuoles constantly fuse to form a single compartment. Therefore, we developed a method to quantify the connectivity status of vacuoles. In this context connectivity describes if and to what extend a vacuole volume inside a cell is linked.

We first analyzed BCECF-stained vacuoles in cells of the early elongation zone. Looking at single optical sections, the vacuoles of DMSO treated control cells displayed the previously described convoluted morphology (Figure 7 A). Contrary to this, application of 250 nM IAA led to a constriction of the vacuole system whereas 10 µM IAA induced fully expanded vacuoles, a feature that usually is only found in differentiated cells. In LatA treated cells vacuole lumina appeared to be more inflated, round and allegedly fragmented. Surface renderings of these treatments further illustrated the morphologically altered vacuole systems (Figure 7 B). However, the rendering quality was not sufficient to determine whether the vacuoles were still forming a continuous or an isolated volume. This applied to the constricted vacuoles of the 250 nM IAA treatment as well as to the putatively fragmented ones of the LatA treatment. The rendering quality depends directly on the optical resolution of the microscope. The smaller the observed tubular network or the closer two separated volumes come together, the more restrictive the axial resolution of CLSM becomes, thereby limiting the rendering accuracy. Although we improved the spatial resolution by decreasing either the voxel size (lateral resolution) or the pinhole diameter (axial resolution), we could not achieve the necessary gain in rendering quality. We therefore developed another way to determine whether vacuole compartments within single cells are directly linked or isolated. This method applied the Fluorescence Recovery After Photobleaching (FRAP) approach to a stained volume. Here, fluorescence recovery depends on the diffusion of bleached and unbleached BCECF molecules within the vacuolar volume instead of lateral diffusion within a membrane. This method was termed vacuole-connectivity FRAP (vaccFRAP).

Even though fluorescence intensities of only a single focal plane were acquired, the obtained information allowed us to draw conclusions about the connectivity state of the bleached vacuole volume. The speed of fluorescence recovery depends on the number

and cross-section width of tubules through which the bleached and unbleached vacuolar volumes are connected. Based on their recovery half-time ($T_{1/2}$), the results were sorted into 4 different groups (Figure 7 C).

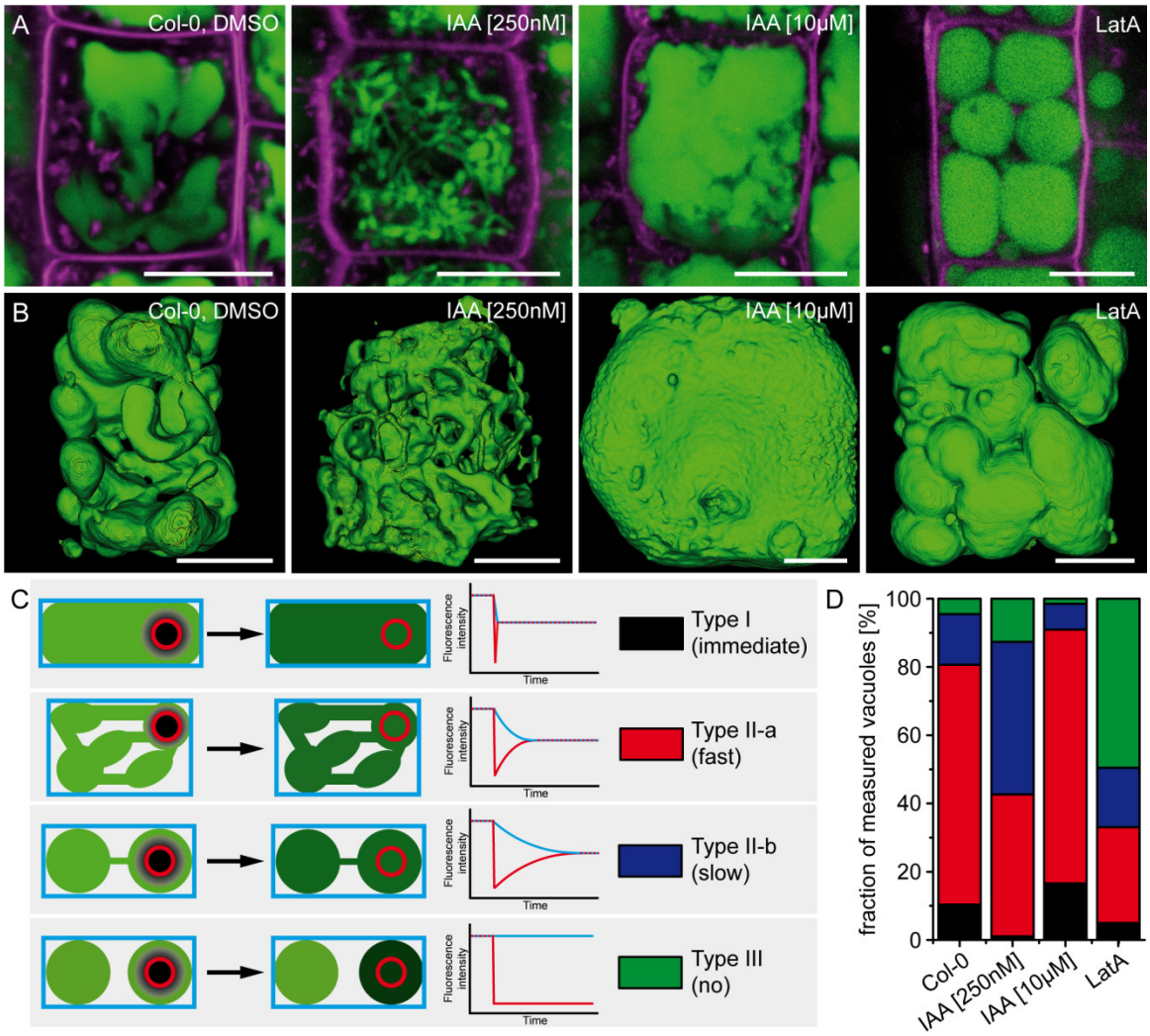

Figure 7: Quantification of vacuole connectivity by Fluorescence Recovery After Photobleaching (FRAP). (A) Representative single optical sections from root tips of 5-days-old *Arabidopsis thaliana* seedlings treated with the indicated compounds. The seedlings were stained with BCECF (green) and FM4-64 (magenta). (B) Surface renderings of representative Z-stacks were computed. (C) The model (left) shows the basic principle of a quantitative 2D FRAP-based method to measure vacuole connectivity. The scheme features the possible connection types of vacuoles (depicted in green). The colored outlines indicate the areas of fluorescence intensity measurement (total vacuole area = blue rectangle, bleached area = red circle). The middle panel showcases theoretical fluorescence intensity recordings that are used to classify the results. (D) The graph summarizes the distribution of all measured vacuoles of the indicated treatments with n = 222 (Col-0), n = 197 (250 nM IAA), n = 199 (10 µM IAA), and n = 121 (LatA). Scale bars indicate 5 µm.

Type I vacuoles are fully differentiated, entirely inflated compartments. Due to the standardized imaging they recover instantaneously after bleaching (Supplemental Figure 2 A). Vacuoles of Type II-a have a morphology typically found in cells of the root elongation zone. They are highly connected among each other and FRAP occurs rapidly. However, compared to Type I, the recovery time is delayed due to diffusion hindrance as

their volumina are connected via tubules. The more constricted these tubular connections are the more limited the diffusion becomes. By using the "FRAP Profiler" (Lynch et al., 2012) we calculated and plotted $T_{1/2}$ of all FRAP experiments (Supplemental Figure 2 B). Based on the average $T_{1/2}$ of Type II-a wild type vacuoles we set the cut-off time for Type II-b to 2 seconds. If there is no fluorescence recovery at all the volumes are truly isolated and thus designated as Type III. In addition, we occasionally recorded fusion events of bleached and unbleached vacuoles. However, these were not further considered but are mentioned here as an additional experimental outcome (Type IV, Supplemental Figure 2 C). By standardization of recovery types we next compared the vacuole connectivity of the previously examined conditions (Figure 7 A and B).

Our results show that 95 % of all measured vacuoles in untreated cells of the root elongation zone have entirely connected volumes (Figure 7 D). This includes all recovery types from Type I to Type II-b. With about 87 % (250 nM IAA) and more than 98 % (10 µM IAA) both auxin treatments were comparable. Nevertheless, the induced changes in vacuole morphology were reflected in altered fractions of Type II-a and Type II-b compared to the control. The more constricted vacuoles of the low auxin concentration resulted in an increased portion of slow fluorescence recoveries (ca. 45 % in 250 nM IAA vs. 15 % in Col-0). On the other hand, the fully expanded vacuoles of the high auxin concentration led to a higher amount of fast and immediate recoveries (almost 91 % in 10 µM IAA vs. 80 % in Col-0). Apart from these findings, about half of the connectivity measurements in LatA treated cells were isolated vacuoles of Type III. Compared to the control, there also was a decrease in the number of Type II-a vacuoles whereas the fraction of Type II-b did not change. In addition to these results we calculated the average $T_{1/2}$ of Type II recoveries for all treatments (Supplemental Figure 2 B). We first determined the fastest possible recovery time in central vacuoles of fully differentiated cells (v_{max}). Here, the bleached molecules can freely diffuse into all directions and mix with unbleached ones. We received a $T_{1/2}$ for v_{max} of 0.194 s, whereas vacuoles in the elongation zone of untreated wild type cells recovered on average within 1.16 s. Again in line with the altered vacuole morphology, the average $T_{1/2}$ for 10 µM IAA was only about 0.862 s, but 2.808 s for 250 nM IAA. This showed a direct correlation between the constricted morphology and the fluorescence recovery time. The longest average $T_{1/2}$ was 3.47 s measured in LatA treated vacuoles. Taken together, we showed that vaccFRAP is a reliable method to quantify the state of vacuole connectivity in single cells. We next focused on the question which is the main membrane source for vacuole biogenesis.

Membrane surface contribution of MVB/LEs to tonoplast expansion

The common model of vacuole biogenesis describes post-Golgi trafficking as the key source of new vacuolar membrane. Therefore, we analyzed the size, number and lifetime of MVB/LEs evaluating how much membrane surface these compartments can contribute to vacuole biogenesis.

First, the lateral dimensions of over 200 MVB/LEs from electron micrographs of wild type root tip cells were measured and averaged (Figure 8 A). We calculated a mean diameter of about 323.65 nm ± 94.6 nm which was comparable to previously published values (Haas et al., 2007; Jia et al., 2013). Assuming a perfect spherical shape of MVB/LEs, the standard surface area was about 0.33 µm². According to our previous surface renderings in cells of the transition zone that are about to elongate rapidly, we defined a model calculation in which the vacuole surface area doubles from 1225 µm² to 2450 µm². In total, a vacuole surface increase by 1225 µm² would thus require 3713 MVB/LE fusion events. Secondly, the average number of MVB/LE compartments per cell was determined from CLSM Z-stacks. For this, we used seedlings expressing the UBIQUITIN10 promoter driven PI3P sensor domain 2xFYVE fused to GFP (based on Vermeer et al., 2006). It was shown previously that this marker protein specifically labels late stages of MVB/LEs (Singh et al., 2014). Using "3D Objects Counter" (Bolte and Cordelieres, 2006) we calculated an average number of compartments per cell of about 165 ± 95 (Figure 8 B). Interestingly, this amount remained constant independent of the cell volume (Supplemental Figure 3 A).

In combination with the necessary number of fusion events, the overall MVB/LE population of a cell would need to be exchanged 22.5 times to generate 1225 µm² of new tonoplast surface area. In order to estimate whether this hypothetical MVB/LE flux was reasonable or not we determined the speed of vacuole growth and MVB/LE lifetime in root tip cells. From the previous renderings we know that surface areas of elongating cells equal that of the vacuole (Supplemental Figure 1 E). We further assumed that epidermal cells have a rectangular cuboid-like shape which has to elongate 2.5-fold to double its surface area given that width and height stay fixed. To measure this, we analyzed time-lapse recordings of growing root tips. On average, elongating cells needed 6748 seconds (about 112.5 minutes, Figure 8 C). We now divided the total elongation time of 6748 s by 22.5 - the number of MVB/LE population turnover to fit the model calculation - thus expecting a maximum lifetime of single MVB/LEs of about 300 s.

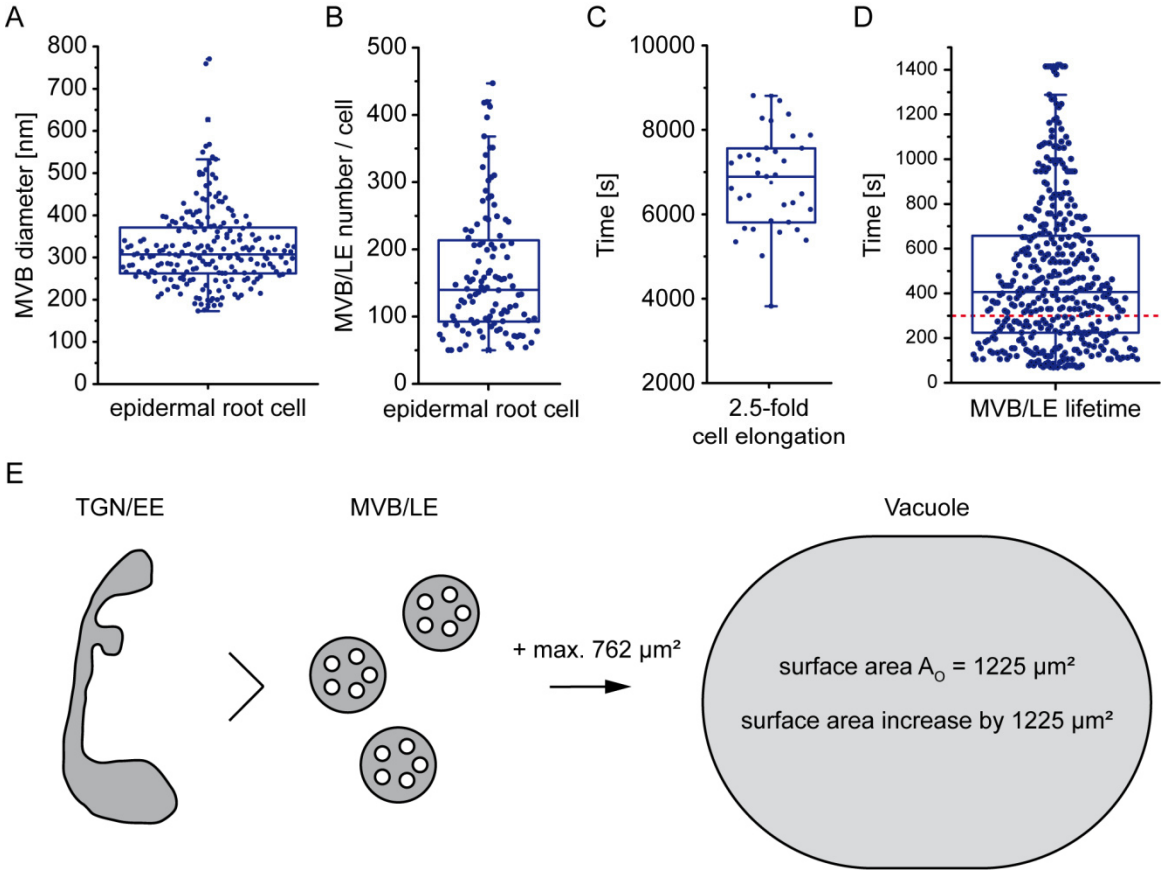

Figure 8: Evaluation of MVB/LE lifetime and their surface area contribution to tonoplast expansion. The mean diameter of MVB/LEs (323.65 nm ± 94.6 nm; from n = 210 MVB/LEs) from EM images acquired from 5-days-old *Arabidopsis thaliana* roots was calculated (A). The average MVB/LE number per cell (rounded to 165 ± 95; from n = 112 cells) was counted using the "3D Objects Counter" plug-in for ImageJ (Bolte and Cordelières, 2006) (B). It took n = 35 cells of the elongation zone about 6748 seconds to increase their length by 2.5-fold and accordingly for the vacuole to double its surface area (C). We tracked MVB/LE compartments in cells expressing 2xFYVE-GFP by recording Z-stack time series and quantified their lifetime with the "TrackMate" plug-in for ImageJ (Tinevez et al., 2016). We received a mean lifetime of approximately 481 seconds from n = 410 tracked compartments (D). To match the hypothesis that only MVB/LEs contribute to tonoplast expansion the maximum allowed lifetime was 300 seconds (red dotted line in D). (E) Model of vacuole membrane contribution by MVB/LEs. The measured values only allow for a maximal surface area increase of 762 µm².

To evaluate the actual average MVB/LE lifetime individual compartments in cells expressing 2xFYVE-GFP were tracked. Projected Z-stack time-lapse recordings were analyzed with "TrackMate" (Tinevez et al., 2016, Supplemental Figure 3 B). We calculated an average MVB/LE lifetime of 481 s (Figure 8 D). This value exceeded the previously calculated maximum allowed MVB/LEs lifetime of 300 s (red dotted line in Figure 8 D). In the context of our model calculation, the highest possible amount of membrane surface area that could be delivered to the tonoplast by fusing late endosomes was 762 µm² (Figure 8 E). We thus concluded that MVB/LE trafficking does not have the capacity to be the solitary source of tonoplast during cell elongation. This raised the question how the required membrane is provided as the vacuole develops, especially in rapidly elongating cells. We hypothesized that to a certain extend protein trafficking towards the vacuole should coincide with membrane flow. Interestingly, it is

not known how two of the most abundant proteins in the tonoplast, V-ATPases and V-PPases (Carter et al., 2004), are delivered there.

V-ATPase trafficking to the tonoplast bypasses Golgi and post-Golgi compartments

V-ATPase trafficking starts at the ER with the help of dedicated assembly factors (Herman et al., 1994; Graham et al., 2003; Neubert et al., 2008). The incorporation of VHA-a1 into the multi-subunit protein complex leads to TGN/EE localization, whereas VHA-a2 and VHA-a3 direct V-ATPases to the tonoplast (Dettmer et al., 2006; Krebs et al., 2010). We first checked if we can observe co-localization between the ER-resident V-ATPase assembly factor AtVMA21-GFP (Neubert et al., 2008) and VHA-a3-mRFP (Krebs et al., 2010). In meristematic root cells both marker proteins were always separated. While AtVMA21-GFP was present in the ER, VHA-a3-mRFP was exclusively localized at the tonoplast (Figure 9 A).

The following localization studies were performed in the *gnl1*;GNL1 BFA-sens. background (Richter et al., 2007). GNL1 is a Brefeldin A (BFA) insensitive guanine-nucleotide exchange factor on ADP-ribosylation factor (ARF-GEF) GTPase. It mediates retrograde transport of COPI-coated vesicles from the Golgi to the ER. Richter *et al.* complemented the *gnl1* mutant with a functional but BFA-sensitive GNL1 version (GNL1 BFA-sens.). Upon BFA treatment in the *gnl1*;GNL1 BFA-sens. background it is therefore possible to specifically inhibit the COPI-dependent transport. This also leads to the collapse of COPII-coated vesicle transport exiting the ER towards the Golgi and hence to the retention of cargo molecules at the ER. We first verified the correct localization of both V-ATPase populations in this background using VHA-a1-GFP and VHA-a3-mRFP. In untreated seedlings, both markers were detected in their previously described destinations (Dettmer et al., 2006; Krebs et al., 2010) and showed no fluorescence overlap (Figure 9 B). In a model where both V-ATPase varieties travel along the same transport pathway, VHA-a1 containing complexes are retained in the TGN/EE whereas V-ATPases with VHA-a3 subunits would proceed to the tonoplast. One major endosomal transport route for this is the MVB/LE pathway. It has been shown that these compartments mature directly from subdomains of the TGN/EE (Scheuring et al., 2011; Singh et al., 2014). Scheuring *et al.* (2011) also demonstrated that this process can be blocked at the level of the TGN/EE by Concanamycin A (ConcA) application eventually leading to vacuolar cargo retention. This applies to trafficking of the endocytic tracer FM4-64 (Dettmer et al., 2006), too.

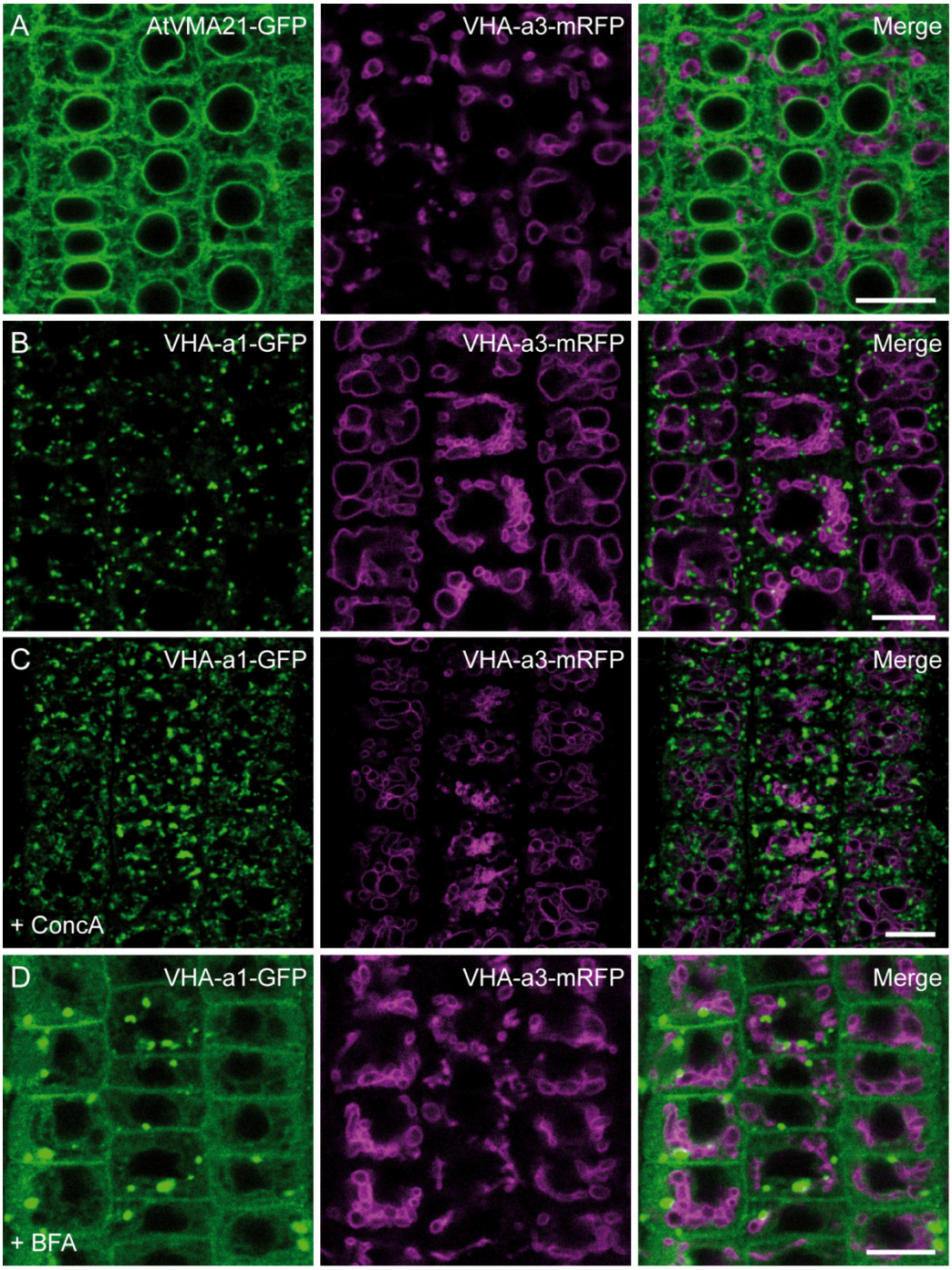

Figure 9: V-ATPase transport to the vacuole is Golgi-independent. 5-days-old seedlings of *Arabidopsis thaliana* expressing different marker proteins were investigated with CLSM. (A) Co-expression of the V-ATPase assembly factor AtVMA21-GFP (green) and the tonoplast localized V-ATPase marked by VHA-a3-mRFP (magenta). (B) Co-expression of VHA-a1-GFP (green) and VHA-a3-mRFP (magenta) shows no co-localization. (C) After 3 h treatment with 1 µM Concanamycin A (ConcA) VHA-a3-mRFP is still present at the tonoplast. (D) Upon 3 h treatment with 50 µM BFA in the *gnl1*;GNL1 BFA-sens. background, VHA-a1-GFP is retained in the ER and BFA compartments whereas VHA-a3-mRFP is still localized at the tonoplast. Scale bars indicate 10 µm. The presented images except (A) were published in Viotti et al., 2013, but colors were modified. (A) was replaced by VMA21-GFP crossed with VHA-a3-mRFP while the original figure showcased AtVMA12-RFP crossed with VHA-a3-GFP.

Therefore, we treated the VHA-a1-GFP VHA-a3-mRFP co-expression line in the *gnl1*;GNL1 BFA-sens. background with ConcA to check if VHA-a3-mRFP delivery to the tonoplast can be blocked (Figure 9 C). Compared to the control (Figure 9 B) the punctate

TGN/EE formed aggregates, indicating an effective transport block towards the vacuole. However, VHA-a3-mRFP still reached the tonoplast. For other proteins localized at the tonoplast it is known that they make use of different transport machineries. On the one hand, the sucrose transporter SUC4 is retained in the *cis*-Golgi in *pat2-1*, a mutant lacking the β-subunit of the adapter complex 3 (AP-3; Feraru et al., 2010; Wolfenstetter et al., 2012). On the other hand, the *myo*-inositol transporter INT1 still reaches the tonoplast in this mutant (Wolfenstetter et al., 2012). However, we could show that INT1-GFP can be retained in the TGN/EE by prolonged ConcA treatment while VHA-a3-GFP was still transported to the tonoplast in *pat2-1* mutant cells (experiments performed by Dr. Corrado Viotti, data not shown but published in Viotti et al., 2013).

We then checked whether - similar to VHA-a1 containing variants (Richter et al., 2007) - the ER export of VHA-a3 containing V-ATPases is dependent on COPII transport at all. We treated *gnl1*;GNL1 BFA-sens. seedlings expressing VHA-a1-GFP and VHA-a3-mRFP with BFA in order to block this route (Figure 9 D). While VHA-a1-GFP was retained in the ER and in aggregates, so called BFA compartments (Grebe et al., 2003; Hause et al., 2006), the VHA-a3-mRFP localization at the tonoplast remained unaffected. Since the turnover rate of V-ATPases is not known, it was possible that the observed fusion proteins at the tonoplast were pre-existent. Therefore, we performed experiments under similar conditions but photo-bleached both fluorescent proteins and recorded their recovery (Figure 10 A). We found that VHA-a1-GFP and VHA-a3-mRFP recover within 200 minutes (solid lines). Newly synthesized VHA-a1-GFP containing V-ATPases were detected in the ER (Figure 10 B), confirming the ER-export block of COPII-coated vesicles. In contrast, VHA-a3-mRFP bearing V-ATPases were still detected only at the tonoplast. As a negative control we incubated seedlings with the protein synthesis inhibitor cycloheximide (CHX) before adding BFA. Thereby fluorescence recovery of the tagged VHA-a subunits was prevented and it was shown that the previously recorded recovery was not due to diffusion from unbleached regions (Figure 10 A, dashed lines). Accordingly, in cells that were pre-treated with CHX we could not detect any specific signal localization (Figure 10 C).

By the means of ultra-structural immunocytochemistry (IEM) we aimed to trace both the V-ATPase and the V-PPase within the endomembrane system. On ultra-thin sections of high-pressure frozen and freeze-substituted *Arabidopsis* root tips we detected immunogold labeling of VHA-a3-GFP containing V-ATPases and endogenous V-PPase at the tonoplast (Supplemental Figure 4 A and B). In comparison, V-PPase detection was more distinct than that of VHA-a3-GFP (Supplemental Figure 4 C).

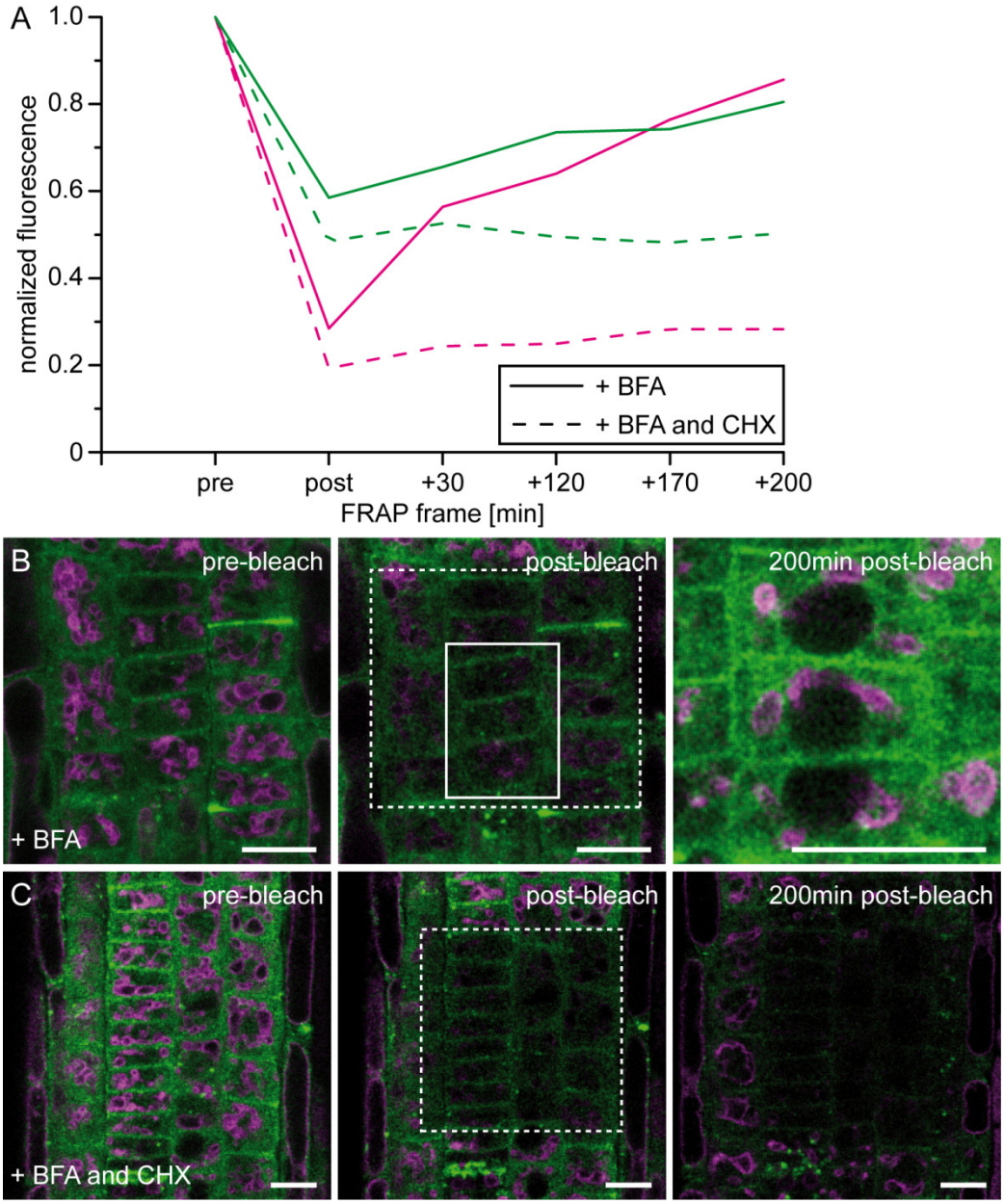

Figure 10: ER export of V-ATPases containing VHA-a1 but not VHA-a3 is dependent on COPI function. FRAP experiments with 5-days-old seedlings of *gnl1*;GNL1 BFA-sens. expressing VHA-a1-GFP (green) and VHA-a3-mRFP (magenta). The seedlings were pre-treated for 3 h with either 50 µM BFA or a combination of BFA and the protein synthesis inhibitor cycloheximide (CHX, 50 µM). (A): Recorded normalized FRAP over 200 minutes of both fluorescently tagged VHA-a subunits upon BFA (solid lines) and BFA + CHX treatment (dotted lines). (B) and (C): CLSM images before, immediately after, and 200 minutes after photobleaching. The white dashed boxes indicate the bleaching area, the solid box the magnified inset 200 minutes later. Upon induced ER-exit block newly synthesized VHA-a1-GFP is retained in the ER, whereas VHA-a3-mRFP fluorescence reappears at the tonoplast (B). (C) Upon CHX treatment there was neither fluorescence recovery nor re-localization of residual fusion proteins detectable. Scale bars indicate 10 µm. The presented data was published in Viotti et al., 2013, but colors were modified. The graph axes in (A) were compressed.

For both proteins there was hardly any signal detected in other endosomal compartments but the tonoplast (Supplemental Figure 4 D), even after prolonged ConcA treatment (Supplemental Figure 4 E). The quantification of gold particle density in the plasma membrane (PM), ER, Golgi, TGN/EE, MVB/LE and in the tonoplast with and

without ConcA (Supplemental Figure 4 F) affirmed the previous observations of exclusive VHA-a3-mRFP labeling at the tonoplast.

Up to this point our results suggested that there might be another, COPII-independent transport route to the vacuole, bypassing Golgi and post-Golgi compartments. This could either be a membrane junction between ER and tonoplast or an intermediate structure originating from the ER that delivers both, membrane material and proton pumps. If the latter is true, we hypothesized that it should be possible to visualize intermediate developmental stages between ER and vacuole with CLSM and IEM.

Provacuoles - An early developmental stage of vacuoles

Previously, we were not able to visualize vacuolar lumen in provascular cells of the root meristem with BCECF staining (Figure 4 A). However, as shown by surface rendering (Figure 5), VHA-a3-GFP fluorescence revealed a highly tubular morphology in these cells, too (Figure 11 A). Taking the remote luminal expansion of the observed vacuoles as a readout for development, vacuoles in provascular cells are certainly delayed compared to cortex or epidermal cells of the same age. Therefore, we were wondering if we could find any discrepancies between tonoplast and luminal labeling. Different from BCECF, SNARF-1 turned out to penetrate into deeper tissue layers of the root and was efficiently taken up into vacuoles of provascular cells (Figure 11 B). When comparing the combined signal of SNARF-1 and VHA-a3-GFP we could identify structures that were devoid of any luminal staining (white arrowhead, Figure 11 C).

Apparently, the same was true for BCECF-stained vacuoles in meristematic cortex cells expressing VHA-a3-mRFP (Figure 11 D and E). Here, we observed even more cases in which seemingly separated BCECF lumen was bridged by VHA-a3-mRFP labeled membrane stretches or loop-like ends (white arrowheads, Figure 11 F). We suspected that these structures might be linked to the development of vacuoles. Therefore, we quantified their amount in the meristematic and elongation zone (Figure 11 G). In the epidermis and cortex layer of the elongation zone, on average only 4 loop-like structures were counted. In contrast, we found ca. 75 loops in the meristematic region. Moreover, the VHA-a3-mRFP intensity across one membrane loop in comparison to that of a corresponding tonoplast section was usually at least twice as high (Figure 11 H), indicating the presence of two adjacent membranes below the optical resolution limit.

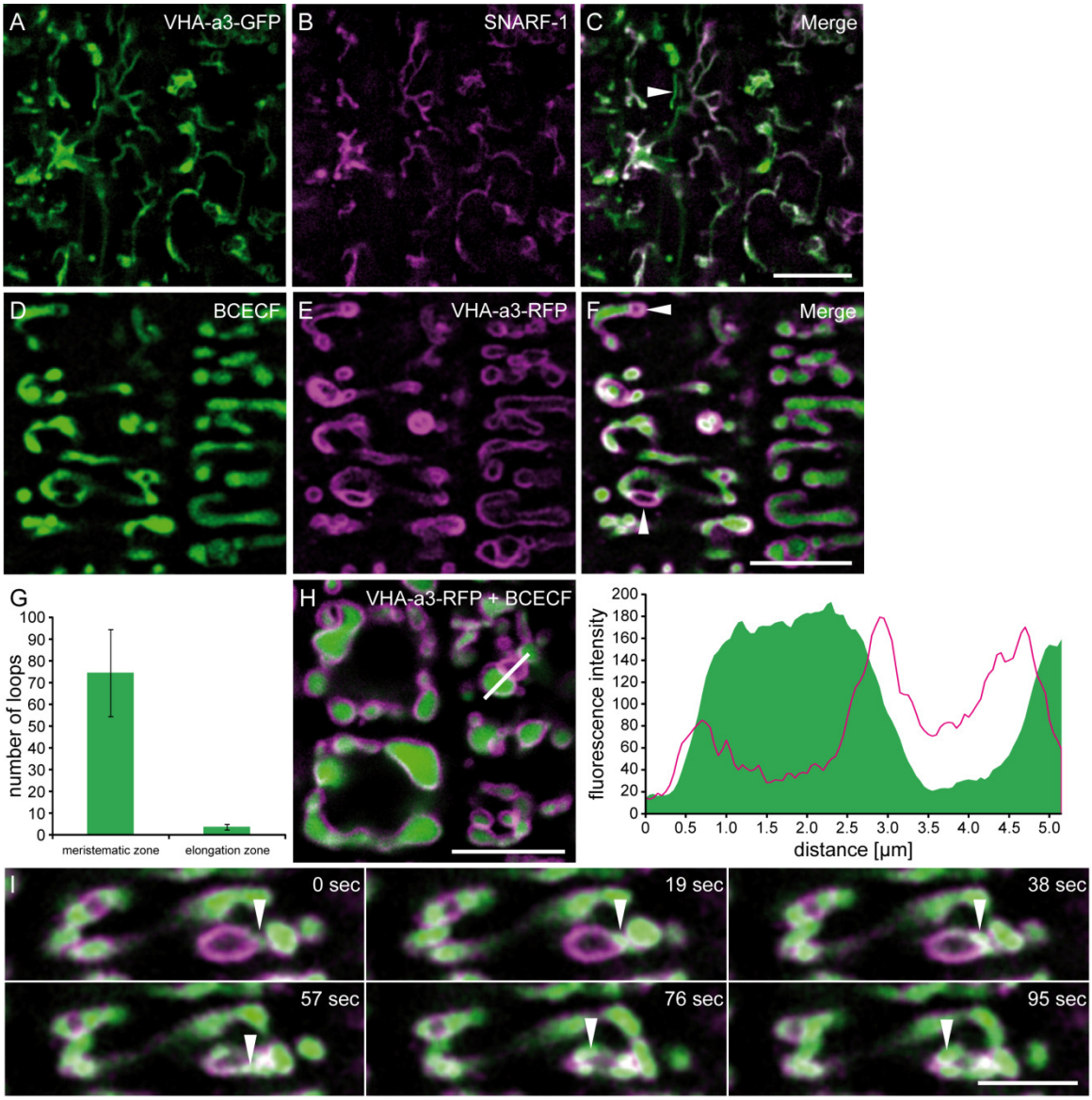

Figure 11: Vacuolar loops represent early stages of vacuole development. CLSM images of developing vacuoles in the root meristem of 5-days-old *Arabidopsis thaliana* seedlings. Provascular cells expressing VHA-a3-GFP (A, green) were additionally stained with SNARF-1 carboxylic acid (B, magenta). The merged image (C) shows a high overlap but also VHA-a3-GFP labeled membranes without SNARF-1 stained lumen (white arrowhead in C). Comparable membrane stretches were observed in BCECF stained meristematic cortex cells (D) expressing VHA-a3-mRFP (E). The overlap (F) shows tonoplast connections of spatially separated BCECF lumen (white arrowheads). These vacuolar loops were predominantly detected in epidermal and cortex cells of the meristematic region (G) and display a two-fold higher fluorescence membrane intensity than the adjacent single tonoplast layer (H, white line indicates the measured intensity profile). The green area depicts the BCECF intensity, whereas the magenta line represents VHA-a3-mRFP. Time-lapse recording of a vacuolar loop that converts into a tubular morphology (I). White arrowheads point to areas of BCECF filled lumen. Error bars in (G) represent the standard deviation of n = 10 roots. Scale bars indicate 10 µm in (A) to (H) and 5 µm in (I). The presented data was published in Viotti et al., 2013, but colors were modified.

In addition, we were able to record a time-lapse of a distinct VHA-a3-mRFP labeled membrane loop whose BCECF-stained lumen inflates over the course of 95 seconds (Figure 11 I). This implied that vacuolar loops indeed represent early stages in vacuole development and subsequently convert into tubular elements.

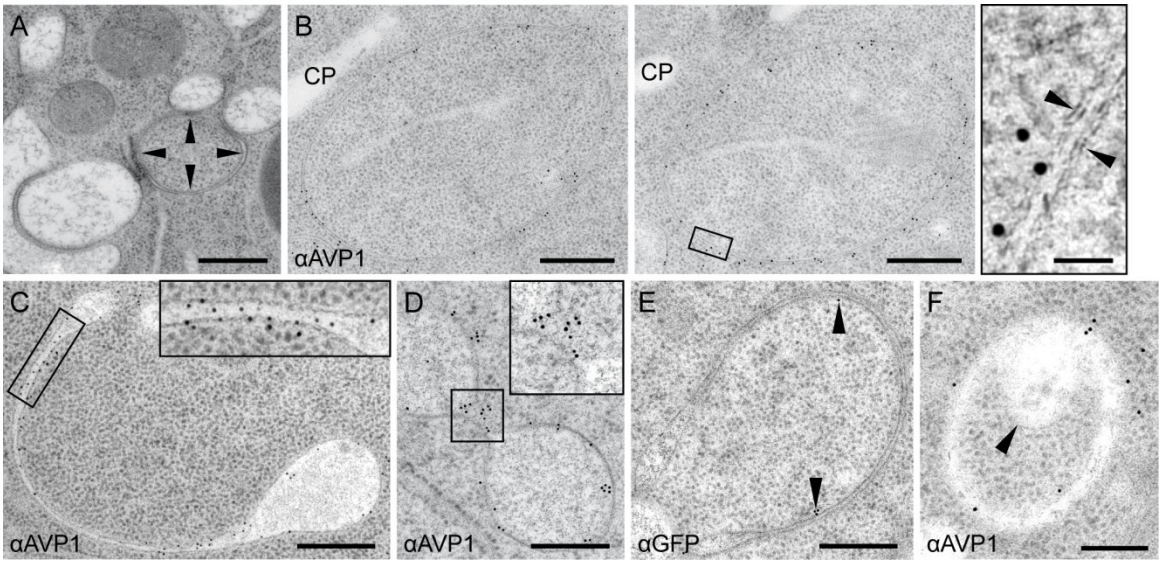

Figure 12: Vacuolar loops, or provacuoles, are early tonoplast membranes. EM images of 5-days-old *Arabidopsis* seedlings. The samples were high-pressure frozen and freeze substituted. Membrane loop with cytoplasmic content (A). IEM shows high V-PPase abundance in the aforementioned membrane loops on consecutive sections (B). A close-up (black box) reveals that the circular structures consist of two very close membranes (black arrowheads) with a highly constricted lumen. We termed these structures provacuoles. Semicircular provacuole with more inflated but unevenly concentrated lumen (C). Two early vacuolar volumes separated by a membrane constriction (D). In cells expressing VHA-a3-GFP antibodies against GFP also label provacuolar membranes (E, black arrowheads). Fusion event of MVB/LE (black arrowhead) with a provacuole (F). Scale bars indicate 400 nm in (A) to (E), 60 nm in the inset of (B) and 200 nm in (F). The presented data was acquired by Dr. Corrado Viotti and published in Viotti et al., 2013.

After that, we investigated vacuolar loops in meristematic cells using EM (performed by Dr. Corrado Viotti). Besides vacuoles with typical bright luminal texture, loop-like structures formed by two adjacent membranes were observed (black arrowheads, Figure 12 A). We found such circular membranes in consecutive sections being heavily labeled by immunogold against endogenous V-PPase (Figure 12 B), indicating that they could already be or become the tonoplast. As the magnified area shows (black box in B), the membrane loops are indeed two distinct lipid bilayers separated by a lumen of about 30 nm in diameter (black arrowheads in Figure 12 B). We also captured cases in which this lumen was more inflated and unevenly enlarged, comparable to a lytic vacuole (Figure 12 C). This observation was similar to the previously recorded vacuolar loop that converted into a tubule (Figure 11 I). Apart from closed or open circular morphologies, we also found repeatedly constricted but connected vacuole volumes (Figure 12 D). With gold-coupled GFP antibodies in seedlings expressing VHA-a3-GFP we then verified that V-ATPases are present in similar membrane loops, too (Figure 12 E). Interestingly, we captured a fusion event between a MVB/LE with an V-PPase labeled membrane loop (Figure 12 F), supporting our hypothesis that the observed structures are of tonoplast nature. Moreover, taking into account the high abundance of vacuolar loops in the meristematic zone and the observed gradual developmental stages of these structures,

we concluded that they indeed are early stages of vacuole biogenesis. We thus designated them provacuoles in reference to Matile and Moor (1968).

The origin of provacuoles

By definition, provacuoles represent early stages of vacuole biogenesis. To investigate this in more detail we analyzed mutants along the default vacuolar transport routes and their effects on provacuole formation.

We first examined the post-Golgi trafficking mutant *pat2-1* (Feraru et al., 2010) crossed to plants expressing VHA-a3-GFP. On average, we counted 284 vacuolar loops in the meristematic root zone of *pat2-1* seedlings which was almost 4 times higher than compared to wild type (Figure 13 A). Similar to the Col-0 control, the amount of loops in the elongation zone decreased. However, with ca. 104 it was more than 25-fold higher than in wild type seedlings. This points to a prolonged stability of these membrane structures. As we exemplarily showed before, the fluorescence intensity of vacuolar loops was approximately doubled in comparison to a single tonoplast layer (Figure 11 H). Interestingly, VHA-a3-GFP labeled vacuolar loops in the meristematic (Figure 13 B) and in the elongation zone (Figure 13 C) of *pat2-1* mutants were on average 2.5 times more intense (Figure 13 A), suggesting that they consist of more than two opposed membranes. To verify this, we performed IEM on *pat2-1* cells using the V-PPase antibody. In line with previously published results describing comparable membrane structures inside vacuoles (Feraru et al., 2010), we found provacuoles with an increased number of stacked membranes (Figure 13 D).

We next examined the RNA-interference line against *VPS45* (*siVPS45-10d*, Zouhar et al., 2009). In this mutant we also found multilayered provacuoles with a phenotype similar to that in *pat2-1* (Figure 13 E). The same holds true for the vacuole transport inhibition induced by ConcA treatment (Figure 13 F). Subsequently, we analyzed the BFA-treated *gnl1*;GNL1 BFA-sens. seedlings, but still detected normal provacuoles (Figure 13 G). In conclusion, Golgi and post-Golgi trafficking inhibition led to altered provacuole morphology but did not prevent their formation.

amsh3 mutants are unable to form central vacuoles (Isono et al., 2010) but instead accumulate a high number of autophagosomes eventually leading to seedling death. We analyzed *amsh3* mutant seedlings to see if they are still able to form provacuoles. We found both normal and morphologically altered provacuoles labeled by V-PPase antibodies (Figure 13 H). Moreover, we became aware that autophagosomes share a high similarity to provacuoles.

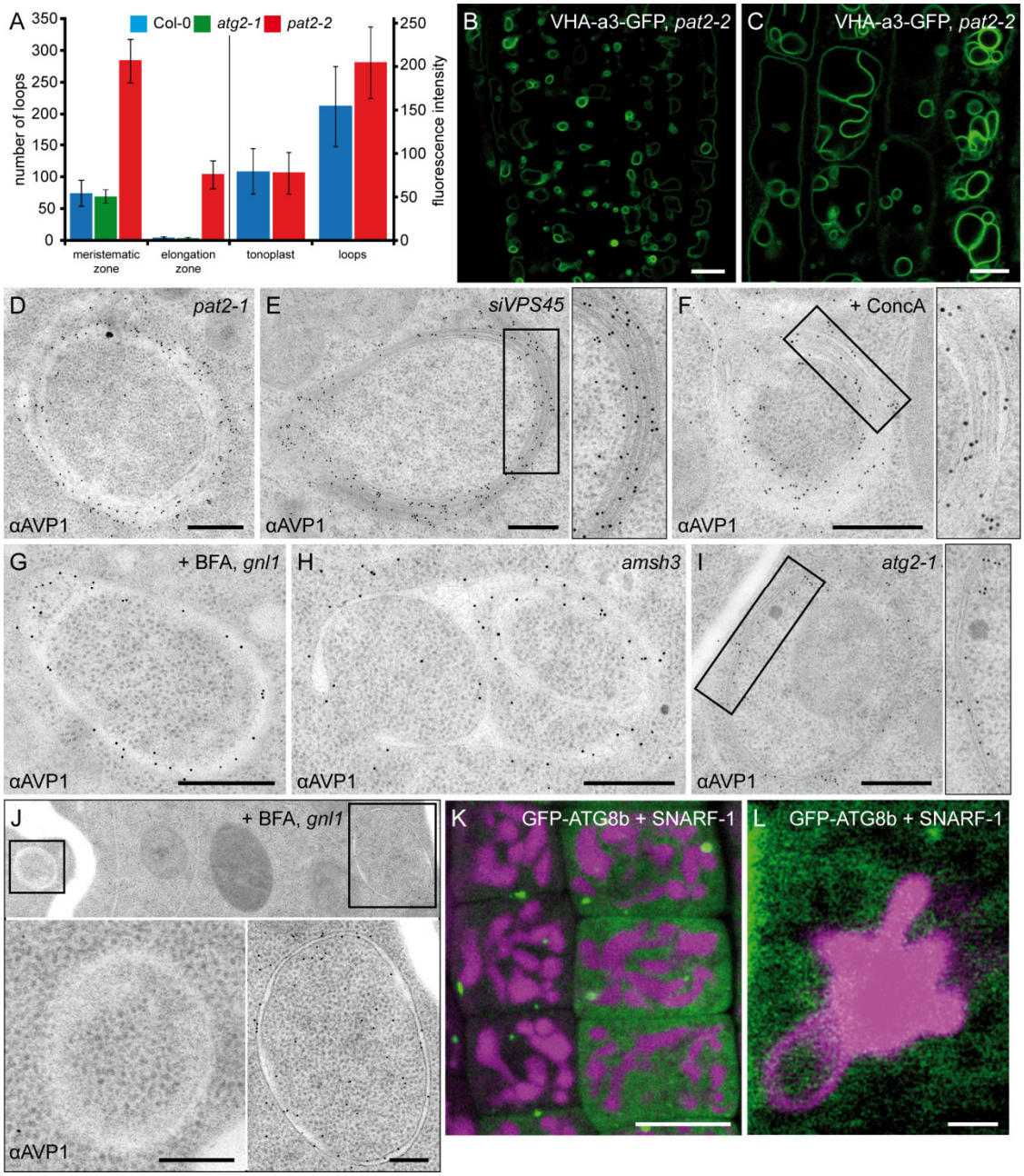

Figure 13: Provacuole formation is independent of Golgi or post-Golgi trafficking does not require the ATG machinery. Quantification of the number and intensity of provacuoles in root tips of 5-days-old seedlings of Col-0, *atg2-1* and *pat2-2* (A). CLSM images of VHA-a3-GFP in *pat2-2* mutants illustrate abundance and intensity of vacuolar membrane loops especially in cells of the meristematic (B) and elongation zone (C). (D) to (I): IEM sections of different trafficking mutants and inhibitors incubated with AVP1 antibodies and subsequently labeled with immunogold particles. The formation of provacuoles was morphologically altered but not prevented in *pat2-1* (D), *siVPS45* (E), ConcA-treated (E), BFA-treated *gnl1*;GNL1 BFA-sens. (F), *amsh3* (H) and *atg2-1* (I) seedlings. Ultra-thin section showing two similar double membrane structures (black boxes) of which only one is exclusively labeled by AVP1 antibodies identifying it as a provacuole (J). (K) and (L): CLSM images of meristematic cells expressing the autophagosome marker protein GFP-ATG8b (green). The seedlings were co-stained with SNARF-1 (magenta) to visualize the vacuole lumen and vacuolar loops. Error bars in (A) represent the SD for n = 10 roots for the number of loops and n = 65 loops for the fluorescence intensity for each genotype. Scale bars indicate 10 µm in (B), (C) and (K),1 µm in (L), 400 nm in (D) to (I) and 200 nm in (J). IEM data was acquired by Dr. Corrado Viotti. The presented results were published in Viotti et al., 2013, but colors were modified.

They usually also consist of two adjacent membranes that enclose portions of the cytosol and fuse with the vacuole. Although autophagosomes are not acidic until they fuse with

the vacuole (Klionsky et al., 2008), we were wondering whether the autophagy machinery generating phagophores at the ER could be responsible for provacuole formation. For this, three mutants of the core autophagy genes that are impaired in autophagosome formation (reviewed in Michaeli et al., 2014) were selected, namely *atg2-1* (Inoue et al., 2006), *atg5-1* and *atg7-2* (Thompson et al., 2005; Hofius et al., 2009). We found the number, formation and morphology of provacuoles unchanged in all investigated mutants (Figure 13 A and I; Supplemental Figure 5 A and B). Additionally, two similar double membrane structures on an ultra-thin section prepared from a BFA-treated *gnl1*;GNL1 BFA-sens. seedling were identified (Figure 13 J, black boxes). Only one of them was labeled by immunogold particles against V-PPase, identifying it as a provacuole, whereas the other was presumably an autophagosome. This suggests that the presence of proton pumps is an exclusive feature of provacuoles. Another core protein of autophagy in plants, *ATG8*, is already present during phagophore formation and can still be detected on autophagic bodies inside the vacuole (Le Bars et al., 2014; Merkulova et al., 2014). Therefore, we also analyzed the GFP-ATG8b marker line together with SNARF-1 stained lytic vacuoles in meristematic cells (Figure 13 K and L). Even though we observed GFP-ATG8b labeled autophagosomes close to the vacuole (Figure 13 K), there were none associated with vacuolar loops (Figure 13 L).

From the presented results we concluded that provacuole formation neither depends on Golgi function nor on vesicles deriving from post-Golgi trafficking or membranes produced by the core autophagy machinery. However, in mutants of these transport routes provacuoles often displayed aberrant morphologies, suggesting at least a contributing function to their development. The most striking provacuole defects were observed upon ConcA treatment. On an ultra-structural level we found rare cases in which an ER membrane seemed to directly convert into provacuolar membranes strongly labeled by V-PPase antibodies (black arrowhead, Supplemental Figure 5 C). This showed that provacuoles can be directly linked to the ER.

In vivo visualization of provacuoles

CLSM time-lapse imaging together with IEM of V-ATPases and V-PPases suggested that provacuoles represent not only a direct ER-to-tonoplast trafficking route, but might also provide the required membrane material for vacuole expansion during cell elongation. However, it is not certain whether provacuoles are rather permanent membrane connections or true intermediate compartments between the ER and the lytic vacuole. Our initial approach was to adjust the imaging of VHA-a3 fusion proteins together with the ER resident assembly factors, of which we know that they

biochemically interact (Graham et al., 2003; Neubert et al., 2008; Neubert, 2012). Since we did not record co-localization between VHA-a3-mRFP and AtVMA21-GFP under standard conditions (Figure 9 A, Supplemental Figure 6 A), we assumed that provacuole formation, their separation from the ER, and transit to the vacuole might be occurring too fast to be captured. A possible explanation could be the fluorophore maturation time of the fusion proteins. Depending on which fluorophore is used their maturation takes at least 5 to more than 100 minutes (Iizuka et al., 2011; Khmelinskii et al., 2012; Milo and Phillips, 2015). Our previous results were obtained with VHA-a3 fused to either eGFP (60 minutes maturation time, Sniegowski et al., 2005) or the slightly faster mRFP (40 minutes maturation time, Campbell et al., 2002). However, these values were determined at 37°C and are likely increased at ambient temperatures in which seedlings grow. From the VHA-a3-mRFP FRAP experiments (Figure 10) we can estimate a maturation half-time of about 120 minutes *in planta*. First, we created a situation where the formation of provacuoles is delayed long enough for the fluorophores of VHA-a3-GFP to mature. We incubated seedlings expressing VHA-a3-GFP and AtVMA12-mRFP for 24 hours at 4°C. Only sporadically, co-localization in thin concise tubular structures and aggregates was detected in provascular cells (yellow arrowheads in Supplemental Figure 6 B). Another approach was to create a VHA-a3 tandem fusion protein with superfolder-GFP (sfGFP, Khmelinskii et al., 2012) and mRFP. With this, we wanted to make use of different maturation kinetics in order to analyze the longevity of provacuoles and their mobility between ER and vacuole. It turned out that this fusion protein, too, was detected only at the tonoplast even though sfGFP is one of the fastest maturing fluorescent proteins available (Supplemental Figure 6 C). However, in order to investigate the dynamics as well as the transport and sorting mechanism of provacuoles in the future it is necessary to visualize these structures for *in vivo* live cell imaging.

We thus designed a system, termed PRV-tool01, that avoids fluorophore maturation time of VHA-a3-mRFP by inducibly transporting V-ATPases via provacuoles to the tonoplast together with an associated protein called VHA-AP2 (At3G24160). VHA-AP2 in *Arabidopsis* was already characterized in our laboratory during the course of a master thesis (Fink, 2012). Also, this protein was detected in a Co-IP of VHA-a3-GFP from tonoplast enriched membranes (by Görkem Patir Nebioglu, data not shown). In Col-0, the GFP fusion protein of VHA-AP2, similar to V-ATPases, localizes to the TGN/EE and the tonoplast (Figure 14 A). In the *vha-a2 vha-a3* double mutant lacking tonoplast localized V-ATPases (Krebs et al., 2010), VHA-AP2-GFP is localized to the TGN/EE and, more strikingly, a majority seems to be retained in the ER (Figure 14 B). We therefore assumed that the retained ER signal is the consequence of absent V-ATPases

not leaving the ER towards the tonoplast. Hence, excessive VHA-AP2-GFP was not removed from the ER and thus accumulated. We hypothesized that if we induce VHA-a3 expression in *vha-a2 vha-a3* mutants expressing VHA-AP2-GFP, V-ATPases destined for the tonoplast will be produced and transported there via provacuoles.

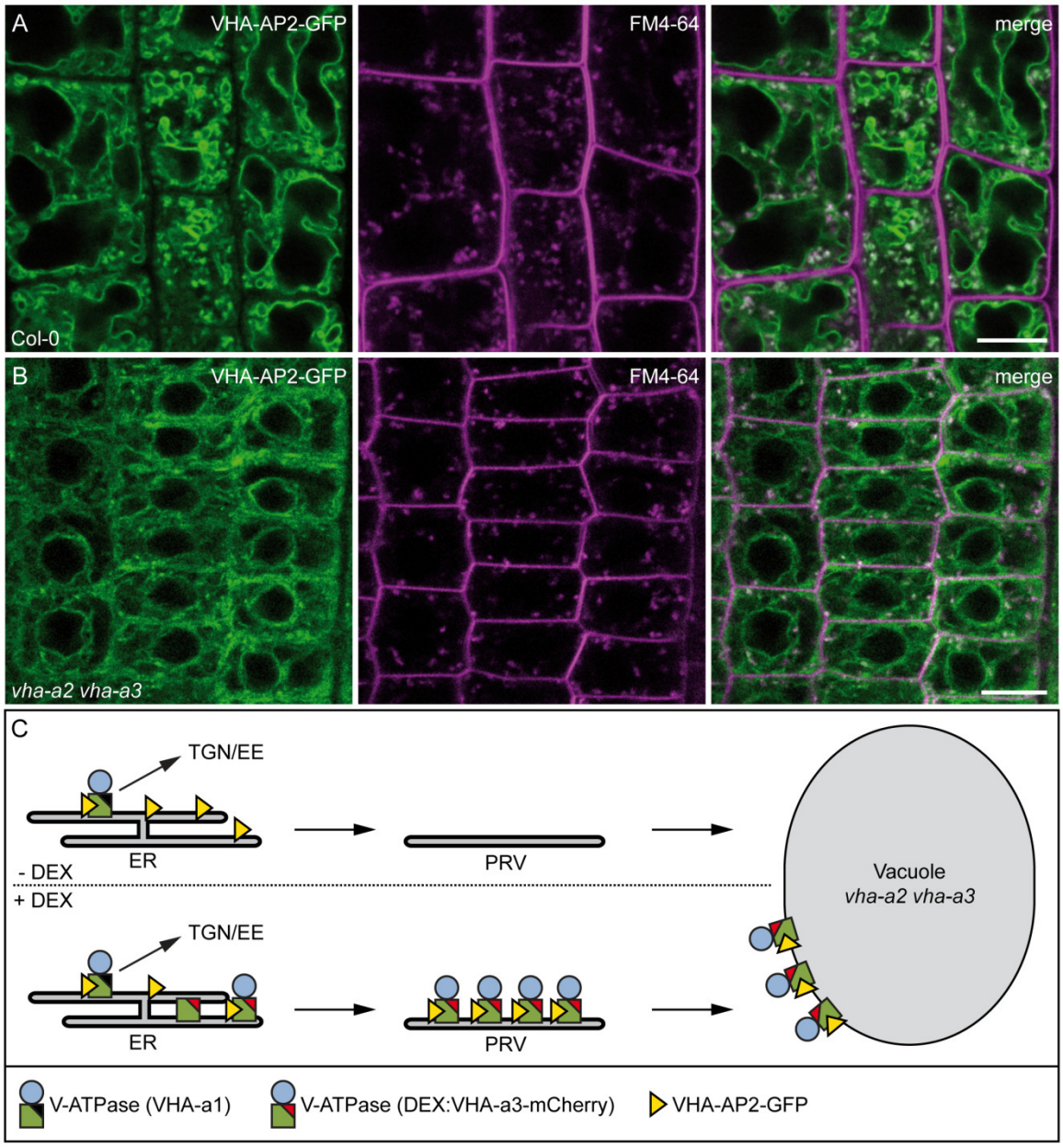

Figure 14: Development of a genetic tool to visualize provacuoles *in vivo*. Localization of VHA-AP2-GFP (green) in Col-0, co-staining with FM4-64 (magenta) 15 minutes after application (A). VHA-AP2-GFP signal in *vha-a2 vha-a3* double mutant background, co-stained with FM4-64 (B). Based on the hypothesis that VHA-AP2-GFP is co-transported together with fully assembled V-ATPases, we planned to inducibly express VHA-a3-mCherry in a *vha-a2 vha-a3* background expressing VHA-AP2-GFP (C). Upon induction, VHA-a3-mCherry subunits are produced, incorporated into V-ATPase complexes and then transported to the tonoplast via provacuoles. The V-ATPases containing VHA-a3-mCherry would take along VHA-AP2-GFP. Since the GFP fluorophores are already fully matured at the start of induction, there should be detectable GFP signal in provacuoles. Scale bars indicate 10µm.

The population of already fluorescent, but ER-retained VHA-AP2-GFP would exit the ER along with the newly synthesized V-ATPases. Thus, emerging provacuoles would be marked regardless of the maturation time of the VHA-a3 fusion protein (Figure 14 C).

For the PRV-tool01 we generated a Dexamethasone-inducible (DEX) VHA-a3-mCherry fusion protein. Once VHA-AP2-GFP labeled provacuoles fuse with the existing vacuolar network, the GFP signal would merge with subsequently matured VHA-a3-mCherry signal at the tonoplast. First, we confirmed the partial ER-retention of the VHA-AP2-GFP signal in uninduced *vha-a2 vha-a3* mutants transformed with the DEX inducible VHA-a3-mCherry. As observed before (Figure 14 B), VHA-AP2-GFP localized to punctae and the ER (Figure 15 A). The ER signal was comparable to that of the established ER localized V-ATPase assembly factor AtVMA21-GFP (Figure 9 B, Neubert et al., 2008). This AtVMA21-GFP pattern was not affected by prolonged incubation with DEX (Figure 15 C), serving as a control to rule out unspecific DEX effects on ER morphology. After 6 hours of induced VHA-a3-mCherry expression, the ER pattern of VHA-AP2-GFP did not change (Figure 15 D). The outline of the nuclear envelope and the TGN/EE punctae were still visible, while the VHA-a3-mCherry fluorescence was hardly detectable at all. After 24 hours of DEX induction VHA-a3-mCherry was located at the tonoplast, co-localizing with a faint signal of VHA-AP2-GFP (Figure 15 E). However, the majority of the GFP fluorescence was still detected in dots and the ER. The amount of tonoplast localized VHA-AP2-GFP was strongly increased 48 hours after induction (Figure 15 F). While the punctuate TGN/EE signal was unaffected, there was barely any ER signal left. This indicated that the induced expression of VHA-a3-mCherry, i.e. the newly produced vacuolar V-ATPases, resulted in a shift of VHA-AP2-GFP localization comparable to the Col-0 situation. Taken together, the transport and localization of VHA-AP2-GFP at the tonoplast seems to depend on the presence of VHA-a3 containing V-ATPases.

Focusing on cells of the transition zone, we searched for independent VHA-AP2-GFP signal that could mark putative provacuolar structures. In these cells, an increased amount of newly synthesized tonoplast material is required as they are about to elongate rapidly along with the contained vacuoles. We found independent tubular structures 48 hours after induction of VHA-a3-mCherry expression (Figure 16 A, arrowheads). The GFP fluorescence of these structures did not co-localize with the tonoplast signal of VHA-a3-mCherry. Morphologically, these GFP-labeled membranes were different from the more diffuse ER signal we observed before (Figure 15 A to D). In addition, we recorded events where both, the putative provacuole and the tonoplast were in contact with each other but merged only partially (Figure 16 B). This example featured a tubular structure exclusively labeled with VHA-AP2-GFP (Figure 16 B, closed white arrowheads)

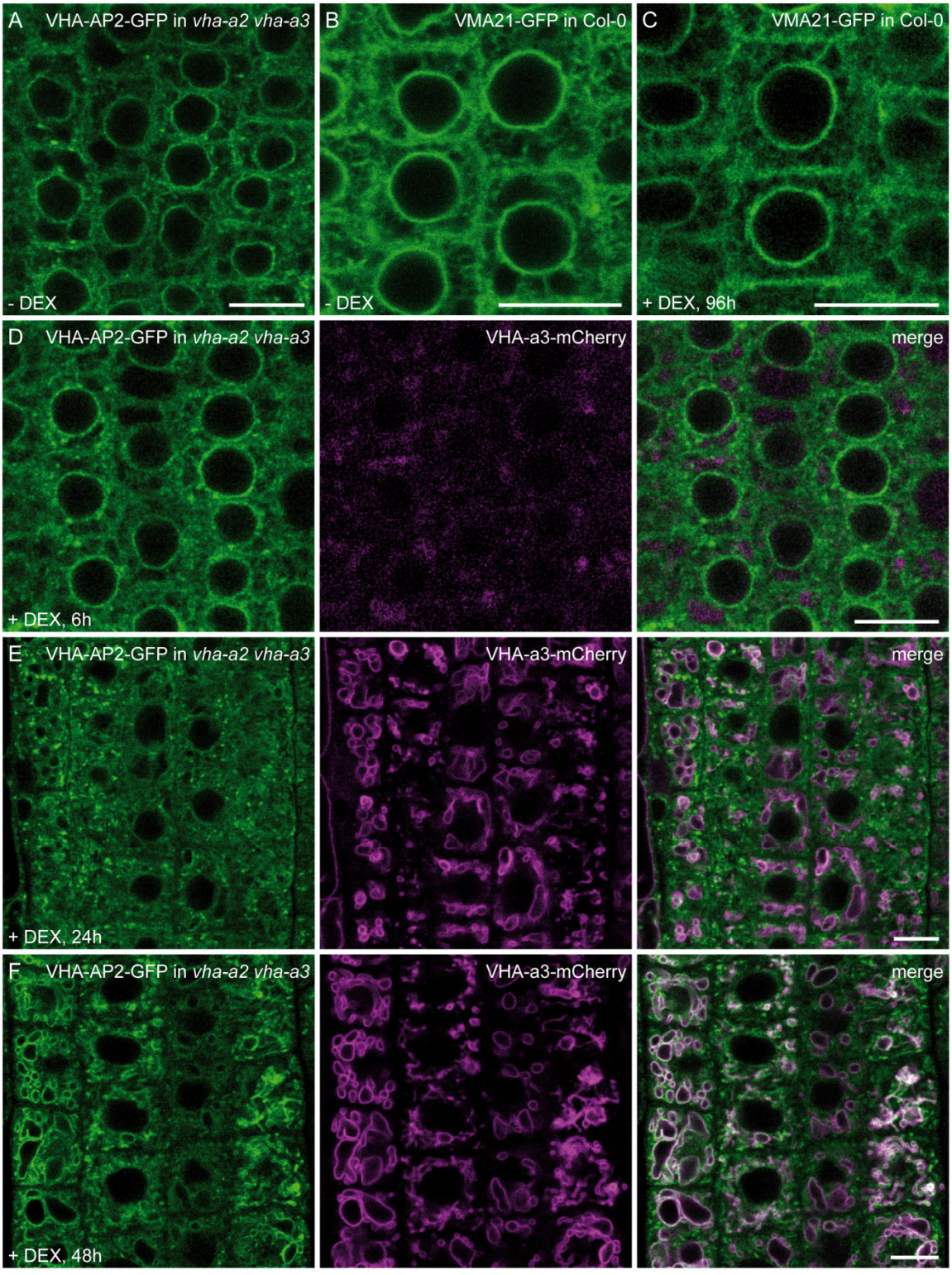

Figure 15: VHA-AP2-GFP is co-transported to the tonoplast with V-ATPases. Localization of VHA-AP2-GFP in *vha-a2 vha-a3* transformed with DEX:VHA-a3-mCherry under control conditions (A). The ER signal matches with that of VMA21-GFP (B). VMA21-GFP signal after 96 h treatment with 30 µM DEX (C). After 6 hours of DEX induction there is faint VHA-a3-mCherry signal detectable (D). VHA-AP2-GFP localization is not changed. 24 hours after induction the signal of VHA-AP2-GFP increases at the tonoplast, co-localizing there with VHA-a3-mCherry (E). 48 hours after DEX induction VHA-AP2-GFP is localized at the tonoplast along with VHA-a3-mCherry (F). Scale bars indicate 10 µm.

changing into a membrane that was also labeled with VHA-a3-mCherry (Figure 16 B, open white arrowheads). We hypothesized that such a distribution occurs during fusion of a provacuole and the tonoplast.

Taken together, the PRV-tool01 turned out to function as intended. We were now wondering if we can use this system to analyze provacuoles in a complete cellular context, in order to investigate their function in vacuole biogenesis.

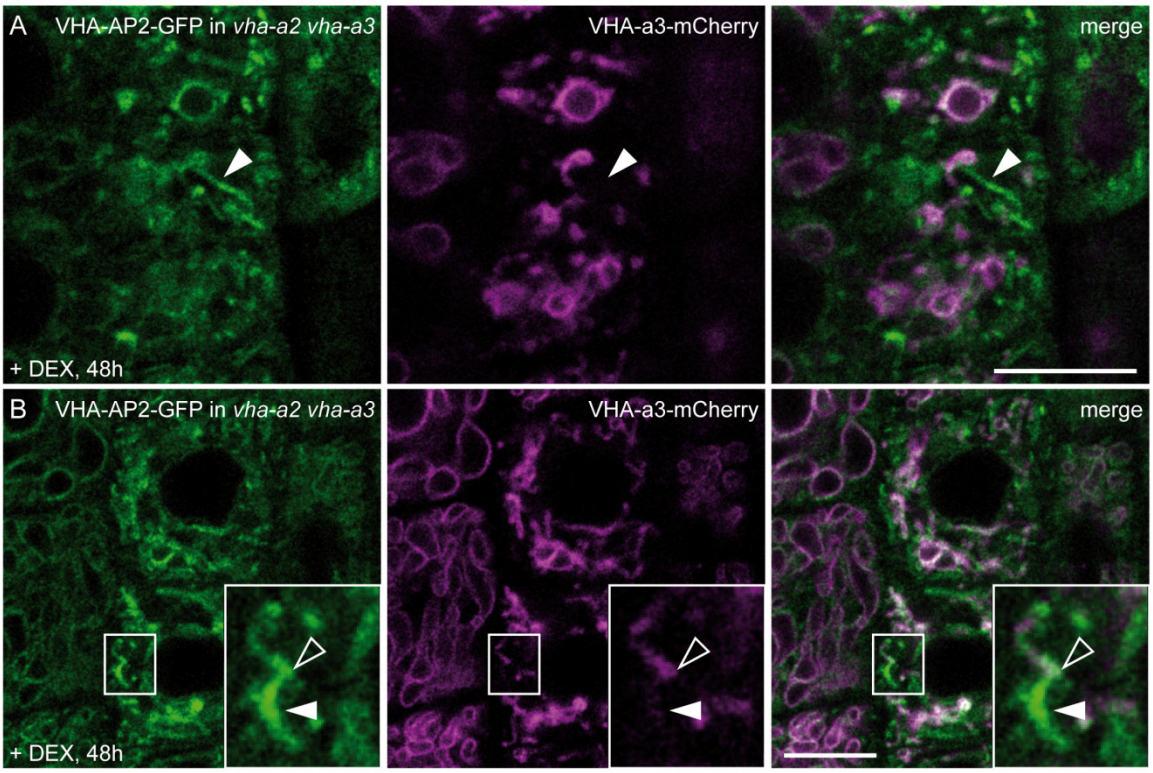

Figure 16: VHA-AP2-GFP marks provacuolar compartments upon induced expression of VHA-a3-mCherry. After 48 hours of induction, VHA-AP2-GFP can be detected in tubular structures that are independent of the tonoplast localized VHA-a3-mCherry signal (A; white arrowheads). These structures are considered to be provacuoles. We also observed membrane stretches that were exclusively labeled with VHA-AP2-GFP (B; closed white arrowheads) but seem to be in contact with the tonoplast marked by the fluorescence of VHA-a3-mCherry (B; open white arrowheads). Scale bars indicate 10 µm.

Provacuoles are the major supplier of new tonoplast membrane

For a more precise morphological description of provacuoles we investigated seedlings of the PRV-tool01 with a Zeiss LSM 880 AiryScan super-resolution microscope. We analyzed how much independent membrane material is present in addition to the tonoplast. As before, after 48 hours of induction, we observed tubular provacuoles only labeled with VHA-AP2-GFP running along VHA-a3-mCherry labeled tonoplast (Figure 17 A, closed white arrowheads). Besides, in single optical sections a part of the GFP signal seemed to spread over a wider area instead of forming tubules (Figure 17 A, open white arrowhead). Orthogonal representations of Z-stacks revealed that the tubular appearing VHA-AP2-GFP signal actually formed membrane sheets (Figure 17 B, white

arrowheads). In order to create 3D representations of the VHA-AP2-GFP labeled provacuoles it was necessary to extract only the discrete GFP signal. We subtracted the VHA-a3-mCherry signal from that of VHA-AP2-GFP (Figure 17 C), thereby erasing its additional tonoplast signal. Then, we projected the entire cell volume to visualize all provacuoles together with the TGN/EEs (Figure 17 D). As it turned out, the GFP labeled provacuoles predominantly form membranous sheets (Figure 17 D, white arrowhead).

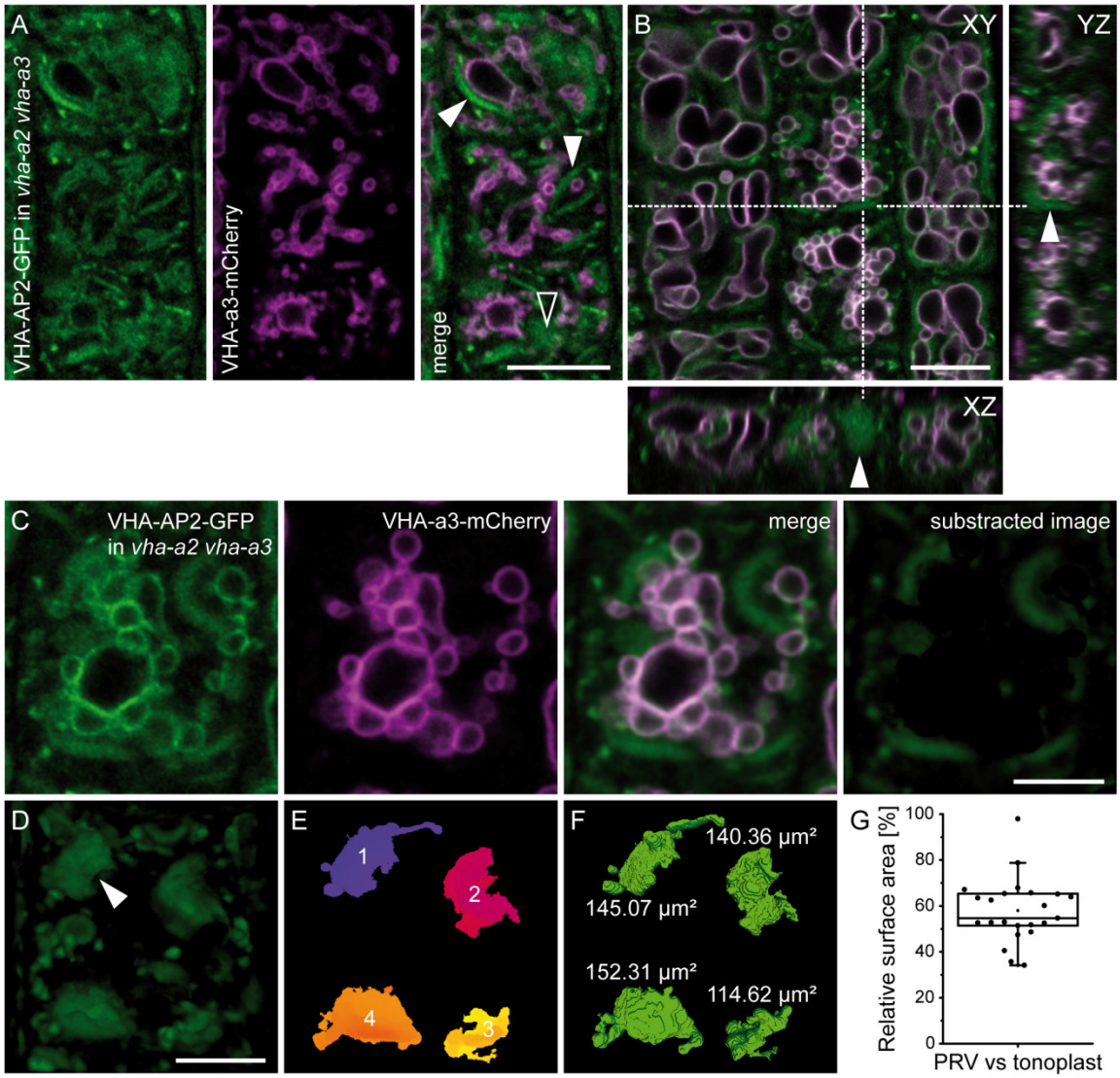

Figure 17: VHA-AP2-GFP labeled provacuoles form membrane sheets. Super-resolution microscopy of the PRV-tool01 48 hours after DEX induced expression of VHA-a3-mCherry. Single optical section showing distinguishable punctae and membrane stretches labeled solely with VHA-AP2-GFP (A). Orthogonal views of a Z-stack, the plane of view is indicated by the dotted line (B), demonstrating the sheet-like morphology (white arrowheads) of the tubular appearing VHA-AP2-GFP signal visible in the single XY plane. Single cell section showing the GFP and mCherry channel independently, as merged and as substracted image (C). The VHA-a3-mCherry signal was substracted from the VHA-AP2-GFP signal, thereby depicting only the independent VHA-AP2-GFP signal. Maximum projected Z-stack of the extracted VHA-AP2-GFP signal (D), the white arrowhead marks a sheet-like provacuole. Size-filtered annotation of individual provacuoles (E) was used to compute their individual surface area (F). Quantification of the relative surface area of all provacuoles to the corresponding tonoplast within single cells (G). Data depicted in a boxplot of n = 23 cells. Scale bars indicate 10 µm in A and B, 5 µm in C and D.

The size and morphology of these structures discriminated them from the TGN/EE compartments. To rule out that the observed provacuoles are artifacts caused by the induced expression of unusually high amounts of V-ATPases containing VHA-a3-mCherry, we analyzed EM sections of wildtype seedlings (Supplemental Figure 7). Here, we confirmed that provacuoles can become much bigger than previously shown (Figure 12). We specifically extracted provacuoles with a size-filter using "3D Objects Counter v2.0" (Bolte and Cordelieres, 2006; Figure 17 E). As a result, segmented and annotated structures were generated from which the surface area was calculated on the basis of the original pixel size (Figure 17 F). These values were compared to the already existing tonoplast membrane based on the recorded VHA-a3-mCherry signal (Figure 17 G). Surprisingly, the average amount of independent provacuole membrane surface within elongating cells accounted for almost 58% of the already existing tonoplast surface. With a Pearson's R-value of 0.84 both features were strongly correlated in all evaluated cells (Supplemental Figure 8 A). The mean surface area of a single provacuole was about 136 µm², but the individual values ranged from 22 µm² up to 971 µm² (Supplemental Figure 8 B). Due to this variation we classified the results to determine a reliable size distribution. Provacuoles with a size up to 100 µm² were most frequent (58 %), followed by 21 % between 100 µm² and 200 µm² (Supplemental Figure 8 C). In 11 % of all provacuoles the surface area exceeded 300 µm². Moreover, the total surface area and the number of provacuoles per cell correlated strongly with an R-value of 0.95 (Supplemental Figure 8 D). These results suggested that even though provacuoles are initially produced as small entities they do not accumulate in high numbers but instead seem to form bigger structures before they fuse with the vacuole. As a consequence, rapid tonoplast expansion during cell elongation would require far less fusion events with provacuoles than with MVB/LEs.

We further used the new values to update the model calculation of the membrane contribution to tonoplast expansion (Figure 18). Taking into account that about 60 % of the necessary membrane surface are covered by provacuoles, the membrane amount that needs to be provided by MVB/LEs decreased to 490 µm². In turn, this led to an increased maximum MVB/LE lifetime of 750 s, or 12.5 minutes, which is in agreement with our experimental data (Figure 8) and previously published results from mammalian cells (10 to 15 minutes, Rink et al., 2005). According to these calculations provacuoles seem to be the major membrane reservoir which provides the majority of newly synthesized tonoplast membrane during cell elongation. Interestingly, the relatively constant number but increasing size of individual provacuoles in elongating cells suggest that these compartments are able to undergo homotypic fusion before they make contact

with the existing vacuolar network. Establishing the contact between a provacuole and the lytic vacuole would further require a membrane fusion event.

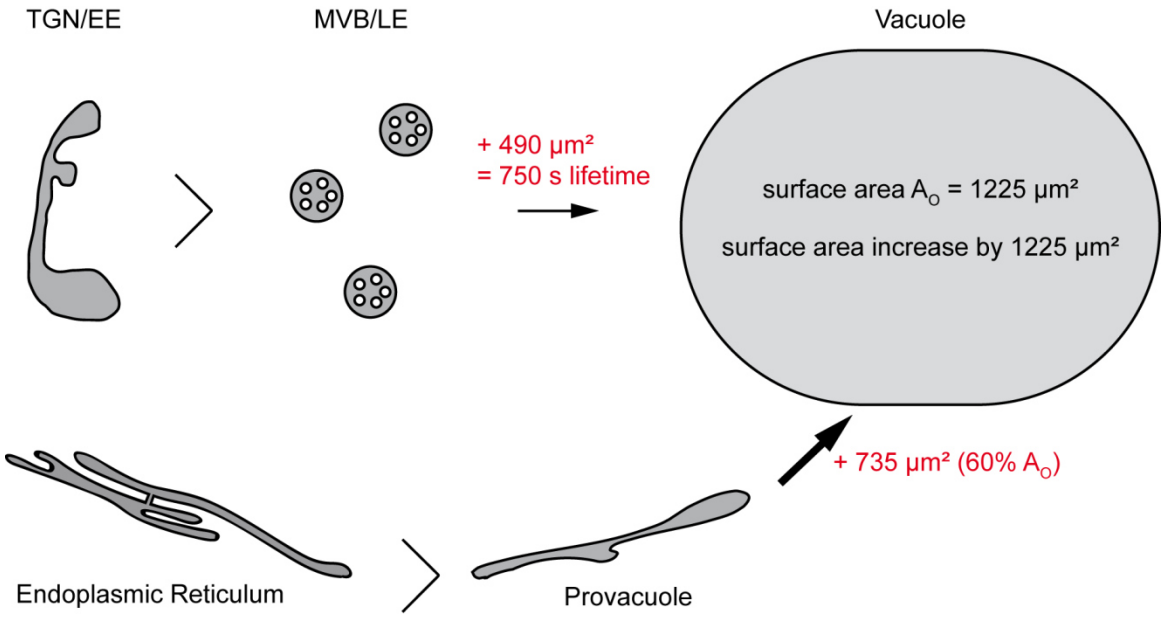

Figure 18: Membrane contribution of MVB/LEs and provacuoles to tonoplast expansion. Considering provacuoles to hold ready approximately 60% of the present vacuole surface we updated the model calculation for the delivery of new vacuole membrane during the initial elongation of an epidermal root cell (Figure 8 E). To increase the tonoplast surface area (A_O) by 1225 µm², 490 µm² would have to be provided by MVB/LEs fusing with the vacuole. Due to this, their allowed lifetime increases to 750 seconds which fits to the experimentally measured values (Figure 8).

Membrane tethering complexes are required for vacuole development

Next, we investigated which factors promote the formation and development of provacuoles. Assuming that provacuoles are constantly produced at the ER but are not permanently connected to the vacuole, they have to fuse at some point with the already existing vacuole. The bigger the tonoplast surface in elongating cells becomes, the more the total surface area of provacuoles increases as well (Supplemental Figure 8 A). Instead of accumulating more individual provacuoles they enlarge (Supplemental Figure 7), presumably due to homotypic fusion. Membrane fusion with the vacuole in yeast requires the HOPS tethering complex (reviewed in Balderhaar and Ungermann, 2013). In *Arabidopsis* all homozygous T-DNA knockout lines of HOPS subunits are embryo lethal. To study the role of this membrane tethering complex in vacuole biogenesis we had to circumvent the embryo lethality of the T-DNA insertion lines. Therefore, we designed a DEX-inducible artificial micro-RNA (amiR; Schwab et al., 2006) knockdown construct against one *Arabidopsis* homolog of a structural HOPS subunit, VPS16.

We analyzed the knockdown effect of amiR-*vps16* in different root zones 72 h after DEX induction, compared to wild type and uninduced amiR-*vps16* seedlings. In both controls, Col-0 (Figure 19 A) and uninduced amiR-*vps16* (Figure 19 B), vacuoles of the

meristematic and elongation zone displayed the typical complex tubular morphology (compare to Figure 4 - Figure 7). In the early and late root differentiation zone unaltered central vacuoles were observed. However, upon induced knockdown of VPS16 we found severely affected vacuoles (Figure 19 C, Supplemental Figure 9). Instead of being tubular or fully inflated, lytic vacuoles appeared as isolated sphere-like compartments. This aberrant phenotype persisted along the further developed root zones and correlated with the duration of induction. However, cells in anterior parts of the root did not show vacuole fragmentation. We then investigated whether the affected vacuoles were isolated due to impaired membrane fusion or still able to establish tubular connections as to a certain extend in LatA-treated cells (Figure 7).

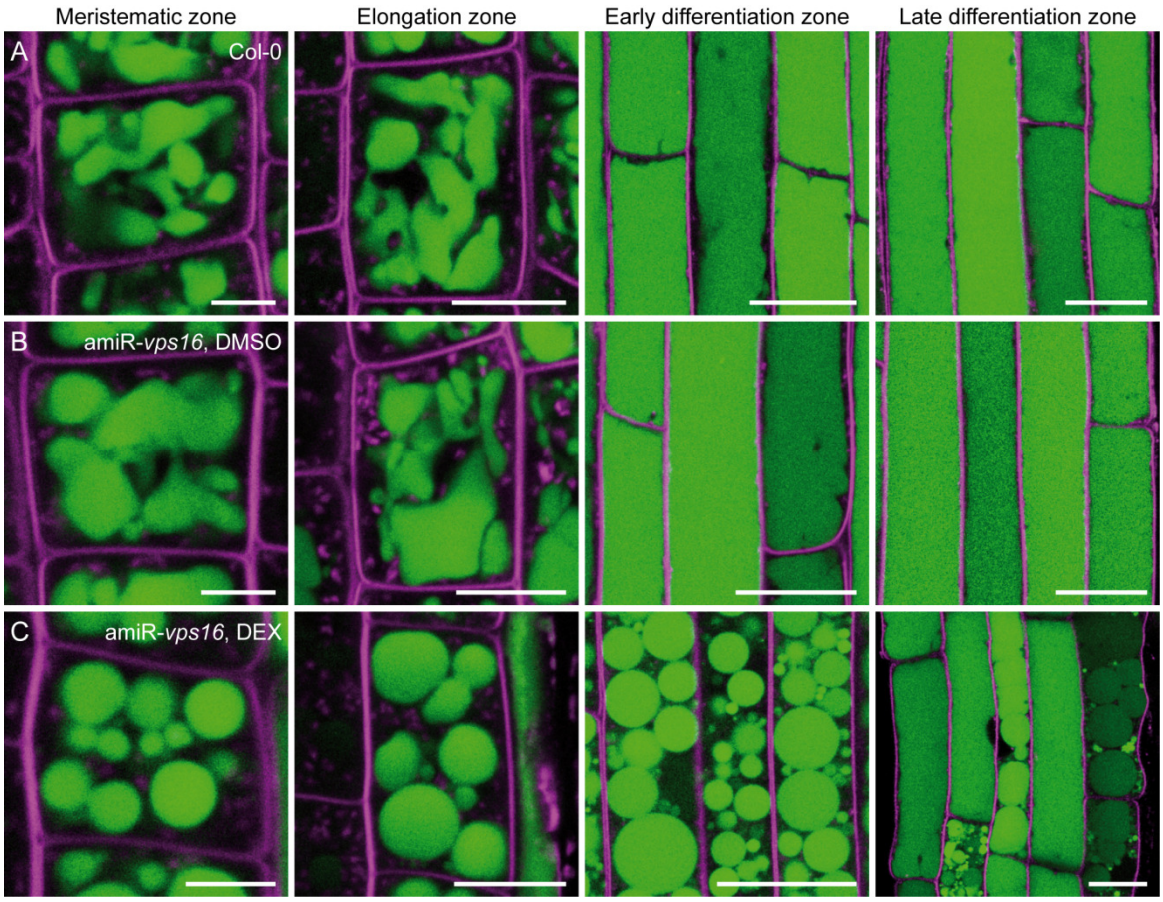

Figure 19: Induced knockdown of VPS16 leads to vacuole morphology defects. CLSM images of 5-days-old *Arabidopsis* seedlings that were incubated for 72 h in liquid 1/2 MS medium supplemented with the indicated substances. The seedlings were stained with BCECF (green) and FM4-64 (magenta). The images depict representative cells of the meristematic, elongation as well as early and late differentiation zone. Lytic vacuoles of Col-0 (A) and uninduced DMSO-treated amiR-*vps16* cells (B) of the meristematic and elongation zone displayed a normal tubular morphology. After 72 h of Dexamethasone (DEX) induction in amiR-*vps16* (C), the morphology of vacuoles appeared as spherical isolated compartments. Note that the morphology defects became less pronounced in the late differentiation zone. Scale bars indicate 5 µm (meristematic zone), 10 µm (elongation zone) and 20 µm (early and late differentiation zone).

In addition, three other mutants with comparably abnormal vacuole phenotypes were analyzed, *zig1-1* (Yamauchi et al., 1997; Kato et al., 2002), *itt3* (Zheng et al., 2014b) and *gfs9-3* (Ichino et al., 2014) (Figure 20 A). GFS9 encodes a *Drosophila melanogaster*

ortholog of *endosomal maturation defective* (ema; Ichino et al., 2014). EMA was shown to directly interact with Vps16A of the HOPS complex and to be important for late endosomal maturation as well as autophagosome development (Kim et al., 2010, 2012a). 3D surface renderings confirmed the presence of sphere-like lytic vacuoles in all tested genotypes and the DEX-induced amiR-*vps16* line (Figure 20 B).

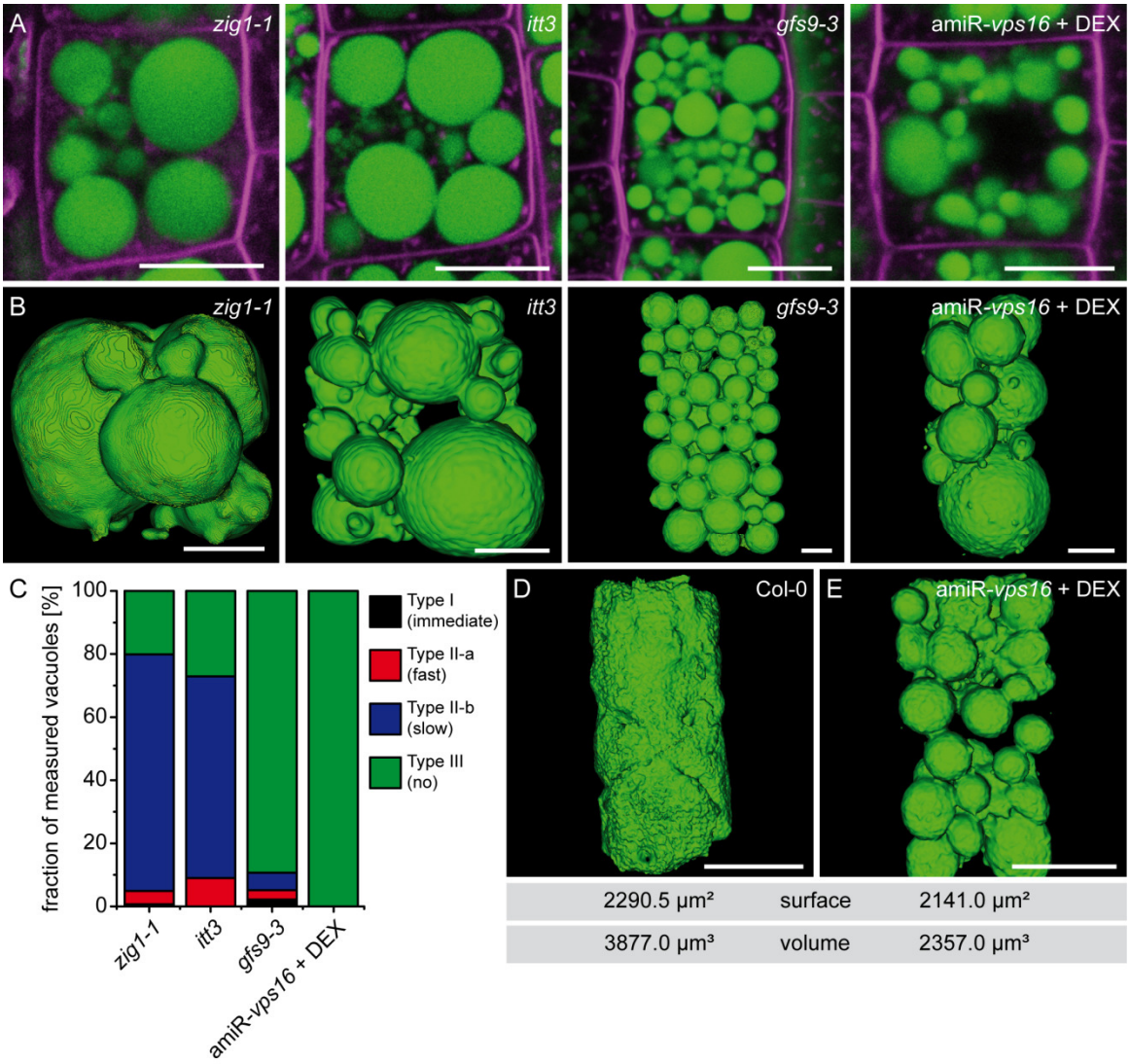

Figure 20: Vacuoles in induced amiR-*vps16* cells are isolated. (A) Representative single optical sections of the indicated genotypes that were stained with BCECF (green) and FM4-64 (magenta). The depicted cells share an abnormal vacuole phenotype of several seemingly independent and rounded vacuoles. Surface renderings of representative Z-stacks of the indicated genotypes were computed in (B) to judge if the vacuoles are interconnected. We further used the quantitative vaccFRAP method to measure vacuole connectivity (C). The graph summarizes the distribution of all measured vacuoles according to the previous model (Figure 7) with n = 144 (*zig1-1*), n = 155 (*itt3*), n = 233 (*gfs9-3*), and n = 190 (amiR-*vps16* + DEX). Surface renderings of lytic vacuoles of Col-0 and induced amiR-*vps16* cells (D). The volume of the amiR-*vps16* vacuole was reduced by 40% whereas the surface area of both compartments was similar. Scale bars indicate 5 µm (A) and (B) and 10µm in (D).

To determine the connectivity of the observed vacuoles, we examined them with the vaccFRAP method. Our measurements showed that compared to wild type cells (Figure 7 D), the amount of slowly recovering vacuoles of Type II-b strongly increased by at least

50 % in both, *zig1-1* and *itt3* (Figure 20 C). Surprisingly, about 73 % to 80 % of all assessed vacuoles were still connected but exhibited highly increased recovery half-times (Supplemental Figure 10). These results were contrary to a previous report showing that vacuoles in *itt3* root cells are independent organelles, based on the fluorescence recovery of a tonoplast integral protein (Zheng et al., 2014a). In contrast, the portion of isolated vacuoles in *gfs9-3* mutants was approximately 89 %. In DEX-induced amiR-*vps16* seedlings all examined vacuoles were isolated.

When we compared the volume and surface area of vacuoles of Col-0 and induced amiR-*vps16* cells of the same size, we found that the amount of tonoplast surface was similar (Figure 20 D and E). The changed morphology of the vacuoles resulted in an ca. 40 % reduced volume. We concluded that the membrane tethering by HOPS is essential for the proper development of lytic vacuoles. The observed spherical vacuoles would be the direct consequence of their impaired fusion competence. Nevertheless, the induced knockdown does not seem to interfere with the synthesis of vacuole membrane material at the ER itself.

VPS16 knockdown prevents V-ATPase trafficking to the vacuole

We hypothesized that *VPS16* knockdown should also affect the transport of V-ATPases to the vacuole. To test this, we crossed the amiR-*vps16* line with VHA-a3-mRFP. Under control conditions, the VHA-a3-mRFP signal displayed the well established tonoplast signal (Figure 21 A; compare to Figure 9, Figure 15 and Figure 17). After 48 h of DEX induction the morphological change of lytic vacuoles occurred, visualized by the tonoplast labeling of VHA-a3-mRFP (Figure 21 B). In addition, small VHA-a3-mRFP punctae became noticeable. When we induced the seedlings for 96 h the tonoplast labeling of VHA-a3-mRFP was completely absent while the majority of RFP fluorescence was present in dots dispersed throughout the cytoplasm (Figure 21 C). We also detected a faint signal at the plasma membrane. Taken together, *VPS16* knockdown inhibited the trafficking of V-ATPases destined for the tonoplast.

In order to verify these findings we performed vacuole pH measurements using BCECF. If the tonoplast is devoid of V-ATPases after prolonged *VPS16* knockdown we should be able to measure an alkalinization of the vacuolar volume. Vacuoles of Col-0, amiR-*vps16* and amiR-*vps16* x VHA-a3-mRFP lines were compared upon mock treatment with DMSO and inducing conditions with DEX for 48 h and 96 h, respectively.

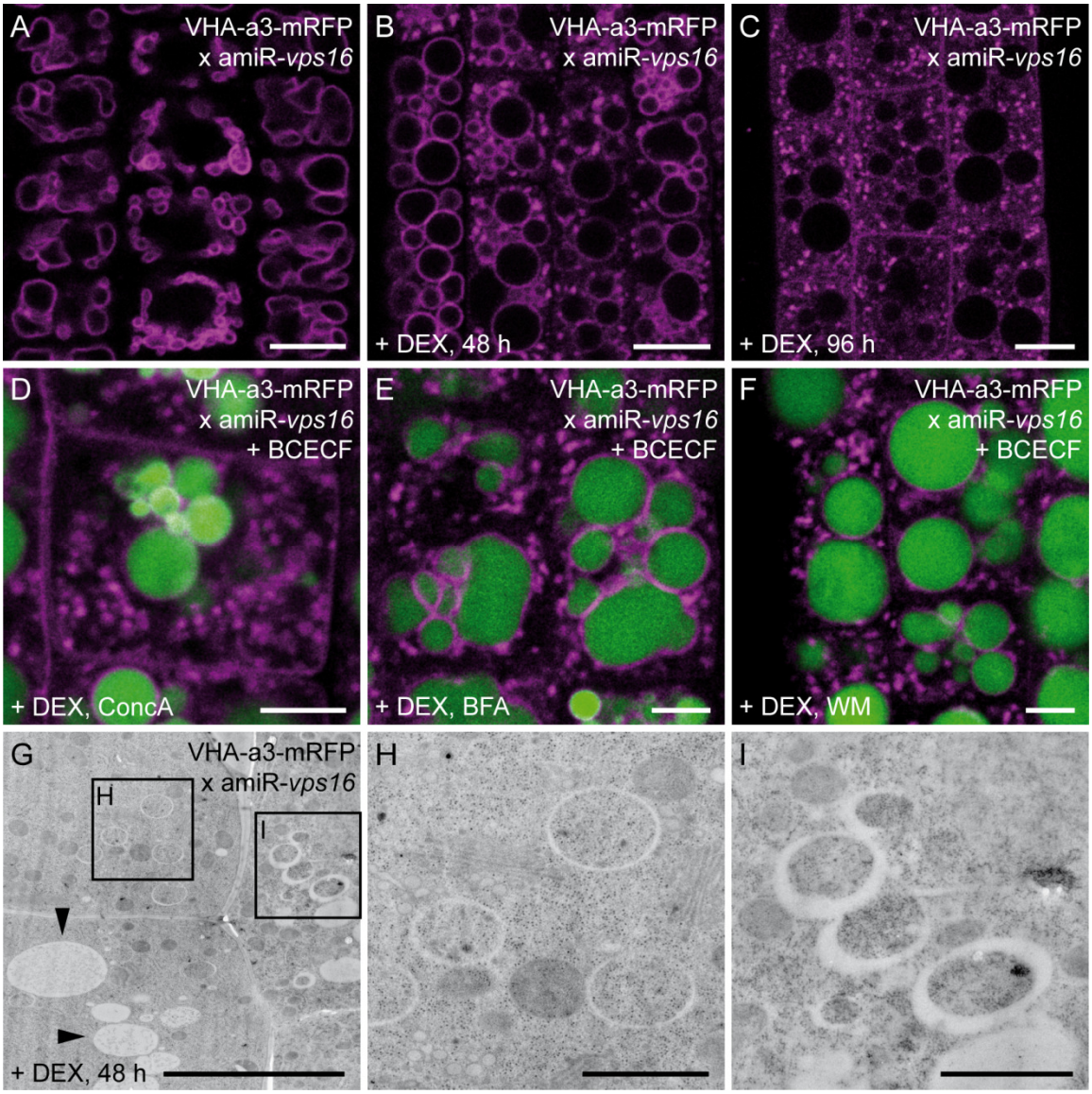

Figure 21: *VPS16* knockdown prevents V-ATPase trafficking to the vacuole. We analyzed crosses of amiR-*vps16* with VHA-a3-mRFP. Under control conditions VHA-a3-mRFP labeled the tonoplast (A). 48 h after DEX induction spherical vacuoles and small VHA-a3-mRFP punctae in the cytosol were observed (B). After 96 h of induction vacuoles were devoid of fluorescently labeled V-ATPases whereas the number of VHA-a3-mRFP positive dots further increased (C). In order to identify the compartments of the punctate RFP signal we applied different endosomal inhibitors after 48 h of DEX induction to affect the morphology of the TGN/EE (ConcA; D), Golgi and TGN/EE (BFA; E) and MVB/LE (WM; F). Root tips of 48 h induced amiR-*vps16* x VHA-a3-mRFP seedlings were preselected by CLSM to show the punctate RFP signal and subsequently processed for EM. The EM images show the sphere-like appearance of lytic vacuoles (arrowheads, G) as well as different circular double-membrane structures highly reminiscent of provacuoles (boxed sectors in G). Magnified images of the framed sectors show the provacuole-like structures with very thin (H) and slightly increased lumen (I). Scale bars indicate 10 µm in A to C, 5 µm in D to G and 1 µm in H and I. EM with Dr. Stefan Hillmer.

We measured a vacuolar pH of about 6.0 for Col-0 and both DMSO treated amiR-*vps16* lines (Supplemental Figure 11 A). In contrast, the average pH value of amiR-*vps16* and the crossing with VHA-a3-mRFP after 48 h DEX induction was at approximately pH 6.3. After 96 h of induction the pH increased to 6.7 for amiR-*vps16* and pH 6.5 for amiR-*vps16* x VHA-a3-mRFP. Wondering about this difference, we noticed that after 96 h of DEX induction not all of the vacuoles were without VHA-a3-mRFP labeling. We thus

separately determined the values for cells with and without VHA-a3-mRFP signal at the tonoplast, we found that the alkalinization to pH 6.7 directly correlated with the absence of tonoplast V-ATPases (Supplemental Figure 11 A).

According to our working hypothesis that fusion of provacuoles with the vacuole require functional HOPS complexes, VHA-a3-mRFP punctae after 48 hours of *VPS16* knockown might be accumulated provacuoles. However, their morphology was similar to other endosomes, e.g. MVB/LEs or TGN/EEs (compare to VHA-a1-GFP labeling of TGN/EE in Figure 9 B). To narrow down the nature of these punctae, we treated induced and BCECF-stained seedlings with different inhibitors of endosomal trafficking. The punctate VHA-a3-mRFP signal did not respond to any treatment (Figure 21 D to F), suggesting that they are neither Golgi, TGN/EE nor MVB/LE. Subsequently, we prepared samples for EM of amiR-*vps16* x VHA-a3-mRFP seedlings induced for 48 h that had been preselected by CLSM to show the punctate RFP signal. On the ultra-structural level, we first confirmed the spherical morphology of the existing lytic vacuoles (arrowheads, Figure 21 G). Similar to the observations with CLSM, we found accumulations of circular double-membrane structures reminiscent of either provacuoles or autophagosomes (Figure 21 H and I).

Assuming that the dot-like accumulations were to some extend provacuoles, we wanted to find out if those structures were detached from the ER or still carried V-ATPase assembly factors. We thus created a double marker line of VHA-a3-mRFP and VMA21-GFP crossed with amiR-*vps16*. A detectable co-localization between both proteins upon induction would imply a residual connection to the ER, where VMA21 exclusively localizes to. Under non-inducing conditions, VHA-a3-mRFP and VMA21-GFP localized to the tonoplast or the ER, without fluorescence overlap (Supplemental Figure 11 B). Upon DEX treatment for 48 h the strong morphological change of the vacuole was visible but did not lead to co-localization of VHA-a3-mRFP and VMA21-GFP (Supplemental Figure 11 C). In fact, even after prolonged DEX induction the VHA-a3-mRFP positive punctae did not co-localize at all with the VMA21-GFP signal still labeling the ER (Supplemental Figure 11 D). These results suggested that the presumable provacuoles labeled by VHA-a3-mRFP were not in contact with the ER further indicating that provacuoles are discrete compartments between ER and vacuole.

EMS mutagenesis screen to identify V-ATPase trafficking mutants

To understand the molecular mechanism of how provacuoles form at the ER and how V-ATPases allocated for the tonoplast are so efficiently sorted into this route, we performed a forward genetic screen to identify trafficking mutants of the provacuole transport route.

The working hypothesis was that impaired sorting of V-ATPases containing VHA-a2 and VHA-a3 subunits should lead to their retention in the ER since they do not contain a COPII export motif as VHA-a1 (PhD thesis of Upendo Lupanga, 2017). As a direct consequence, the mutant plants would lack tonoplast localized V-ATPases and should behave like *vha-a2 vha-a3* knockout plants. *vha-a2 vha-a3* mutants cannot properly sequester toxic ions from the cytosol into the vacuole, thus showing a reduced root elongation phenotype when grown on plates supplemented with $ZnCl_2$ (Krebs et al., 2010). Also, we recently demonstrated that in *vha-a2 vha-a3* VHA-a1-GFP containing V-ATPases do not re-localize from the TGN/EE to the tonoplast to complement for the missing V-ATPase activity (Kriegel et al., 2015).

Using ethyl methanesulfonate (EMS), we mutagenized seeds of plants expressing VHA-a3-GFP in order to later monitor possible ER retention with CLSM. We confirmed the efficiency of the mutagenesis by evaluating the occurrence of visual mutant traits, e.g. embryo lethality, growth retardation or albinism (Supplemental Figure 12 A). Possible mutants were preselected by growing them on vertical plates supplemented with 50 µM $ZnCL_2$ (Supplemental Figure 12 B). Only seedlings with a short root phenotype at least comparable to that of *vha-a2 vha-a3* mutant seedlings of the same age were analyzed with CLSM (Supplemental Figure 12 C).

A mutant with aberrant vacuoles - *big gloomy orb 1* (*bgo1*)

We identified a mutant with a selective VHA-a3-GFP trafficking phenotype. In cells of this mutant we found vacuole-like compartments that were not labeled with VHA-a3-GFP next to or tightly surrounded by vacuoles with GFP labeling (Figure 22 A, asterisks). With projected Z-stacks we demonstrated that they were not vacuolar inclusions but distinct compartments (arrowheads, Figure 22 B). As a working title we named the mutant after its most prominent feature when observed with CLSM: *big gloomy orb 1* (*bgo1*). In order to test whether these structures are indeed vacuoles, we tried to stain them with BCECF and Lysotracker-Red DND99. Both dyes should label either the lumen (BCECF) or the membrane (Lysotracker-red) of vacuoles. In M3 seedlings of *bgo1* mutants we could not detect any labeling of the abnormal compartments with BCECF (Figure 22 C and D) nor Lysotracker-red (Figure 22 E and F). However, based on the corresponding transmitted light images the observed structures displayed big membrane bound compartments with clear and watery content, matching the morphological definition of lytic vacuoles in plants. In EM images of root tips that were high-pressure frozen and freeze substituted, lytic vacuoles appear as bright areas with light grey texture due to their watery content (Hillmer et al., 2012, Supplemental Figure 4 A to F). In meristematic cells of *bgo1* roots

we observed at least one enlarged and round structure per cell with the characteristic bright appearance of lytic vacuoles (asterisks, Figure 22 F and G) in addition to typically shaped ones (arrowheads, Figure 22 F and G). This was consistent with the CLSM images in which we also found both vacuole types within all observed cells.

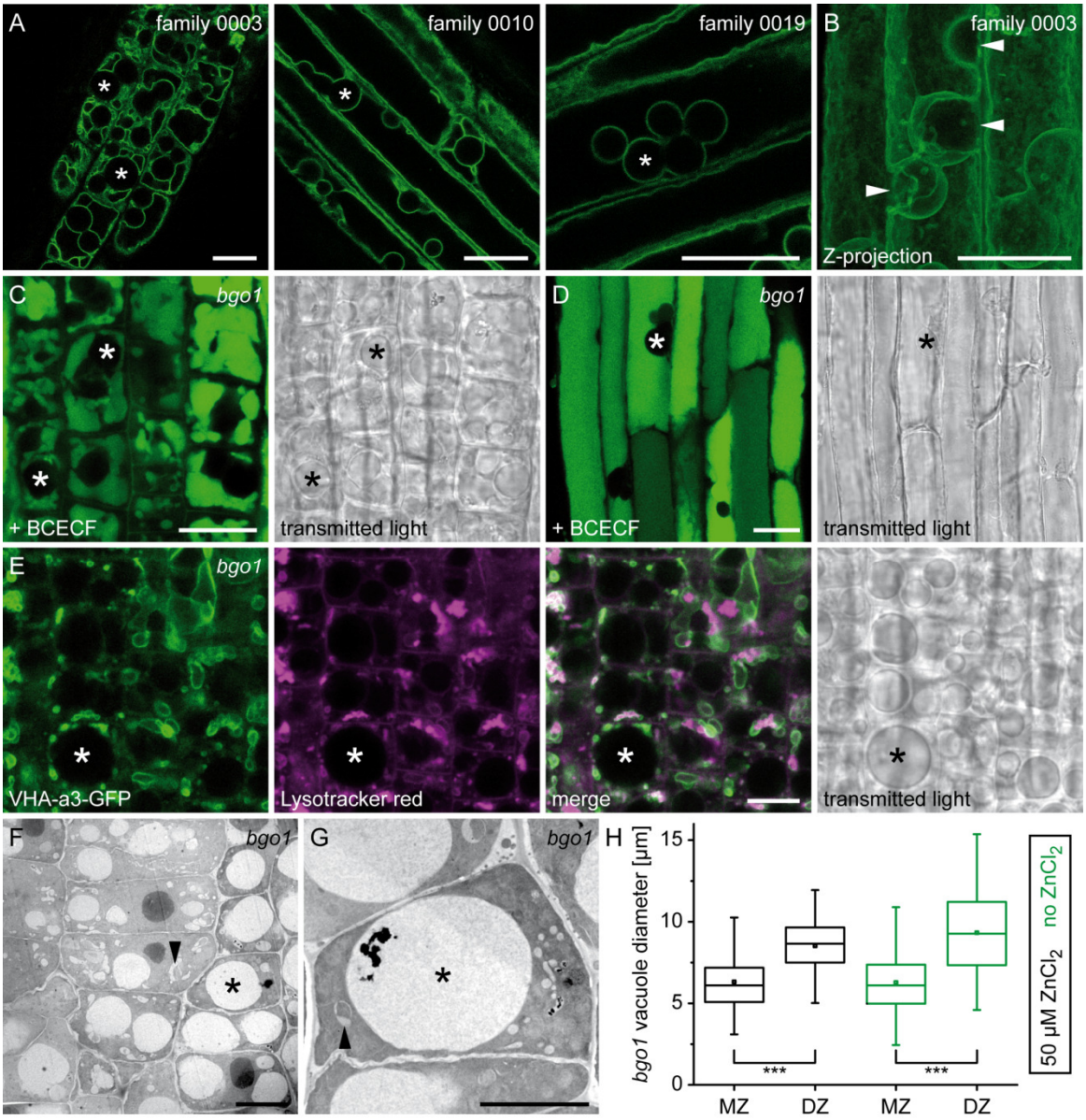

Figure 22: Aberrant vacuoles without VHA-a3-GFP labeling in the *big gloomy orb 1* (*bgo1*) mutant. In a CLSM-based screen for affected VHA-a3-GFP trafficking three particular seedlings of the indicated M2 family pools were identified that had abnormally big spherical structures without GFP-labeling (A, asterisks). The mutant was termed *big gloomy orb 1* (*bgo1*). A projected Z-stack shows that the structures are discrete compartments (arrowheads, B). The abnormal vacuoles (marked by asterisk) could not be stained with BCECF in meristematic (C) or differentiated cells (D). The same was true for Lysotracker-Red DND99 staining (Lysotracker red, E). High-pressure frozen and freeze-substituted root tips of *bgo1* mutants demonstrated the presence of the big vacuolar structures (asterisk) next to normal tubular lytic vacuoles (arrowhead) in meristematic cells and close to the quiescent center (F). A close-up of a cross-section of an epidermal cell showcases the unusually large size (G). Quantification of average diameter of the aberrant *bgo1* vacuoles in cells of the meristematic (MZ) and differentiation zone (DZ) both on plates with and without supplemented $ZnCl_2$ (H). *** indicate $p < 0{,}0005$ for n = 335 (MZ + $ZnCl_2$), 156 (DZ + $ZnCl_2$), 225 (MZ - $ZnCl_2$) and 166 (DZ - $ZnCl_2$) aberrant vacuoles in *bgo1* mutants. Scale bars indicate 20 µm in (A) to (D), 10 µm in (E) and 5 µm in (F) and (G). EM with Dr. Stefan Hillmer.

A striking feature of the aberrant vacuoles in *bgo1* mutants was their drastically increased size especially in meristematic root cells. We therefore analyzed the size of abnormal *bgo1* vacuoles comparing cells of the meristematic and differentiation zone with and without the addition of $ZnCl_2$. The diameter of *bgo1* vacuoles significantly increased in differentiated cells as opposed to those in meristematic cells (Figure 22 H), suggesting that these vacuoles, too, receive membrane material over time. Interestingly, the *bgo1* phenotype was not dependent on the addition of $ZnCl_2$.

Zusammenfassung

Supplementary Figures

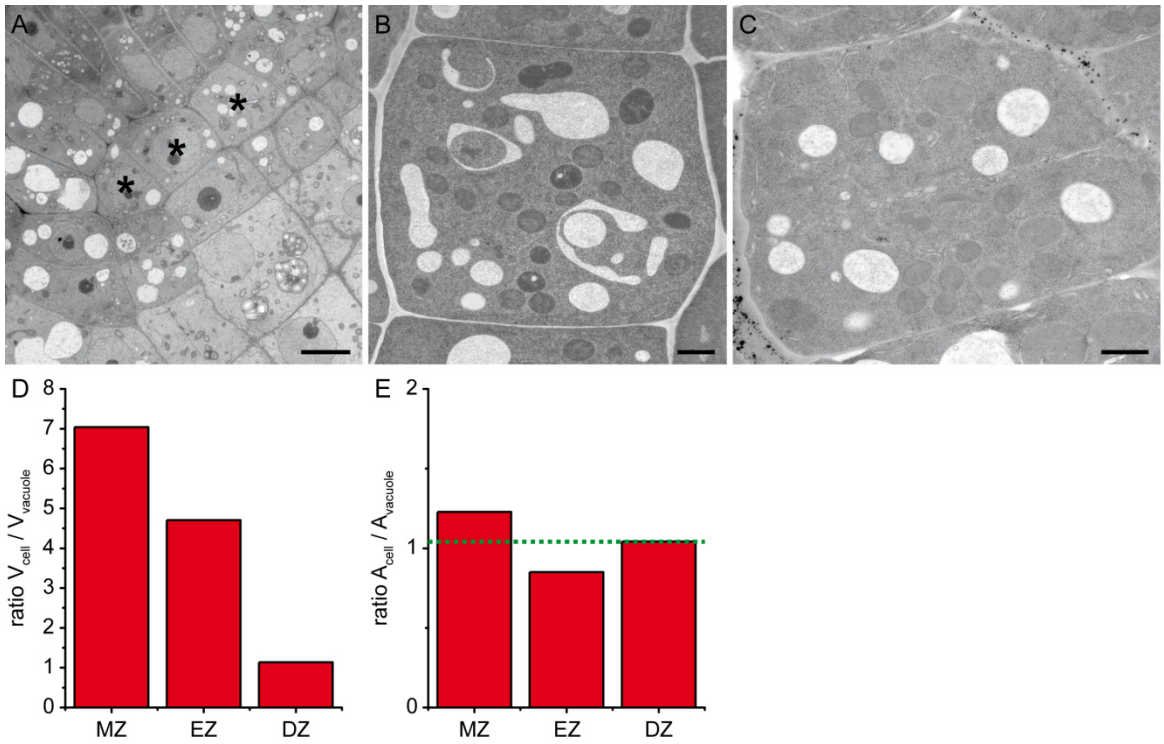

Supplemental Figure 1: Lytic vacuoles in the quiescent center and their development over time. Root tips of 5-days-old *Arabidopsis thaliana* seedlings were processed for EM. Ultra-thin sections show lytic vacuoles of variable sizes in all cells of the root meristem including the quiescent center (asterisks in A). In meristematic cells, vacuoles appear as multiple small compartments which did also form tubular stretches (B). In meristematic cells undergoing cell division vacuoles can also be observed (C). Based on 3D renderings of representative BCECF-stained vacuoles of the meristematic (MZ), elongation (EZ) and differentiation zone (DZ) we calculated the ratio of cell to vacuole volume (D) and surface area (E) of n ≥ 3 representative cells per zone. Independent of the vacuole volume the surface area of both, vacuole and plasma membrane is approximately 1 in cells over all root zones (dotted line in E). Scale bars indicate 4 µm in A and 1 µm in B and C. EM was performed by Dr. Corrado Viotti and Dr. Stefan Hillmer. A to C were published in Viotti et al., 2013.

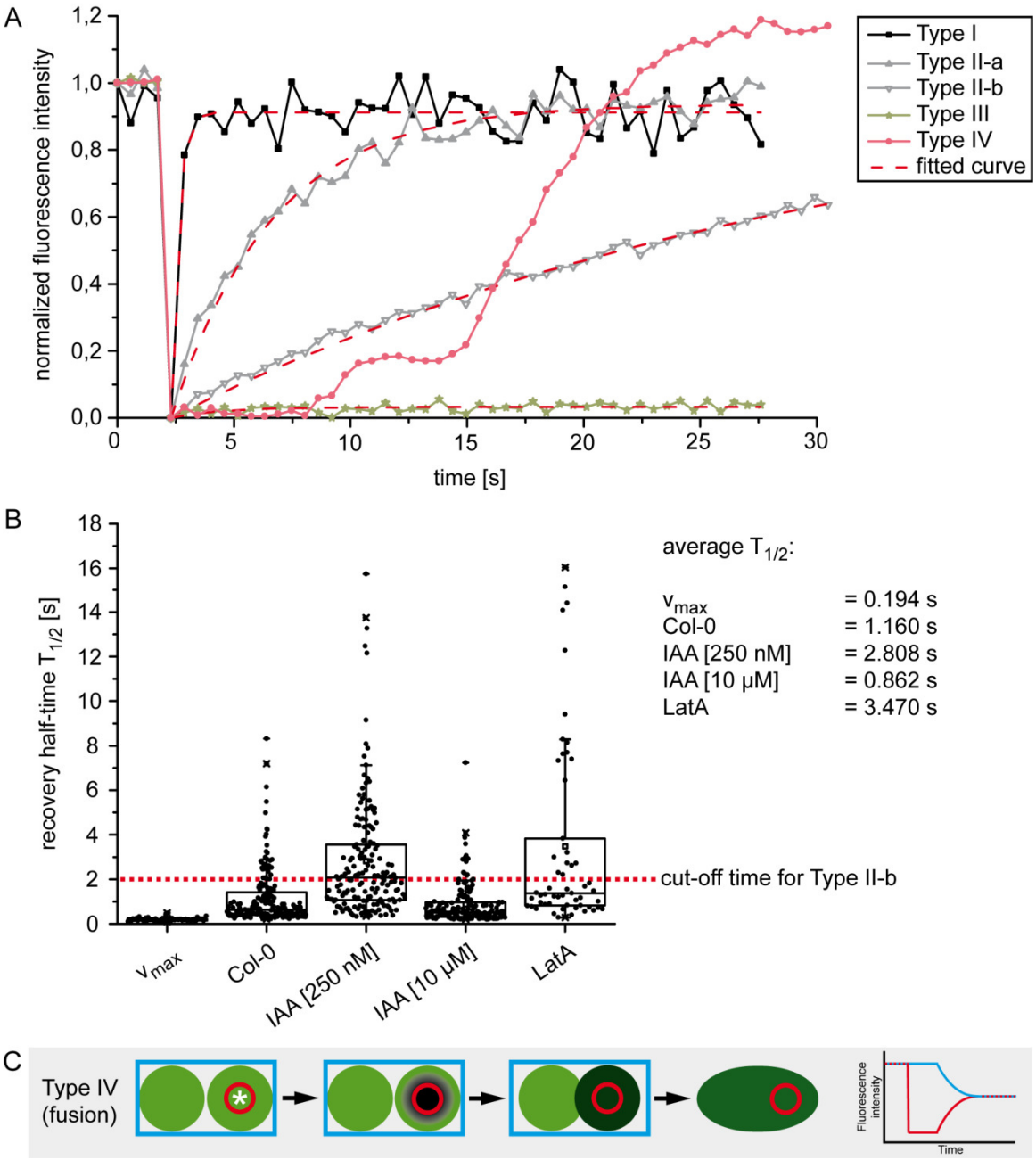

Supplemental Figure 2: Representative measurements and recovery times of vacuole-connectivity FRAP (vaccFRAP) experiments. Normalized fluorescence intensities of vaccFRAP experiments that depict representative measurements according to the established recovery types (A). For each measurement a one-component exponential curve was fitted (indicated by the red dotted lines). Based on the exponential fits the recovery half-time $T_{1/2}$ for all indicated experiments was calculated and summarized in a boxplot (B). The boxplots represent the distribution of n = 63 (v_{max}), n = 222 (Col-0), n = 197 (250 nM IAA), n = 199 (10 µM IAA), and n = 121 (LatA). The red dotted line indicates the cut-off time for Type II-b recoveries and the average recovery half-times are given on the right-hand side. According to the established vaccFRAP recovery types we also developed a schematic representation for vacuole fusion events based on actual measurements (C).

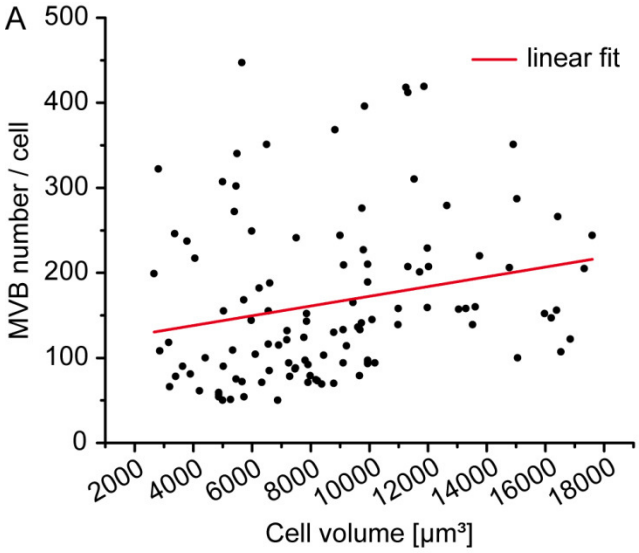

B

model calculation:

i) d_{MVB} = 323.65 nm ± 94.57 nm

ii) $A_{OMVB} = \pi * d^2 = \pi * (0.323\ \mu m)^2 \approx 0.33\ \mu m^2$

iii) $n_{MVB/cell}$ = 164.875 ± 95.35

iv) 1225 µm² / 0.33 µm² = 3712 MVB/LE fusion events

v) $t_{elongation} \approx 6748$ s

vi) 3712 events / 165 MVB/LEs per cell = 22.5 times exchange of MVB/LE population

vii) 6748 s / 22.5 exchanges = 300 s per exchange = MVB/LE lifetime

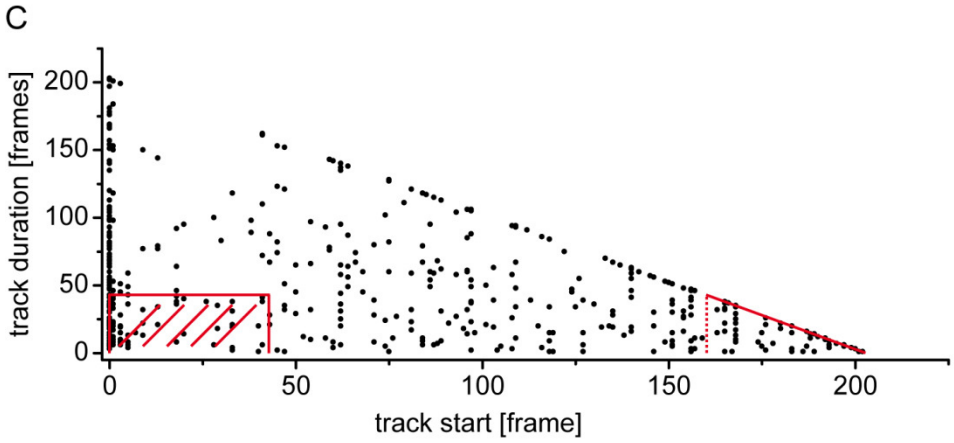

Supplemental Figure 3: Calculation of MVB/LE lifetime in *Arabidopsis thaliana*. 5-days-old seedlings expressing 2xFYVE-GFP were stained with propidium iodide (PI) and Z-stacks of the epidermis and cortex of root tips were acquired using a resonant scanner. The number of MVB/LEs per cell was calculated using the "3D Objects Counter" plug-in for ImageJ (Bolte and Cordelieres, 2006; A). Based on experimental data of cell and vacuole expansion together with the size and number of MVB/LEs we did a model calculation resulting in a maximum MVB/LE lifetime of maximum 300 seconds (B). 3D tracking over time of 2xFYVE-GFP labeled MVB/LEs was analyzed with the "TrackMate" plug-in for ImageJ (Tinevez et al., 2016; C). The continuous red lines indicate the group or single tracked compartments which were excluded from the lifetime calculation. The red dotted line indicates the frame until the compartments which lie on the red line above were excluded. n = 410 tracked compartments were included in the MVB/LE lifetime calculation. A single frame (Z-stack) took 7 s.

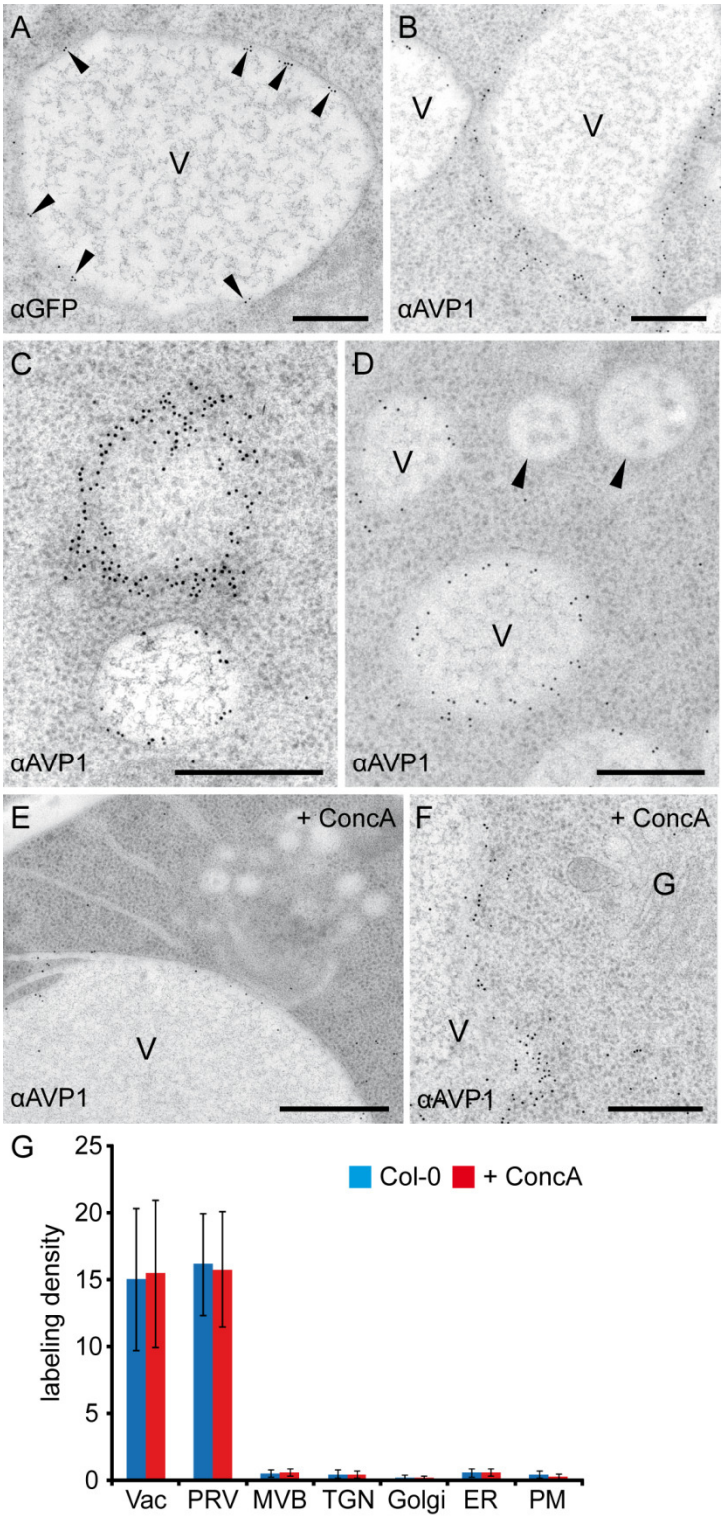

Supplemental Figure 4: Quantification of VHA-a3-GFP and VHP1 immunogold labeling. Ultra-thin sections of high-pressure frozen and freeze-substituted root tips of 5-days-old seedlings were labeled with immunogold. Primary antibodies against GFP in seedlings expressing VHA-a3-GFP or against endogenous pyrophosphatase (AVP1) in Col-0 were analyzed. The immunogold particles showed labeling at the tonoplast for VHA-a3-GFP (A) and VHP1 (B and C). Adjacent MVB/LE were not labeled (arrowheads, D). After 12 h ConcA treatment VHP1 labeling was unchanged (E and F). The labeling density of immunogold particles against AVP1 was quantified in cells incubated with and without ConcA (G) as number of particles per 1 µm membrane stretch. For the indicated compartments, vacuoles (Vac), provacuoles (PRV), MVB, TGN, Golgi, ER, and plastids/mitochondria (P/M) immunogold particles for n = 30 membrane sectors were counted. Error bars indicate the standard deviation. Scale bars indicate 400 nm. EM was performed by Dr. Corrado Viotti.This figure was published in Viotti et al., 2013, but font sizes and colors in (G) were changed.

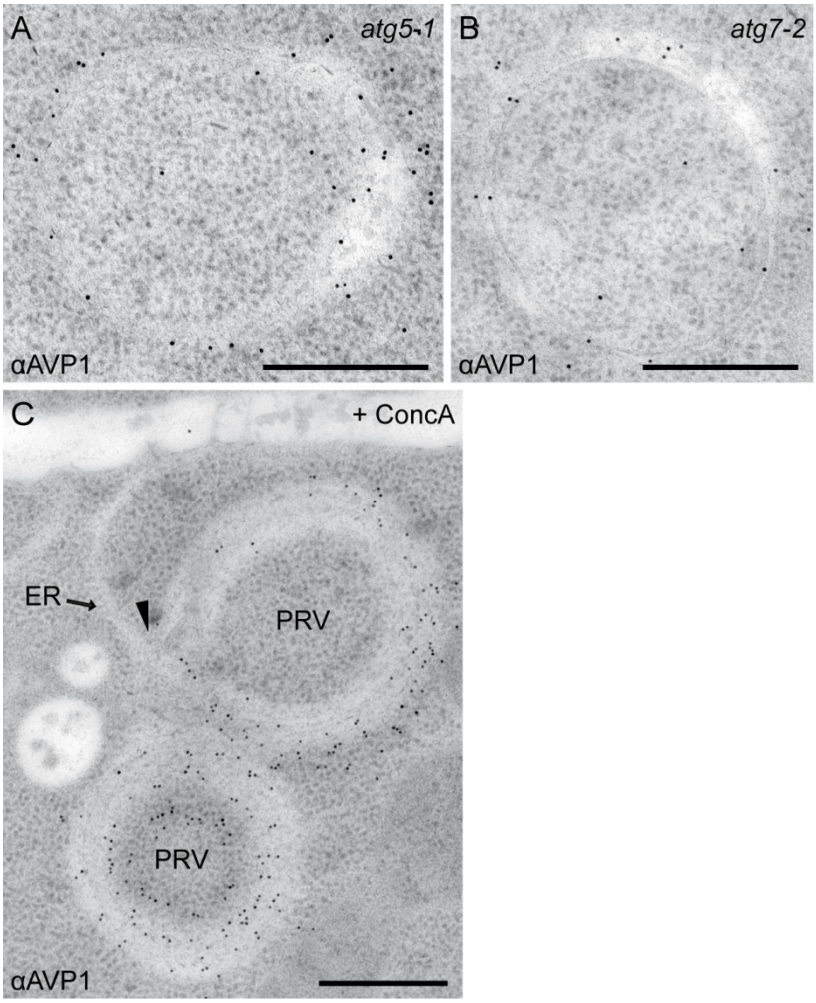

Supplemental Figure 5: Ultra-structure of provacuoles in *atg* mutants and in Col-0 after ConcA treatment. Ultra-thin sections of high-pressure frozen and freeze-substituted root tips of 5-days-old *Arabidopsis thaliana* seedlings were labeled with immunogold. Primary antibodies against endogenous pyrophosphatase (AVP1) in *atg5-1* (A) and *atg7-2* (B) were analyzed. In these mutants autophagosome formation is inhibited but normally shaped provacuoles were detected, labeled by immunogold against AVP1. In (C), the strongly affected, multilayered morphology of provacuoles after 12 h treatment with ConcA is shown. A direct connection between a cortical ER tubule and the provacuole is visible (indicated by arrowhead). PRV = provacuole, ER = Endoplasmic Reticulum. Scale bars indicate 400 nm. EM was performed by Dr. Corrado Viotti. These images were published in Viotti et al., 2013.

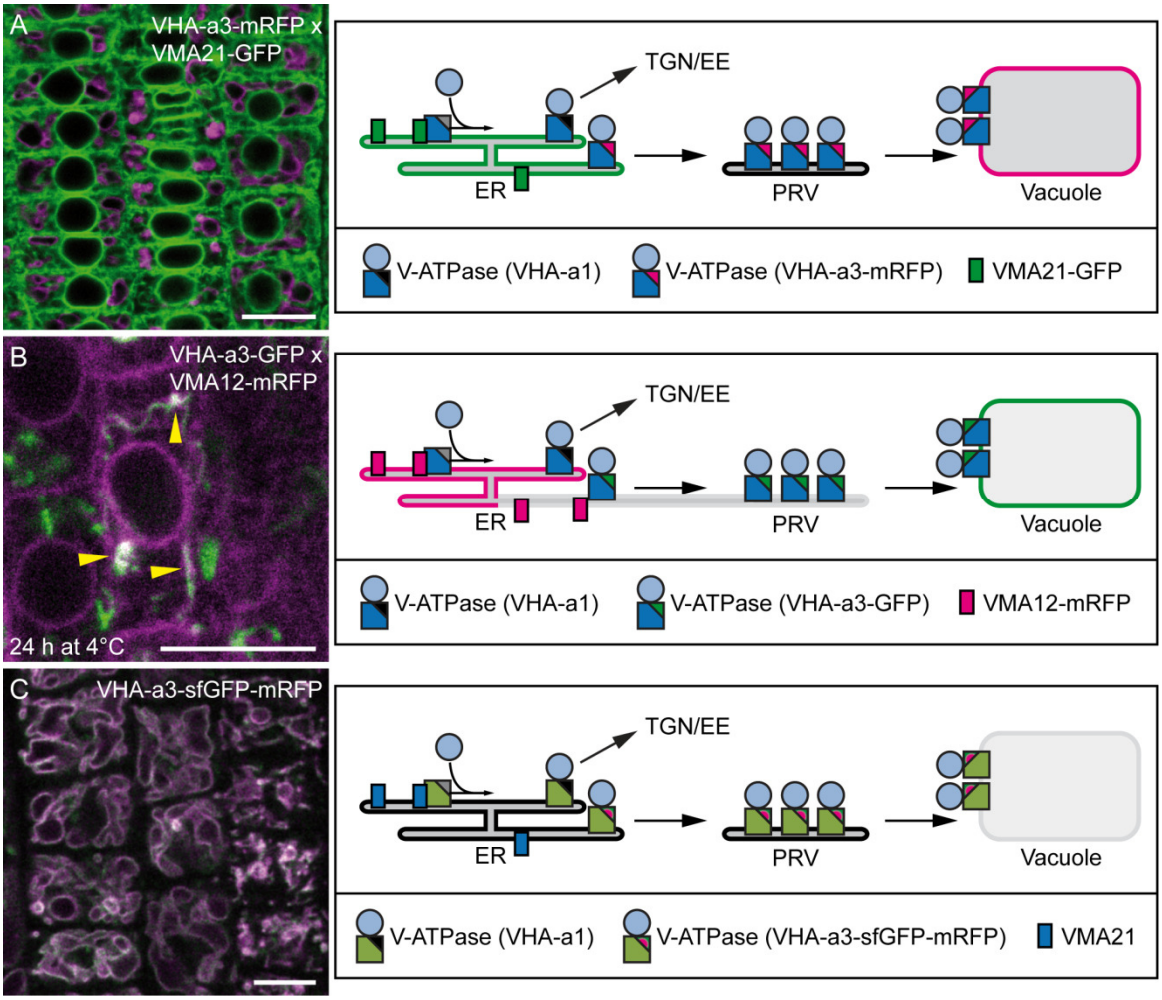

Supplemental Figure 6: Schematic summary of different fluorescent approaches to visualize provacuoles *in vivo*. Here, we combined representative CLSM images with the respective schematic representation of the distribution of the used fluorescent proteins. (A) CLSM image of meristematic root cells of a transgenic *Arabidopsis thaliana* seedling expressing VHA-a3-mRFP and VMA21-GFP. The fluorescent marker proteins labeled the ER (VMA21-GFP) and the tonoplast (VHA-a3-mRFP). In this control situation there is no co-localization that would indicate a putative intermediate compartment. (B) After keeping the seedlings in 1/2 MS agar plates put on ice for 24 h we could see occasional co-localization in tubular structures (arrowheads), but only in provascular cells of root tips. (C) We also expressed VHA-a3 fused to a tandem fluorescent timer of superfolder-GFP and mRFP (sf-GFP; Khmelinskii et al., 2012). We could only detect fluorescence at the tonoplast. Scale bars indicate 10 µm.

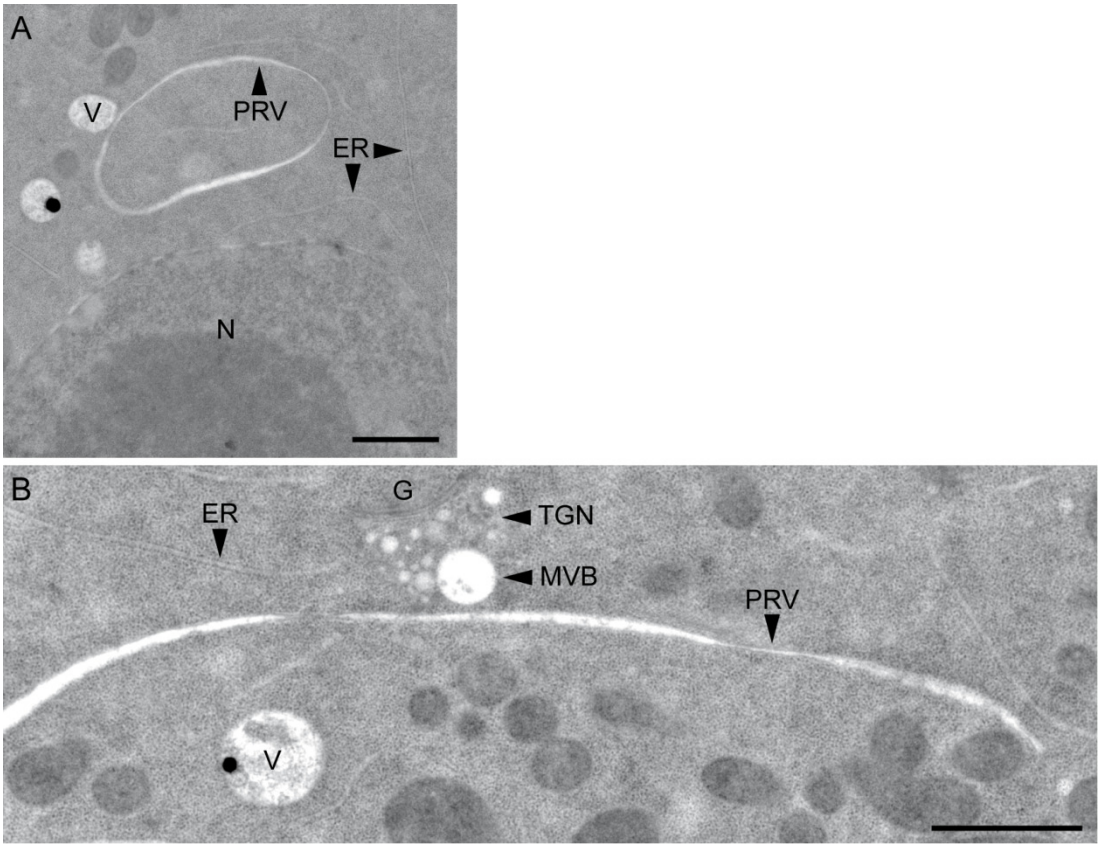

Supplemental Figure 7: Provacuoles can acquire a widespread size. Ultra-thin sections of high-pressure frozen and freeze-substituted root tips of 5-days-old *Arabidopsis thaliana* Col-0 seedlings contrasted with osmium tetroxide. The images showcase examples of provacuoles with an extensive size in a ring-like (A) or long but flat (B) morphology. Sample preparation and imaging together with Dr. Stefan Hillmer. V = vacuole, PRV = provacuole, ER = Endoplasmic Reticulum, N = nucleus, G = golgi apparatus, TGN = TGN/EE, MVB = MVB/LE. Scale bars indicate 1 µm.

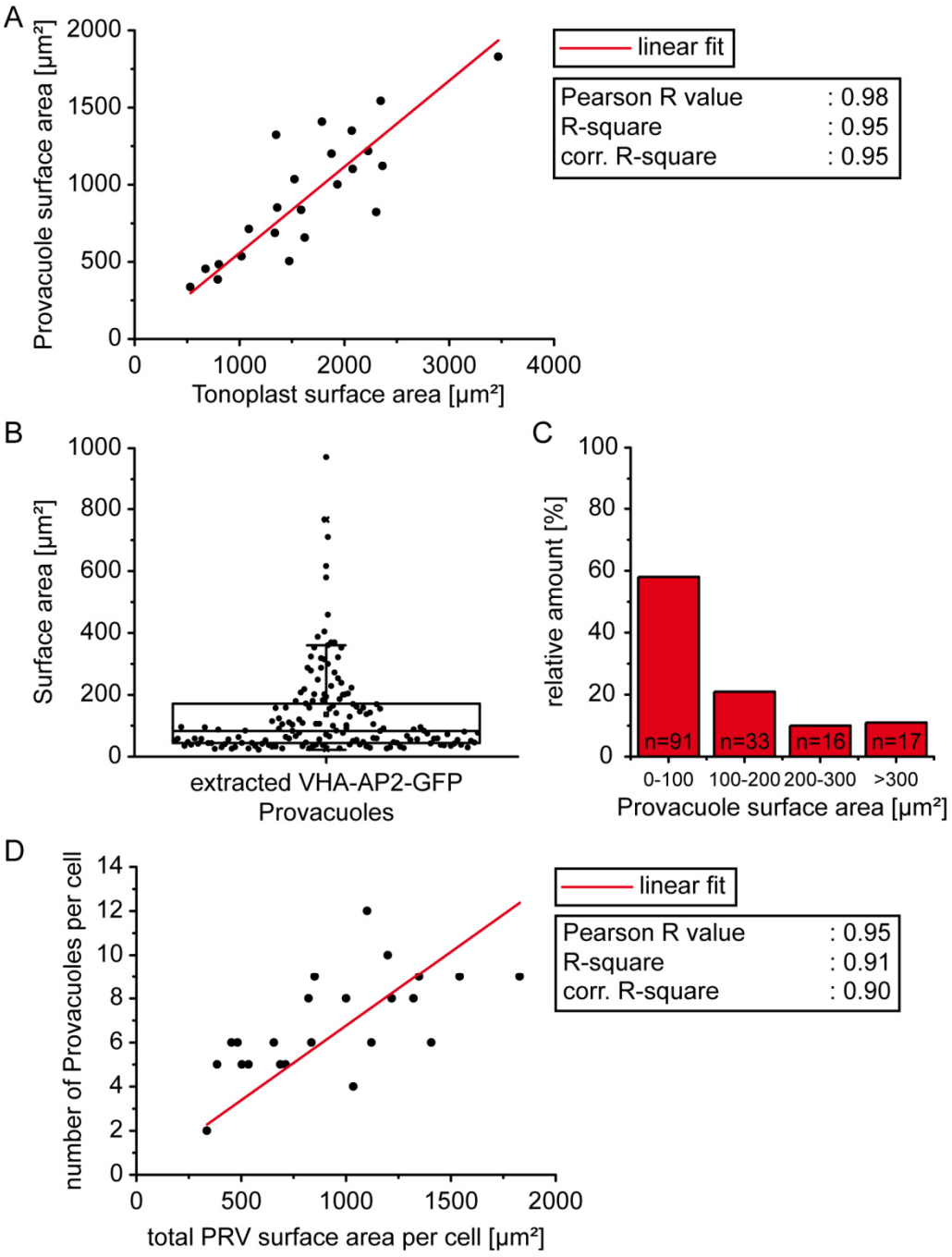

E <u>model calculation with accounted provacuole membrane contribution:</u>

viii) required membrane amount = 490 µm²

ix) 490 µm² / 0.33 µm² = 1484 MVB/LE fusion events

x) 1484 events / 165 MVB/LEs per cell = 9-fold turnover of MVB/LE population

xi) 6748 s / 9 = 750 s per exchange = MVB/LE lifetime

Supplemental Figure 8: Provacuoles provide the majority of new tonoplast material during cell elongation. Correlation analysis of the summed surface area of VHA-AP2-GFP labeled provacuoles with the corresponding tonoplast surface area marked by VHA-a3-mCherry within individual cells after 48 h of DEX induction (A). The surface area of all measured provacuoles labeled by VHA-AP2-GFP is given in (B). The values were sorted into four groups according to size and number (C). Correlation analysis of the number of provacuoles per cell and their corresponding surface area (D). The obtained values were used to update the previous model calculation (Supplemental Figure 3 B) of MVB/LE membrane contribution to tonoplast expansion (E). Red lines in (A) and (D) represent the linear fit correlation curves emanating from the origin of coordinates.

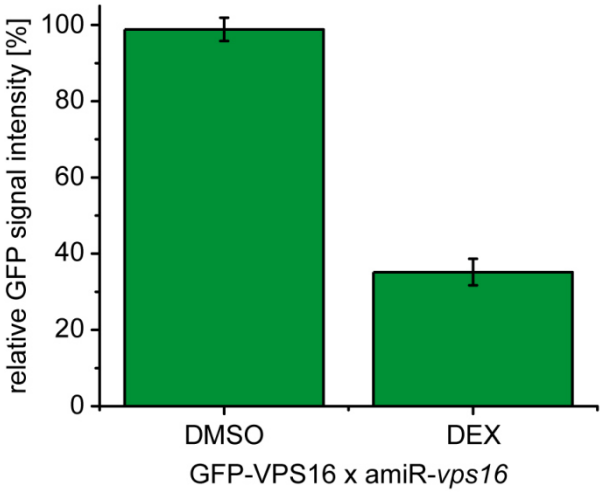

Supplemental Figure 9: Knockdown efficiency of amiR-*vps16* in VPS16 over-expression line. *Arabidopsis thaliana* plants expressing GFP-VPS16 were crossed with plants carrying the DEX-inducible amiR-*vps16* construct. Root tips of 5-days-old seedlings of the homozygous progeny were imaged. After 96 h the same seedlings were imaged again. The fluorescence intensities of both images before and after the treatment was measured for each seedling. The relative GFP signal intensity between both time points is shown in the bar chart. The error bars represent the standard deviation of 3 biological replicates with each n =16 seedlings per treatment.

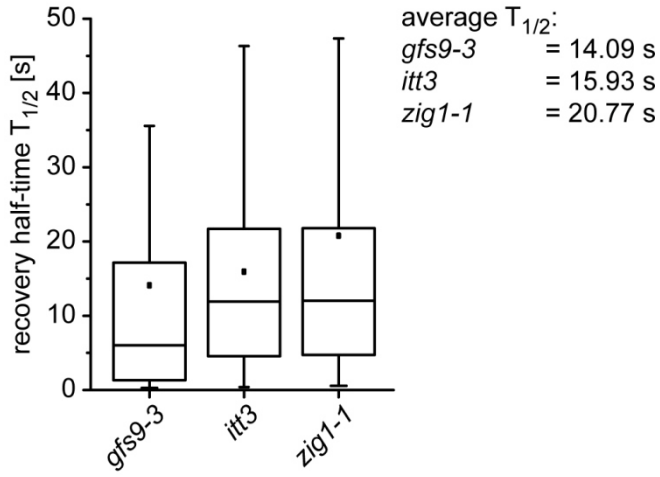

Supplemental Figure 10: vaccFRAP Type II recovery half-times of mutants with strongly affected vacuole morphology. The fluorescence recovery half-times ($T_{1/2}$) were calculated for the indicated genotypes and summarized in a boxplot. The boxplots represent the distribution of n = 20 (*gfs9-3*), n = 113 (*itt3*), and n = 114 (*zig1-1*) measurements. Average $T_{1/2}$ values are given on the right hand side of the figure.

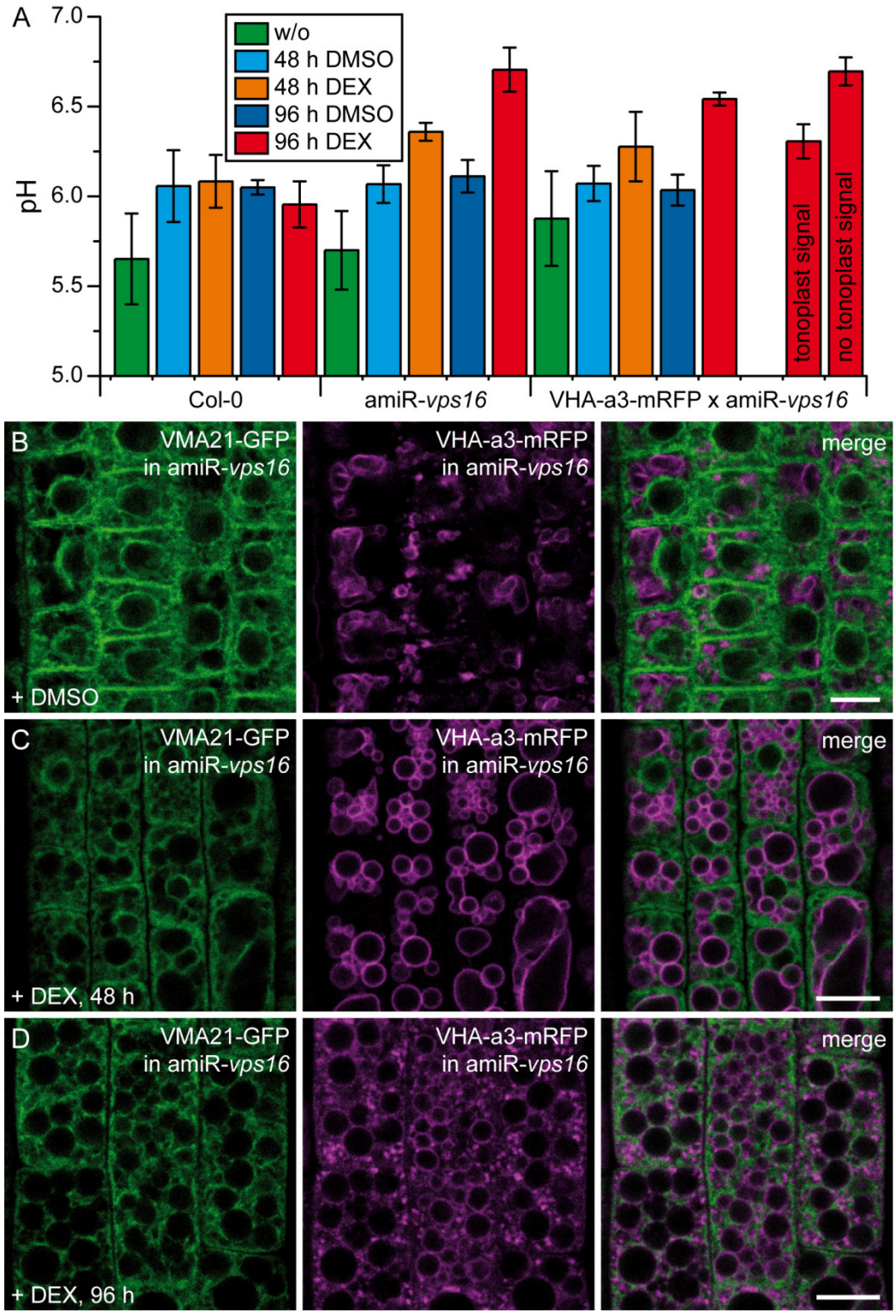

Supplemental Figure 11: pH measurements and localization studies in induced amiR-*vps16* cells. 5-days-old *Arabidopsis thaliana* seedlings of Col-0, amiR-*vps16* and amiR-*vps16* x VHA-a3-mRFP were incubated for the indicated times with either DMSO as control or DEX for inducing agent and stained with BCECF to measure the pH of lytic vacuoles in elongating root cells (A). The 96 h DEX treatment for amiR-*vps16* x VHA-a3-mRFP was manually categorized into cells with and without tonoplast labelling with VHA-a3-mRFP. 5-days-old seedlings of the F2 progeny of a crossing with VHA-a3-mRFP x amiR-*vps16* and VMA21-GFP were incubated with DEX for either 48 h (C) or 96 h (D) and compared to the uninduced conditions (B). Error bars in (A) represent standard deviation of the means of 3 biological replicates with n = 13 - 38 seedlings for each treatment, genotype and condition. Scale bars indicate 10 µm.

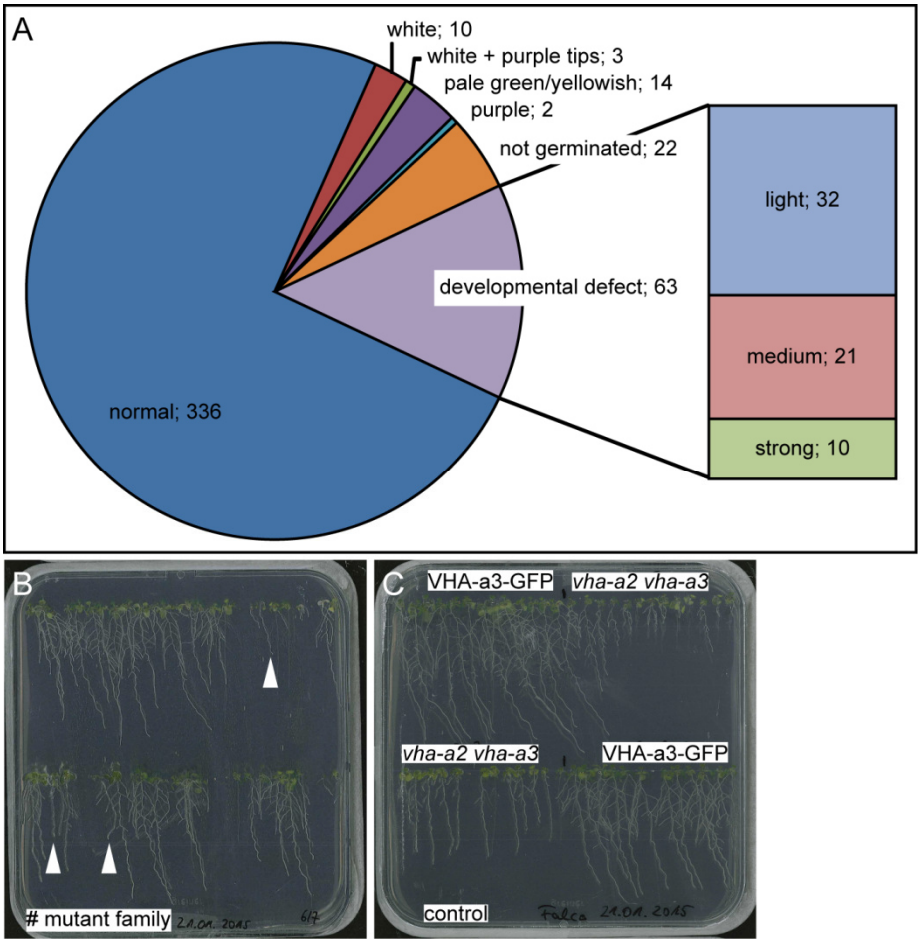

Supplemental Figure 12: EMS mutagenesis evaluation by visible traits and $ZnCl_2$ pre-screen for CLSM analysis. We generated approximately 40000 M1 seeds to screen for VHA-a3-GFP trafficking mutants. The mutagenized M1 seeds were propagated and the M2 seeds pooled in families of about 40 individual plants. We randomly picked 450 M2 seeds from several families and quantified the occurrence of visible traits (A) to verify that we introduced a certain frequency of mutations. The M2 seeds were pre-screened on 1/2 MS plates supplemented with 50 µM $ZnCl_2$ (B). Based on the assumption that trafficking and sorting mutants of V-ATPases destined for the tonoplast would mimic the root growth hypersensitivity of *vha-a2 vha-a3* double knockout mutants on plates with 50 µM $ZnCl_2$, we always used a dedicated control plate in parallel (C). According to the short roots of *vha-a2 vha-a3* mutants we selected seedlings from the M2 pool (examples indicated by arrowheads in B) and analyzed the localization of VHA-a3-GFP in those seedlings.

Discussion

One is all there is - Morphogenesis of lytic vacuoles

Root tips yield an intrinsic developmental gradient thus providing an excellent experimental system to study vacuole morphology. Already at the beginning of the 20th century scientists investigated root tips to study the origin of vacuoles in plants (Bensley, 1910), even more after vital stains, e.g. neutral red, were established (Dangeard, 1923; Guilliermond, 1929, 1941). These works demonstrated that central vacuoles form by fusion of several smaller, round or tube-like vacuoles that were found already in the youngest meristematic cells (reviewed in Zirkle, 1937). The idea of individual vacuoles fusing to become a large single compartment is still widely accepted (Taiz, 1992; Marty, 1999; Seguí-Simarro and Staehelin, 2006). Today, *Arabidopsis thaliana* is an established model organism in plant cell biology, but the early works investigating vacuole development were done in different plant species, preferably those with big colored flower petals, e.g. *Fritillaria imperialis* or *Iris germanica* (Guilliermond, 1941) so that former findings may not apply in general.

In the work at hand, the spatio-temporal development of vacuoles was analyzed by recording Z-stacks of epidermal root tip cells in order to reconstruct the contained vacuolar volume. Here, we found that developing vacuoles in Arabidopsis form a single interconnected compartment of predominantly tubular shape. Though single optical sections of a stained vacuole can appear to be separated into several independent round, rod-like or tubular domains, the means of 3D reconstructions allowed us to capture their entirety within cells. Over time, this vacuolar lumen inflates as the cells elongate and eventually becomes the typical central vacuole (Figure 5), showing an intriguing similarity to drawings depicting vacuole formation of cresyl blue stained *Hordeum* root meristems and young rose leaf cells (Guilliermond, 1929).

While maximum-projected Z-stacks improve single 2D images in terms of representative volume information, surface rendering excels projected volumes by not only creating the impression of a vacuole volume (Krüger et al., 2013) but generating an actual 3D computer model that can be observed from any angle. This approach provided evidence that the tubular vacuoles are indeed interconnected within a single cell and even during cytokinesis (Figure 4 E). Furthermore, since the spatial dimension of each recorded pixel from the specimen is maintained the actual dimensions could be calculated. This enabled us to determine the ratio of vacuolar surface area to vacuolar volume thereby establishing a measurable feature of morphological vacuole complexity (Figure 5 D). The

higher the amount of tubules in a vacuole network, i.e. its complexity, the bigger its surface area is in relation to the volume contained and vice versa. Accordingly, this ratio decreased along with the development of tubular vacuolar networks found in meristematic cells into the rectangular cuboid-like shape in differentiated cells.

3D surface renderings similar to our approach (Viotti et al., 2013) allowed other scientists to demonstrate that vacuoles in closed guard cells are strongly constricted but still preserve a connected configuration (Andrés et al., 2014). The same holds true for changes in vacuole morphology induced by prolonged auxin treatment (Scheuring et al., 2016). Moreover, rendering and calculation of the surface area to volume ratio as an indicator of vacuole morphology underlined the severe defects on vacuole biogenesis in the MVB maturation mutants *fyve1* and *alix* (Kolb et al., 2015; Kalinowska et al., 2015).

Quantification of morphological differences of vacuoles

Rendered models of vacuoles display these compartments as static bodies. However, this turned out to be misleading as their highly dynamic nature was revealed in 3D time lapse imaging using the functional GFP-tagged VHP1 fusion protein (Segami et al., 2014). Though developing vacuoles form a single tubular compartment, they constantly revolve within the cell comparable to cytoplasmic streaming, establishing new tubular extensions and join up with other parts of the vacuolar system. Comparable observations were made in epidermal cells of red onion (Wiltshire and Collings, 2009). In the context of a living cell the acquisition speed of Z-stacks is as crucial as the spatial resolution due to the default movement. However, image acquisition adjustments by decreasing either the voxel size or the pinhole diameter did not enable us to reliably record 3D time-lapse series of BCECF-stained vacuoles with a quality level sufficient for surface rendering. In contrast, we established vaccFRAP, a method that only requires 2D time lapse imaging to assess the spatial connectivity status of vacuoles thereby avoiding excessive energy input to the specimen (Figure 7 C). The method is limited by the loading efficiency of BCECF and the smallest adjustable bleach-point diameter of the microscope. Based on our vaccFRAP measurements individual vacuoles were classified to be either isolated (Type III), fully connected (Type I) or linked via tubules that restrict free diffusion of bleached and unbleached BCECF molecules (Type II). Our results showed that 95% of all measured wild-type vacuoles were connected compartments, supporting our findings of the 3D reconstructions that vacuoles are coherent compartments. In addition, recovery half-times were calculated from the recorded fluorescence intensity curves of Type II vacuoles so that we could distinguish between interconnected vacuolar networks of different genotypes and treatments. By adding different concentrations of auxin we

manipulated the tubular vacuole morphology in elongating cells, creating either more constricted or more inflated compartments. Accordingly, based on our experimental data two subgroups of fast recovering vacuoles (Type II-a), representing wild-type morphology, and slowly recovering vacuoles (Type II-b) were created.

vaccFRAP differs from conventional FRAP experiments in that the fluorescence recovery of an optical plane is recorded that belongs to a 3D volume rather than a 2D membrane sheet. Due to the diffusion of bleached and unbleached BCECF molecules within the vacuolar lumen, the 2D cross section reflects the connectivity status of the entire volume. In contrast to FRAP experiments that bleach membrane integral proteins, fluorescence recovery is only prevented if a volume is truly isolated. Vacuoles of the VTI11 mutant *itt3* (Zheng et al., 2014b) were shown to be isolated compartments based on the lateral diffusion of the tonoplast intrinsic fusion protein GFP-TIP2;1 (Zheng et al., 2014a). Here, we found that almost 75% of the measured vacuoles in *itt3* are still connected compartments. Even though we analyzed vacuoles of the elongation zone rather than fully differentiated cells as Zheng and colleagues, it is unlikely that their connectivity status changes in between since the overall appearance does not. Instead, partial complementation of lacking VTI11 SNAREs by VTI12 (Sanmartín et al., 2007) might possibly lead to an arrested dissociation of membrane fusion factors. In yeast it was demonstrated that HOPS membrane tethering complexes execute SNARE proofreading function thus mediating membrane fusion progression (Starai et al., 2008; reviewed in Balderhaar and Ungermann, 2013). Assuming that VTI12 can promote vacuole membrane fusion in Arabidopsis, the vacuolar volume could be already connected via a small membrane fusion pore. This is supported by our measurements showing that the fluorescence recovery of *itt3* Type II vacuoles is extraordinarily slow (Supplemental Figure 10). At the same time HOPS proof-reading of atypical SNARE-complexes containing VTI12 could cause a delayed dissociation of the fusion machinery and thereby lead to impaired lateral movement of membrane integral proteins. During initial membrane tethering of vacuoles in yeast, a vertex ring forms. It is generated by activated Rab7-GTPases and excludes unnecessary proteins from the future fusion site, lipid mixing of the outer membrane leaflets and lateral movement of proteins (Wickner, 2010). Once HOPS mediated fusion occurred, all factors dissociate. Since most vacuole membrane fusion factors are conserved in Arabidopsis (Uemura and Ueda, 2014; Vukašinović and Žárský, 2016), probably also hallmark stages of this process are similar. This model would explain the different results from *itt3* vacuoles obtained by the FRAP experiments based on lateral protein diffusion within the tonoplast versus the volume-based vaccFRAP method described here. Moreover, this scenario is supported by the

observation that WM can induce re-fusion of *itt3* vacuoles (Zheng et al., 2014b, 2014a). As mentioned in the introduction, membrane association of activated Rab-GTPases and HOPS complexes depend on PI3P. WM, as inhibitor of the PI3-kinase, was shown to cause rapid dissociation of the genetically encoded fluorescent biosensor 2xFYVE in Arabidopsis (Vermeer et al., 2006; Takáč et al., 2013; Zheng et al., 2014b), indicating that WM releases proteins that bind to membranes via PI3P association. Following this idea, WM treatment supposedly unblocks the fusion factor dissociation by releasing them into the cytosol thereby fully opening the fusion pore.

In conclusion, recovery half-time values of vaccFRAP experiments can be used as a measure of vacuole network connectivity that in turn provides quantitative information of the 3D morphology of vacuoles beyond the mere differentiation between connected or isolated compartments. Due to its rather easy experimental procedure and since it only requires BCECF staining of vacuoles, vaccFRAP can be performed in any other mutant or treatment to detect even minor and less obvious differences in vacuolar architecture than those induced by auxin.

Membrane tethering complexes are essential for vacuole morphogenesis

To deliver their cargo to the vacuole, the numerous vesicles derived from endosomal trafficking routes have to fuse with the tonoplast. Taking into account the default motion and enomous plasticity of developing vacuoles, it is reasonable to assume that their morphological development requires constant membrane fusion, too. Endosomal membrane fusion with the vacuole membrane was shown to be mediated by Rab-GTPases, SNAREs and membrane tethering complexes in mammals and yeast (Wickner, 2010). In yeast, HOPS is necessary for late endosomal fusion with the vacuole and homotypic vacuole fusion (reviewed in Balderhaar and Ungermann, 2013). But in contrast to yeast, all homozygous T-DNA knockout lines of HOPS subunits in *Arabidopsis* are not viable (Rojo et al., 2001; Niihama et al., 2009; Hao et al., 2016). This indicates the importance of both, membrane fusion mediated by these complexes and vital presence of lytic vacuoles. To study the function of membrane fusion components, weak mutant alleles (Hao et al., 2016; Feng et al., 2017a) or inducibly expressed dominant negative proteins (Cui et al., 2014; Feng et al., 2017a) were successfully used in the past to avoid putatively embryo lethal phenotypes of knockout mutants, e.g. *vcl1* (Rojo et al., 2001). Here, we studied the role of the CORVET/HOPS membrane tethering complexes by inducibly expressing an artificial micro RNA against VPS16 (Figure 19). In induced root tips, vacuoles failed to establish a connected morphology, suggesting that

vacuole development strongly depends on CORVET/HOPS mediated membrane fusion processes. The usually tubular vacuoles displayed a highly fragmented, sphere-like phenotype distinctly more severe than reported before in pollen tubes (Hao et al., 2016; Feng et al., 2017a). By using vaccFRAP we could determine that all observed vacuoles in elongating cells were indeed isolated compartments, demonstrating the effectiveness of our induction system. However, the level of GFP-tagged VPS16 was only reduced by two thirds. Still, this amount seems to be below a critical threshold of VPS16 subunits to assemble enough functional CORVET/HOPS complexes necessary for vacuole development. Previous experiments in our lab demonstrated severe growth defects in root and hypocotyl elongation as well as whole plant development upon amiR-*vps16* induction (Master thesis by Jana Askani, 2015). As pointed out before, a deliberately shaped tubular network of vacuoles might be beneficial to accommodate the newly forming cell plate during cell division (Seguí-Simarro and Staehelin, 2006; Figure 4) and at the same time maintain the integrity of the lytic compartment. A connected conformation ensures that all tonoplast localized transporters, channels, pumps etc. remain equally distributed within the cell at any time. This becomes especially important the more transport routes with specific cargo end in the vacuole. Since at least two SNARE proteins are delivered independently to the tonoplast (Ebine et al., 2014; Uemura and Ueda, 2014), assuming there are only separated vacuoles would inevitably lead to an unequal membrane fusion factor equipment of tonoplast membranes and hence inefficient cargo delivery. Given that their density in the tonoplast is constant, another advantage of a single compartment would be that vacuoles with a high surface area to volume ratio would allocate more proton pumps per volume. As a consequence, vacuoles in the root tip should have a higher potential to accumulate solutes as well as buffer pH changes and toxic ion concentrations in the soil.

Temporary down-regulation of CORVET/HOPS subunits was shown to lead to fragmentation and significant volume reduction of lytic vacuoles in *Medicago* as prerequisite for simultaneously emerging symbiosomes (Gavrin et al., 2014). Similarly, the calculated surface area of 3D rendered vacuoles revealed that compared to wild type cells only their contained volume changed markedly upon amiR-*vps16* induction (Figure 20). This was not the case for the generated membrane surface meaning that tonoplast synthesis itself remained constant although the overall vacuole morphology was highly affected. Our results thus may also suggest that tonoplast synthesis, vacuole morphogenesis and vacuole degradation are mechanistically separate processes. Since the DEX-inducible amiR-*vps16* knockdown system targets a shared structural subunit of CORVET and HOPS, future research needs to address the question which of the two

complexes specifically mediate vacuole development and trafficking. Preliminary results in our lab suggest a HOPS-specific role in morphogenesis, however since also Rab5-GTPase exclusive trafficking routes end at the tonoplast (Ebine et al., 2014), an additional bi-functional CORVET/HOPS complex is conceivable.

We observed that the phenotype of fragmented vacuoles directly corresponded with the duration of amiR-*vps16* induction. Interestingly, anterior parts of the root that contained fully differentiated cells at the start of induction did not or only partly show vacuole fragmentation. We speculate that this is due to the significantly reduced complexity of the vacuole volume in these cells. Since fully developed vacuoles display a rectangular cuboid-like shape it is unlikely that a subvolume is separated by its own revolving movement. A reasonable explanation for the occurrence of fragmented vacuoles might be the formation of trans-vacuolar strands (TVS). TVSs are considered as highly dynamic cytoplasmic passages through the fully inflated vacuole more than tonoplast material reservoirs (Ruthardt et al., 2005; Segami et al., 2014). Their formation, number and stability is highly dependent on intact actin filaments (Uemura et al., 2002; Higaki et al., 2006; Sheahan et al., 2007) and the recently discovered protein of unknown function REGULATOR OF BULB BIOGENESIS 1 (RBB1; Han et al., 2015). The current model of TVS development proposes the formation of a tonoplast invagination by a constricting actin filament bundle running along the tonoplast. Eventually, the rims of the so called tonoplast groove would fuse and release a cytoplasmic tunnel into the vacuolar lumen (Higaki et al., 2006). It is likely that this homotypic tonoplast fusion event might be impaired upon VPS16 knockdown. As a consequence, a progressing actin bundle constriction or its lateral movement could actively divide a vacuole thus creating an isolated subvolume. In this case the final scission has to be considered as a membrane fission event. Depending on how frequently TVS would be formed in specific cell types, the number of fragmented vacuoles may differ. This could also explain less drastic morphological changes in fully differentiated leave tissues.

Vacuole morphology depends on multiple factors

The fact that there is usually one vacuole per cell contradicts the general idea that central vacuoles develop from several smaller vacuoles by fusion but simplifies the model of how a vacuole forms. Given that enough membrane material is provided a vacuole would "only" have to inflate like a balloon. A measurable feature of this development is the ratio of vacuole surface area and vacuole volume, reflecting the spatial complexity of the compartment (Viotti et al., 2013). Recent findings suggest that auxin can affect vacuole morphogenesis by changing the abundance of tonoplast

localized SNAREs (Löfke et al., 2015). Also, mutants or chemical treatments that alter the lipid identity of the tonoplast, SAC phosphoinositide phosphatases overexpressors, *pi4kß1/2* and the PI3K/PI4K inhibitor WM, induced less tubular vacuoles in meristematic cells (Nováková et al., 2014; Löfke et al., 2015). Moreover, actin filaments were shown to be closely attached to the tonoplast and their chemical disruption induced fragmented vacuoles (Scheuring et al., 2016; Figure 7). It was further proposed that auxin induced vacuolar constriction is the result of condensed actin filaments and myosin motor proteins rather than microtubules. Even though the connecting link between the tonoplast and the actin cytoskeleton is not known yet, it seems plausible that it plays an important role in actively shaping tubular vacuoles, maybe even for the default vacuole movement. Future experiments should investigate the distribution of cytoskeleton elements in induced amiR-*vps16* cells to decipher which factor is responsible for the spherical vacuolar shape. Preliminary results indicate that even though the rounded vacuoles resemble the phenotype of LatA-induced actin depolymerization, the filaments were still tightly wrapped around the vacuoles. This suggests that actin filaments rather follow than dictate the shape of vacuoles and there might be a link between membrane tethering complexes and the cytoskeleton. NET4 could establish such a link as it was shown that it is localized at the tonoplast in a specific pattern mimicking the filamentous organization of actin filaments. It contains a plant specific domain to bind to actin as well as a domain to associate to membranes (Deeks et al., 2012). However, additional mechanistic details are missing so far. Interestingly, *in vitro* expriments showed that VHA-B subunits of the V-ATPase can bind to actin filaments and thus might also be involved in cytoskeleton remodeling (Ma et al., 2012).

Vacuole shape determination seems to be the result of a balanced system of lipid modifications, membrane fusion factors and cytoskeleton elements. However, there might be more proteins that play yet undiscovered roles in modulating vacuole shape. Scientists recently created artificial tubular web-like membranes similar to the ER by mixing liposomes with a membrane fusion protein and a membrane curvature stabilizing factor from yeast. It was found that when constant membrane fusion was blocked, the self-organized tubules immediately fragmented, suggesting that compartment morphology might be the product of steady formation and disassembly (Powers et al., 2017). The same study further demonstrated that the GTPase atlastin, on its own, was able to form tubular membranes out of liposomes. In plants, the interaction of atlastin and the reticulon HVA22 was previously shown to modulate ER morphology when over-expressed in tobacco leaf epidermal cells (Lee et al., 2013). It might be that similar to the restricted expression of actin binding NET4 (Deeks et al., 2012) curvature stabilizing

proteins are expressed in the root meristem to specifically support the formation of tubular vacuoles, possibly related to proteins shaping the ER (Sparkes et al., 2011). In addition, early studies suggested that the shape of vacuoles changes in response to the activity of cytoplasmic streaming (Bailey, 1930; Zirkle, 1932). It would thus be interesting to analyze if there is an altered morphology or impaired movement of vacuoles in myosin mutants and plants expressing chimeric myosin proteins that exhibit reduced cytoplasmic streaming (Tominaga et al., 2013). These mutants have a strong cell elongation and growth phenotype that might also be linked to delayed vacuole development.

Revising the classic model of tonoplast membrane contribution

During cell elongation in the root tip the contained tubular vacuoles expand drastically, ultimately developing into a central vacuoles. This requires a steady delivery of substantial amounts of newly synthesized tonoplast material, yet the membrane donor compartment of vacuole biogenesis is still unknown. There are two major models that propose different origins for the vacuolar membrane. The first one suggests smooth-ER derived tonoplast precursors, i.e. provacuoles, fusing to form flat membrane sheets to enclose organelle free cytoplasm. Subsequently, the lumina of these structures inflate and by digesting the trapped cytoplasmic content, small vacuoles are created which then fuse to form bigger compartments (Matile and Moor, 1968; Mesquita, 1969; Amelunxen and Heinze, 1984; Hilling and Amelunxen, 1985). The second model suggests TGN/EE derived tubular structures that enlarge by fusion and form ring-like autophagic vacuoles, also digesting enclosed cytoplasm (Marty, 1978). A causal link was reasoned due to the detection of enzymatic activity of acid hydrolases in both, the TGN/EE (originally termed GERL) as the origin compartment and the vacuole as the destination. In favor of this model there are numerous findings that demonstrate the transport of soluble cargo, membrane integral transporters and channels as well as degradation of plasma membrane localized receptors through the late endosomal route (recently reviewed in Uemura and Ueda, 2014; Viotti, 2014; Paez Valencia et al., 2016). In contrast, our quantification of late endosomal traffic towards the vacuole revealed two interesting results. First, we found that the total number of MVB/LE compartments per cell in the root elongation zone seems to be nearly constant on average, regardless of the cell size (Supplemental Figure 3). On the one hand this finding suggests that the cytoplasmic volume does not increase in sync with the cell volume as the overall number of contained compartments remains stable. On the other hand, it supports the idea that the vacuole is the low-cost way to rapidly fill expanding cell volume.

Second and most importantly, we found that the amount of membrane surface area provided by MVB/LEs is not sufficient to be the only membrane donor of expanding vacuoles (Figure 8). With an average lifetime of about 8 minutes only 60 % of the vacuole surface area increase could be covered during the initial cell elongation. Moreover, this is probably over-estimating the actual membrane contribution considering that the marker protein we used to track individual late endosomes, 2xFYVE-GFP (Vermeer et al., 2006), is predominantly labeling late stages of MVB maturation (Singh et al., 2014). In comparison, the average lifetime of late endosomes in human cells was measured between 10 to 15 minutes (Futter et al., 1996; Rink et al., 2005). Since there are other trafficking routes reported to end at the vacuole the origin of tonoplast material should be considered as the sum of all incoming trafficking.

Trafficking of vacuolar proton pumps reveals a novel transport route to lytic vacuoles

The majority of transport processes across the tonoplast uses energy which is provided by an electrochemical gradient between the vacuolar lumen and the cytoplasm (Martinoia et al., 2012). It is generated by an interplay of proton pumps and other ion transporters that balance the electric charges (Schumacher, 2014). The V-ATPase and the V-PPase are two of the most abundant proteins at the tonoplast (Carter et al., 2004). Still, their intracellular trafficking route is not known even though there are many studies investigating the localization and function of these proton pumps with either peptide antibodies (Herman et al., 1994; Ratajczak et al., 1999; Dettmer et al., 2006) or fluorescent fusion proteins (Dettmer et al., 2006; Krebs et al., 2010; Segami et al., 2014). Since subcellular transport processes mostly occur via vesicles rather than stable physical connections between compartments, we hypothesized that protein traffic towards the vacuole inevitably should coincide with membrane flux. This led us to follow the trafficking route of both, V-ATPases and V-PPases. We found that both proton pumps are transported from the ER to the vacuole in a so far unknown, more direct way to the vacuole while bypassing Golgi and post-Golgi compartments (Viotti et al., 2013).

Tonoplast integral proteins are co-translationally inserted into the ER membrane whereas soluble vacuolar cargo molecules are synthesized within the ER lumen and bind to dedicated vacuolar sorting receptors (Niemes et al., 2010; Künzl et al., 2016). Both kinds of proteins are then transported to the Golgi via COPII vesicles and afterwards reach the TGN/EE, the compartment where endocytic and secretory trafficking converge (Dettmer et al., 2006; Viotti et al., 2010). From there, vacuolar cargo is sorted into emerging multivesicular bodies that pinch off and proceed towards the

vacuole (Scheuring et al., 2011). Once released, MVB/LEs undergo an intricate maturation process (i) to form intra-luminal vesicles into which ubiquitinated membrane proteins destined for degradation are sorted (reviewed in Cui et al., 2016) and (ii) to obtain a specific membrane identity to allow membrane fusion with the tonoplast (Singh et al., 2014; Ebine et al., 2014; Cui et al., 2014). As previously shown, incubation with ConcA inhibits MVB/LE maturation at the TGN/EE thus blocking endocytic and soluble cargo transport towards the vacuole (Scheuring et al., 2011).

In addition to this classical transport route there exist alternative pathways delivering tonoplast proteins to the vacuole. The sucrose transporter SUC4 was shown to require AP3 complexes for their transport which is blocked in the corresponding *pat2-1* mutant (Feraru et al., 2010; Wolfenstetter et al., 2012). In contrast, INT1, a tonoplast localized myo-inositol transporter, is still delivered in this mutant background (Wolfenstetter et al., 2012), but its transport is blocked upon ConcA treatment (Viotti et al., 2013). In the present study we found that neither ConcA treatment nor the lack of the AP3 β-subunit in *pat2-1* can prevent the delivery of V-ATPases and V-PPases to the tonoplast, suggesting a transport route that bypasses post-Golgi compartments.

The subcellular localization of V-ATPases is determined by which of the three VHA-a isoform subunits is incorporated into the holo complex (Dettmer et al., 2006). After assembly at the ER, VHA-a1 containing V-ATPases destined for the TGN/EE are exported in a COPII-dependent manner as previously demonstrated (Richter et al., 2007). In cells of *gnl1*;GNL1 BFA-sens. mutants COP-mediated transport between the ER and Golgi collapses upon BFA-treatment. Our experiments using CLSM and IEM in this genetic background showed that the delivery of V-ATPases and V-PPases to the tonoplast was not impaired. This implies different sorting of V-ATPases containing VHA-a1 and VHA-a3 already at the level of the ER. For the yeast V-ATPase subunit Stv1p a specific three amino acid sequence was identified to be responsible for targeting to the Golgi (Finnigan et al., 2012) which is absent in Arabidopsis. A recent PhD thesis in our laboratory revealed that VHA-a1 contains an acidic cluster with a critical leucine (L159) residue in its N-terminus serving as an ER export signal as well as a TGN/EE retention motif (Lupanga, 2017). Though it was possible to re-route VHA-a1 containing V-ATPases to the tonoplast, the specific signal to enter the provacuole transport route is not known yet.

To rule out that VHA-a3-mRFP recovery at the tonoplast results from different maturation speeds of the fluorophores fused to either VHA-a1 and VHA-a3, we performed FRAP experiments to record only newly synthesized proteins upon BFA block in *gnl1*;GNL1

BFA-sens. mutants. Similar to the results before, VHA-a1-GFP was retained in the ER whereas VHA-a3-mRFP still reached the tonoplast (Figure 10). These findings pointed to a new trafficking route that completely bypasses COPII-mediated ER-export as well as Golgi and post-Golgi compartments. Interestingly, unlike Arabidopsis VHA-a3, mammalian VHA-a subunits were shown to transit through the Golgi thereby receiving a N-glycosylation modification that is, at least for VHA-a4, important for their stability and transport to subcellular destinations (Kartner et al., 2013; Esmail et al., 2016). Previous studies in tobacco demonstrated that there might be multiple, in part BFA-insensitive transport routes of TIP proteins to lytic and protein storage vacuoles (Gomez and Chrispeels, 1993; Bottanelli et al., 2011; reviewed in Pedrazzini et al., 2013). In Arabidopsis, another exception to the classic vacuole transport pathway was shown by means of chemical genetics. Incubation with the inhibitor C834 led to ER-retention of the BFA-insensitive delivery of TIP1;1 and TIP3;1 (Rivera-Serrano et al., 2012). It is at question if the artificial over-expression of the PSV-specific TIP3;1 might interfere with correct ER-export in cells that usually do not express PSV proteins anymore (Hunter et al., 2007). Still, the target and mechanism of C834 are unknown and it will be interesting to find out whether C834 can also block ER export of V-ATPases destined for the tonoplast.

Provacuoles are early stages of vacuole biogenesis

So far we provided evidence that strongly implies a direct ER-to-vacuole transport route of V-ATPases and V-PPases to the tonoplast. In several different plant species, storage proteins were shown to be transported directly from the ER to PSVs during seed maturation by specialized structures called protein bodies or precursor accumulating (PAC) and PAC-like vesicles (Hara-Nishimura, 1998; reviewed in Herman, 2008 and De Marchis et al., 2013). In Arabidopsis, a comparable trafficking pathway to lytic vacuoles was only demonstrated for autophagy-related degradation (Le Bars et al., 2014). By performing IEM with antibodies either specifically against V-PPase (Kobae et al., 2006a) or against GFP in plants expressing VHA-a3-GFP we identified double-membrane structures with minimal luminal expansion but a high density of the two vacuolar proton pumps. They formed circular structures, seemingly enclosing cytoplasm, or arch-like areas partly with already more enlarged areas, comparable to the light grey texture typically found in lytic vacuoles (Hillmer et al., 2012). We further co-stained seedlings expressing VHA-a3-GFP with SNARF-1 and observed similar membrane loops already in contact with the tonoplast. Moreover, these structures inflated and were filled over time, suggesting that they are early stages of vacuole biogenesis capable of expanding. According to the definition of a vacuole precursor, we termed them provacuoles.

During phagophore formation semi-circular or circular structures are formed that enclose portions of the cytosol, thus sharing a high similarity to the provacuole structures we observed in our studies (Xie and Klionsky, 2007). It was speculated before that direct ER-to-Vacuole protein trafficking is not only important during seed maturation and germination but could also contribute to vacuole biogenesis (Yano et al., 2007; Isono et al., 2010; Katsiarimpa et al., 2013; Michaeli et al., 2014). A recent study using 3D reconstruction and real-time imaging of autophagosome formation revealed that phagophores form at the ER by the consecutive action of ATG5 and ATG8 (Le Bars et al., 2014). However, we were still able to identify provacuoles in different mutants of the core autophagy machinery in which autophagosome formation is inhibited, namely *atg2-1* (Inoue et al., 2006), *atg5-1* and *atg7-2* (Thompson et al., 2005; Hofius et al., 2009). Together with the fact that there was no ATG8-GFP labeling detectable at vacuolar loops, this suggested that macroautophagy is most likely not involved in provacuole formation and thus neither in vacuole biogenesis. This was surprising as both classic models of vacuole biogenesis employ autophagic processes. In the end, we cannot yet fully exclude the possibility that autophagy-related proteins transiently accompany the formation of provacuoles at the ER. The most striking difference between phagophores and provacuoles is the presence of V-ATPases and V-PPases on the latter. In cells of *amsh3* mutants that accumulate autophagosomes in the cytosol (Isono et al., 2010), we detected two double membrane structures next to each other with only one being densely labeled with antibodies against V-PPase, presumably a provacuole. This supports the idea that autophagosomes, unlike provacuoles, are not acidic compartments and only become acidified after they have fused with the vacuole (Klionsky et al., 2008).

Provacuoles were also identified in all other previously tested trafficking mutants and treatments used in this study to inhibit Golgi and post-Golgi trafficking pathways. Though the formation of provacuoles has not been prevented their morphology was often altered, displaying multi-layered membrane stacks. This is particularly interesting since it might show the interdependency of the endosomal trafficking routes that end in the vacuole. As mentioned before, membrane fusion with the vacuole requires several different components, like Rab-GTPases, membrane tethering complexes and SNARE proteins. While Rab7-GTPases and HOPS complexes are recruited from the cytosol, SNARE proteins are mostly tail-anchored proteins and thus have to enter the endosomal trafficking pathway at some point. A recent study demonstrated that in *Arabidopsis* as well, the Guided Entry of Tail-anchored proteins (GET) pathway is an important mechanism to insert SNARE at the level of the ER (Xing et al., 2017). From there,

SNAREs could be transported either as monomers or in inactive *cis*-SNARE complexes. Two TGN/EE localized SNARE complexes that are essential during cytokinesis were shown to be transported to their respective site of action in an inactive *cis*-SNARE complex (Karnahl et al., 2017). In contrast, it is known that the delivery of VAMP713 to the tonoplast is dependent on functional AP3 complexes and SYP22 requires the action of VPS9a and activated Rab5-GTPases (Ebine et al., 2014). Interestingly, both SNAREs, unlike the Qb-SNARE VTI11 (Uemura et al., 2004; Niihama et al., 2005), do not seem to travel along the classic MVB/LE pathway indicating that at least vacuolar SNAREs are usually not transported in a complex. Since monomeric SNAREs can always be integrated into an active *trans*-SNARE complex, the vacuolar SNARE proteins could promote fusion at any given time if paired with other compatible SNAREs. In fact, we observed a case of an MVB/LE fusing with a provacuole, suggesting that both membranes had the correct membrane identity to undergo fusion. On the other hand, inhibiting the transport pathway of individual SNAREs could also lead to their re-routing thus creating unbalanced SNARE compositions in certain compartments or membranes. This, in turn, could create abnormal membrane arrangements that are not fusion-competent anymore and become stabilized. In the *pat2* mutant we observed abnormal accumulations of circular internal membranes derived from the tonoplast. From localization studies in *ap-3δ* mutants we know that VAMP713 mis-localizes to endosomal compartments and the plasma membrane (Ebine et al., 2014). In both AP3 mutants, *pat2* and *ap-3δ*, these internal membranes are present, possibly due to enlarged fusion incompetent membrane sheets that form out of cross-linked *cis*-SNARE complexes with the present Q-SNAREs.

A new tool to study degradation of tonoplast integral proteins

Upon induced knock-down of VPS16 over long time periods tonoplasts became depleted of VHA-a3-mRFP signal and the vacuolar pH rose to even more alkaline values than that of *vha-a2 vha-a3* mutants (Krebs et al., 2010), demonstrating that the transport of all V-ATPases to the vacuole requires the CORVET/HOPS membrane fusion machinery. It was recently proposed that the remaining acidification of vacuoles in *vha-a2 vha-a3* mutants occurs most likely by vesicular trafficking from the TGN/EE (Kriegel et al., 2015). Thus, the more alkaline vacuoles might be the result of impaired membrane fusion of such contributing vesicles.

At the same time VHA-a3-mRFP positive punctae accumulated in the cytosol showing the continuing production of provacuoles, but also implying active turnover of V-ATPases at the tonoplast. In plants, degradation of tonoplast integral proteins is largely elusive

and at least for the potassium channel TPK1 is believed to occur via tonoplast invagination and subsequent separation into the lumen (Maîtrejean and Vitale, 2011). In yeast, a different mechanism was recently identified in which the vacuolar amino acid transporter Ypq1 was first ubiquitinated upon nutrient starvation and then sorted into outward budding transport vesicles (Li et al., 2015). After these intermediate vesicles have pinched off, the transporters become internalized by the ESCRT machinery similar to ILV formation of late endosomes. Accordingly, these vesicles subsequently fuse to the vacuole and release their cargo in a HOPS-dependent manner (Li et al., 2015). From our observations, a similar mode could apply for the degradation of V-ATPases since we did not observe any VHA-a3-mRFP labeled vesicles inside the vacuolar lumen though the increased pH should prevent efficient degradation. It is thus likely that the accumulated VHA-a3-mRFP labeled vesicles represent a mixture of newly synthesized provacuoles and tonoplast degradation vesicles. To distinguish between both populations and to study the tonoplast integral protein degradation in the future we propose a double induction system, called PRV-tool02. It extends the existing line expressing VHA-a3-mRFP in the DEX-inducible amiR-*vps16* by introducing an estradiole (EST)-inducible VHA-a3-GFP. Upon the DEX-induced membrane fusion block indicated by the altered vacuole morphology, the expression of VHA-a3-GFP would co-label emerging provacuoles. Since these provacuoles never reach the vacuole, the putative intermediate degradation vesicles should be labeled only by VHA-a3-mRFP.

Provacuoles contribute the major amount of tonoplast to expanding lytic vacuoles

Our lifetime measurements of late endosomes suggested that the amount of post-Golgi derived membrane contributed to vacuole surface expansion is not enough to allow for their experimentally observed growth rate. Based on the findings that V-ATPases and V-PPases seem to travel on a direct way from the ER to the vacuole, we hypothesized that provacuoles might also pose as the major membrane shuttle to the expanding tonoplast. First and foremost, such a transport system would provide an efficient way to deliver huge amounts of tonoplast material to the vacuole during the phase of rapid cell elongation without reducing the density of vacuolar proton pumps.

So far, by using CLSM VHA-a3 fusion proteins were only detected at the tonoplast but never *en route* to the vacuole. We therefore created an inducible transport system called PRV-tool01, enabling us to specifically visualize provacuoles for the first time *in vivo*. Previous work in our lab suggested that the localization of VHA-AP2-GFP depends on the presence of V-ATPases in the respective compartment. While it localizes to the

TGN/EE and the tonoplast in wild type cells, in *vha-a2 vha-a3* mutants the majority of the protein is retained in the ER (Master thesis by Fabian Fink, 2012). We combined this genetic background with an inducible VHA-a3-mCherry expression system (Figure 14 C). Upon induction of VHA-a3-mCherry expression ER-retained VHA-AP2-GFP was transported to the tonoplast, showing its V-ATPase dependent transport (Figure 15). Based on our hypothesis that V-ATPases are delivered to the vacuole by provacuoles, we speculated that newly assembled V-ATPases containing VHA-a3-mCherrry might take along VHA-AP2-GFP. Since the fluorophores of VHA-AP2-GFP were already fully matured at the beginning of induction, they marked provacuole compartments as they were transported together with newly assembled but not yet fluorescent V-ATPases destined for the tonoplast. This allowed for a clear separation between already existing tonoplast membranes and provacuoles. With 3D super-resolution CLSM we were able to record the entirety of provacuolar membranes in elongating cells, revealing that provacuoles can form individual and enlarged membrane sheets or cup-like structures. Corresponding to their morphology observed in ultra-thin EM sections, it was barely possible to distinguish the single membrane layers of provacuoles. Their fairly enormous size was not expected from our previous observations using IEM where we usually observed smaller structures, but likely reflects the poor representation of 3D structures in 2D images.

Further post-processing followed by surface area calculations demonstrated that within an elongating cell about 60 % of provacuolar membrane surface is present in addition to the existing amount of tonoplast surface area. Unlike the stable number of MVB/LEs, this value directly correlated with the vacuole size strongly suggesting that provacuoles are the main membrane contributor of expanding vacuoles in elongating cells. Considering these findings, the amount of surface area that would need to be provided by MVB/LE trafficking to allow for vacuole expansion decreased considerably. The resultant MVB lifetime increased to about 12.5 minutes, thus resembling values comparable to other eukaryotes (Futter et al., 1996; Rink et al., 2005).

The finding that the size and number of individual provacuoles differed in relation to the overall amount of provacuoles within the cell, inferred that these compartments most likely undergo homotypic fusion before they make contact with the vacuole. Although we cannot yet exclude that the induced expression of VHA-a3-mRFP in the PRV-tool01 possibly leads to an artificially increased amount of produced provacuoles, the unaltered vacuole morphology in the observed cells suggest that there is no significant influence. Additionally, the vacuoles in elongating cells of *vha-a2 vha-a3* mutants do not show any obvious differences in size or morphology in general. This also means that the

production of provacuoles and thus the formation of vacuoles is independent of tonoplast localized V-ATPases and occurs permanently in the root meristem. It would further provide the major advantage that vacuole expansion can occur very fast because only a small number of large provacuoles need to fuse with the tonoplast as compared to thousands of MVB fusions required. Moreover, while late endosomal trafficking might be steady, provacuoles could be produced in advance of cell elongation and act as a membrane storage. This idea was supported by the observation that upon induced knock-down of VPS16 comparatively small punctate signals of VHA-a3-mRFP accumulated preventing the V-ATPases to reach the vacuoles. It is reasonable that due to the induced membrane fusion block the initially formed provacuoles depart from the ER but cannot develop any further, leading to the observed accumulations. In other words, those punctae would represent the smallest provacuolar entities that pinch off at the ER. The fact that the VHA-a3-mRFP signal accumulates in dots rather than in the ER also strongly indicates that provacuoles do not stay in contact with the ER. Interestingly, ultra-structural analysis of such cells revealed a noticeable increase of small and circular structures with a high similarity to previously observed provacuoles (Figure 21). Future experiments need to verify the presence of VHA-a3-mRFP on these compartments to identify them as provacuoles.

Since provacuoles themselves seem to undergo a development that seems to depend on CORVET/HOPS mediated membrane fusion, they have to be equipped with all necessary membrane fusion components. This would explain the MVB-provacuole fusion event we observed by IEM and why the inhibition of Golgi and post-Golgi trafficking routes often affected the morphology but not the formation of provacuoles. It is possible that the impaired delivery or re-routing of vacuolar SNARE proteins to their target membrane could lead to unusual or premature fusion events with other compartments. Such mis-localization was demonstrated before for SYP22 and VAMP713 (Ebine et al., 2014). As a consequence, early unintended fusion events with provacuoles could even deliver vacuolar V-ATPases and other tonoplast proteins to any other subcellular localization with altered SNARE composition. Still, considering that the production of provacuoles happens in advance of vacuole expansion to generate a reserve during cell elongation, it would require a certain control mechanism to prevent premature provacuole fusion with other membranes. During cell plate formation all required SNAREs including the specifically expressed Qa-SNARE KNOLLE are delivered as inactive *cis*-SNARE complexes that have to be actively rendered fusogenic and kept connected (Lauber et al., 1997; Park et al., 2012; Karnahl et al., 2017). Similarly, provacuoles might be intentionally equipped with a set of inactive SNARE bundles that

either require a certain trigger or another separately delivered SNARE at the tonoplast to undergo fusion.

A very recently published set of experiments proposed V-ATPase trafficking to the vacuole via TGN/EE compartments in a Rab7-GTPase independent manner comparable to SYP22 (Feng et al., 2017b). Since it was shown that vacuolar cargo can be delivered without requiring Rab7-GTPase activity (Ebine et al., 2014; Feng et al., 2017a) and that our inducible amiR-*vps16* knock-down system does not allow to distinguish between Rab5- or Rab7-GTPase specific membrane fusion, it is not yet clear which Rab-GTPase promotes V-ATPase trafficking to the vacuole. However, the authors concluded that V-ATPases containing VHA-a3 would travel via the TGN/EE from partial co-localization of YFP-tagged VHA-a3 in cells expressing dominant-negative RFP-ARA7 ($ARA7^{S24N}$) which were additionally treated with BFA (Feng et al., 2017b). From the experiments with multiple blocked transport routes presented in that study it cannot be ruled out that the observed co-localization is due to unintended provacuole fusions. Besides, further experiments to support this model were missing. It could be further argued that the BFA-induced compartments in this dominant-negative Rab5-GTPase background might have acquired an aberrant membrane identity comparable to that of a tonoplast and thus VHA-a3-YFP could co-localize with TGN/EE marker proteins. Moreover, the constant expression of dominant-negative Rab5-GTPases presumably alters the subcellular membrane and compartment identities in general thus leading to severe trafficking errors. Previous studies therefore usually analyzed effects of dominant negative trafficking factors by transient expression (Batistič et al., 2010; Bottanelli et al., 2011; Cui et al., 2014), induced expression (Cui et al., 2014) or chemical inhibition (Richter et al., 2007; Viotti et al., 2010; Scheuring et al., 2011; Viotti et al., 2013; Richter et al., 2014).

Is a provacuole really different from a vacuole?

What distinguishes a provacuole from a vacuole? In the end, it might only be the difference in volume. Imagining a vacuole-free plant cell, *de novo* formation of a lytic vacuole would need to start with a provacuole. As visualized by the PRV-tool01, there can be several independent provacuoles within a cell. The most important prerequisite for a provacuole in order to serve as the initial vacuole is fusion competence to receive incoming post-Golgi trafficking. From IEM images we know that at least MVB/LEs can fuse with provacuoles. In turn, Qa-, Qb- and Qc-SNAREs have to be present in the provacuole membrane. Since there are no other acceptor membranes than the provacuoles, they would receive more and more cargo equipping their surface and lumen with vacuole-specific proteins. In the beginning one thus might expect *de novo*

vacuole formation starting with several small vacuoles that finally fuse again to a single compartment. In fact, experiments with evacuolated protoplast described this morphological order of events (Hörtensteiner et al., 1992; Di Sansebastiano et al., 2001). However, in the context of a developing tissue the contained vacuole volume in dividing cells seems to be distributed equally. This means that there is already a vacuole present as the intended target compartment. Combined with the fact that the size and amount of provacuoles increases, but not their lumen, suggests a yet undiscovered trigger needed to make the provacuole membranes fuse on demand. Since the vacuole surface area multiplies several times when cells enter the elongation phase, such a signal might only happen once during transition.

Identification of other provacuole cargo

The identification of provacuoles as a major transport pathway of proton pumps and membrane material to the vacuole during cell elongation gives rise to interesting future research questions. In addition to the experiments proposed before, it will first be necessary to find out whether provacuoles are restricted to developing cells in the root tip or if they are also present in fully matured cells, e.g. in leaf epidermal cells. The membrane turnover of central vacuoles could possibly be brought to an equilibrium by the steady vesicle flux of the classic vacuolar trafficking routes, rendering provacuoles expendable as tonoplast backup. Future investigations should also focus on the differential targeting of V-ATPases destined to the TGN/EE and the vacuole. The recent identification of a plant specific sequence in VHA-a1 encoding ER-export and TGN/EE retention (Lupanga, 2017) might enable the discovery of a similar sequence for provacuole entry in VHA-a3. Nevertheless, other tools might allow us to identify new cargo for the provacuole route. We recently developed a DEX-inducible Sar1b^{H74L} that can block COP-mediated ER-export as it was shown before in transient or cell-specific expression (Batistič et al., 2010; Feng et al., 2017a). Combining this system with a broad selection of tonoplast integral proteins could reveal other potential cargo of provacuoles.

N-glycosylation is a very common post-translational modification in eukaryotes that is transferred to proteins at the Golgi (Strasser, 2014). It was proposed for proteins in lysosomal membranes that complex glycosylation protects them from being digested by luminal hydrolases (Strasser, 2016). Interestingly, a recent study found that only 4 tonoplast integral membrane proteins in Arabidopsis are modified by complex N-glycosylation, indicating that there is no need for most tonoplast proteins to transit through the Golgi (Pedrazzini et al., 2016). Thus, it might be possible that provacuoles

are the prime transport shuttle for most proteins at the tonoplast. Even if not, most of them could be re-routed once their default pathway is blocked by Sar1b^{H74L} expression.

To study the mechanistic processes involved in provacuole formation we performed a forward genetic screen to find mutants with impaired tonoplast localization of VHA-a3-GFP containing V-ATPases. So far we identified one candidate, *bgo1*. In cells of this mutant we observed aberrant vacuoles without any VHA-a3-GFP labeling. Especially in meristematic cells, these vacuoles display a clearly enlarged and spherical morphology compared to the constricted tubular appearance of normal vacuoles. Interestingly, the same cells contain vacuoles with a normal morphology and VHA-a3-GFP signal at the tonoplast (Figure 22), suggesting a selective process by which V-ATPases containing VHA-a3-GFP are excluded. Deduced from their appearance in both EM and CLSM we assume that their content is watery, thus eliminating them as residual protein storage vacuoles. Still, our results so far point to the conclusion that root cells in *bgo1* mutants contain two distinct types of vacuoles, indicated by the presence or absence of VHA-a3-GFP containing V-ATPases. It was discussed previously whether different types of vacuoles do usually co-exist or if this is the consequence of developmental transitions (Frigerio et al., 2008). In the root meristem of tobacco and pea roots protein storage and lytic vacuoles were observed at the same time within a single cell (Paris et al., 1996; Zheng and Staehelin, 2011). However, this was only the case during the first days after germination when energy reserves from the seed are used up. Since we investigated *bgo1* mutant seedlings usually only after 5 days, there should be no PSVs left as indicated by the lack of PSV-specific TIP expression (Hunter et al., 2007; Gattolin et al., 2011). It was shown before that expression of phaseolin in vegetative tissues does not produce PSVs (Bagga et al., 1992; Frigerio et al., 1998), indicating that PSV proteins are degraded in lytic vacuoles. Nevertheless, the mutation in *bgo1* could possibly lead to *de novo* formation of protein storage vacuoles that do not receive any cargo. But this would conflict with the observation that VHA-a3-GFP labeling can be detected at protein storage vacuoles in developing embryos (data not shown).

Attempts to load the aberrant vacuoles with different luminal dyes to measure their pH were not successful indicating that these compartments might be surrounded by protein-free membranes. However, we determined that the *bgo1* specific vacuoles increase in size over time, suggesting that they are able to receive new membrane material or fuse with one another. This also implies that there are specific membrane fusion factors which allow selective fusion with each other but prevent fusion with VHA-a3-GFP labeled vacuoles. In *Medicago truncatula* symbiosome fusion with the vacuole is avoided by an unique combination of tonoplast and plasma membrane SNAREs in the symbiosome

membrane (Limpens et al., 2009; Gavrin et al., 2014). Similarly, mis-targeted SNAREs could create an exclusive membrane identity of the aberrant *bgo1* vacuoles rendering them non-fusogenic to other compartments but themselves. Future experiments should aim to reveal the proteins constituting this special membrane identity and explore the mechanism by which V-ATPases are not sorted into these compartments.

Conclusion

A new model of vacuole biogenesis in *Arabidopsis thaliana*

In plants, vacuole biogenesis is a process that on one side requires the establishment and maintenance of a unique membrane identity. This is a common feature of all other compartments found in eukaryotic cells ensuring the precise delivery of transport vesicles between them. On the other side, the enormous size of a fully matured vacuole demands the production of enormous amounts of membrane especially during the expansion phase in elongating cells. Compared to other eukaryotes, huge vacuoles are a feature specific to plants. They use this compartment to form big cells with minimal economic cost. During vacuole development the surface area of the tonoplast multiplies within a very short time frame. Previously, the most common model of vacuole biogenesis suggested that multiple small vacuoles fuse into one central vacuole while receiving their membrane material via post-Golgi derived transport vesicles. It also included that growth of small vacuoles is acquired by degradation of cytoplasmic content.

Based on the results presented in this thesis we propose a model in which the lytic vacuole exists and develops always as a single compartment. From a constricted tubular morphology in meristematic cells the lumen inflates during elongation phase and finally transforms into a big central vacuole in fully differentiated cells. Isolated subvolumes may appear occasionally, e.g. by the highly dynamic movement, but can re-fuse with the main vacuole. In accordance with published data, the membrane identity of vacuoles is established by numerous transport vesicles that constantly arrive at the tonoplast. Thereby crucial factors for membrane fusion are delivered, most importantly SNAREs. Furthermore, many other proteins that modify membrane lipids (e.g. kinases) and effectors to recruit cytoplasmic factors (e.g. Rab-GTPases) are required to ensure specific fusion events. The main portion of tonoplast surface area needed during the phase of rapid vacuole expansion is not provided by post-Golgi trafficking but by provacuoles. Provacuoles are synthesized directly at the ER as small, cup-shaped double-membrane structures with barely any lumen. In contrast to previous models, this process does not involve the core autophagy machinery. Afterwards, they pinch off and seem to fuse with each other into extensive sheets. Subsequently, upon fusion with the tonoplast their lumen inflates by the influx from the lytic vacuole thereby displacing the cytosol. Interestingly, provacuoles are not only membrane shuttles but also serve as a protein carrier at least for the two major tonoplast proton pumps, V-PPases and V-ATPases. Thereby, these tonoplast proteins bypass all other endosomal compartments on their way to the vacuole. Still, Golgi and post-Golgi trafficking seems to play a role

during the development of provacuoles since their morphology was affected in several transport mutants. Being tonoplast precursors, provacuoles should share a mostly similar membrane identity with vacuoles thus probably also receiving the same cargo. For the morphological development of vacuoles and their maintenance as a single connected compartment membrane fusion events mediated by CORVET/HOPS tethering complexes are essential. This includes the transport of V-ATPases to the vacuole, the development of provacuoles into large membrane sheets and is probably also true for all other vesicles arriving at the tonoplast.

In conclusion, this thesis provided details about the morphological development of lytic vacuoles in space and time, discovered a new transport route that also serves as the main membrane source of tonoplast expansion during cell elongation and demonstrated the mechanistic importance of membrane tethering complexes during vacuole biogenesis in *Arabidopsis thaliana*. The findings open up many possibilities for future experiments to further understand the molecular mechanisms of provacuole formation, cargo sorting into provacuoles and vacuole development itself.

Methods

Buffers and solutions

Surface sterilization solution (100 mL)

ethanol [70 % (v/v)]	99.95 mL
Triton X-100	50 µL [0.05 % (v/v)]

½ MS medium (1000 mL)

MS basal salt mix	2.16 g
sucrose	5 g (0.5 %)
ddH_2O	add up to 1000mL

Adjust to pH 5.8 and autoclave.

MS = Murashige and Skoog basal salt mixture (Duchefa)

for ½ MS plates (1000 mL)

MS basal salt mix	2.16 g
sucrose	5 g (0.5 %)
ddH_2O	add up to 900 mL

Adjust to pH 5.8.

Phyto agar	5 g (0.5 %)
ddH_2O	add up to 1000 mL

Autoclave.

1/10 MS plates for screening (1000 mL)

MS basal salt mix	0.431 g
sucrose	5 g (0.5 %)
$ZnCL_2$ solution (50 mM)	500 µL (final concentration 50 µM $ZnCl_2$)
MES solution (1M)	10 mL (10 mM)
ddH_2O	add up to 900 mL

Adjust to pH 5.8.

Phyto agar	10 g (1 %)
ddH_2O	add up to 1000 mL

Autoclave.

Stored ½ MS or 1/10 MS medium (for plates) was melted using a microwave and subsequently cooled down to 45 °C in a water bath before pouring. If necessary, antibiotics for transgene selection were added and mixed shortly before pouring the plates.

Infiltration solution for floral dip (100 mL)

sucrose	5 g (5 %)
Silwet	50 µL [0.05 % (v/v)]
$MgSO_4$	2 to 4 crystals
ddH_2O	add up to 100 mL

LB medium (1000 ml)

Bacto tryptone	10 g
Bacto yeast extract	5 g
NaCl	10 g
ddH_2O	add up to 1000 mL

Autoclave.

for LB-plates (1000 mL)

Bacto tryptone	10 g
Bacto yeast extract	5 g
NaCl	10 g
ddH_2O	add up to 1000 mL
Bacto agar	15 g

Autoclave.

pH calibration buffers

The calibration buffers were prepared from the following stock solutions (each 25 mL):

1) 1 M MES (2-(N-morpholino)ethanesulfonic acid)

2) 1 M HEPES (4-(2-hydroxyethyl)-1-piperazineethanesulfonic acid)

3) 1 M Ammonium acetate

4) 1 M BTP (Bis-tris-propane; 1,3-bis(tris(hydroxymethyl)methylamino)propane)

For 25 mL of a designated pH buffer 1.25 mL of 1 M MES or 1 M HEPES were mixed with 1.25 ml of 1 M ammonium acetate and 12.5 mL ddH_2O. Then, the pH was adjusted with BTP or diluted HCl. Afterwards ddH_2O was added to a final volume of 25 mL and the pH was verified again. Each calibration buffer ranging from pH 5.2 to 8.0 was prepared in increments of pH 0.4, sterile-filtrated and stored at 4 °C.

Construct design and molecular cloning

Polymerase chain reactions (PCR), PCR fragment clean-up, ligation and preparation of plasmid DNA from small bacterial cultures (miniprep) were done according to standard protocols. GreenGate cloning was performed according to Lampropoulos et al., 2013.

pUBQ10:GFP-VPS16

The wild type gene of VPS16 (VCL1, AT2G38020) for N-terminal GFP fusion was amplified from *Arabidopsis thaliana* cDNA in a PCR using the primers KS-q2303 and KS-q2308. The PCR fragment was ligated into the pre-opened, blunt-end cloning vector pJet1.2. Sequencing was performed with the primers pJet1.2for, KS-q2311, KS-q2312 and pJet1.2rev. Both, the pJET1.2 vector containing VPS16 and the pUGT2kan standard vector were digested with ApaI and SalI and the cleaned up fragments used for ligation to generate pUBQ10:GFP-VPS16 (p0926). This plasmid was transformed into *A. tumefaciens* GV3101 (p0955) and used to transform *A. thaliana* Col-0 plants.

DEX:amiR-*vps16*

This construct was cloned during a practical course under my supervision by master student Taslima Nahar using the GreenGate system (Lampropoulos et al., 2013). We used the "WMD3" micro RNA design tool (Schwab et al., 2006) at wmd3.weigelworld.org to generate and select specific amiRNA sequences against VPS16 following the official guidelines on this webpage. The amiR-*vps16* sequence was amplified in 4 independent PCR reactions using the primer combinations PrimerA-FW and KS-q2298, KS-q2295 and KS-q2296 as well as KS-q2297 and PrimerB-RV on the pRS300 plasmid containing the miR319a precursor sequence. The fourth PCR was done with the primers KS-q2336 and KS-q2337 using the cleaned up PCR products of the first 3 PCRs. This final PCR product was first digested with Eco31I and then ligated into the pre-opened (with Eco31I) pGGI000 vector. The resulting vector pGGI004 (pKS-I004) was transformed into competent *E.coli* (p0947), sequenced and afterwards used in a GreenGate reaction to create an N supermodule together with the following modules:

Adaptor module	Promoter module	Bypass module	Terminator module	Resistance module	Destination vector
pGGG-H-A adaptor	pGGA-6xOP	amiR-*vps16*	pGGE-rbcs	pGGF-Hygromycin	pGG-N000
AG Lohmann	AG Lohmann	This work	AG Lohmann	AG Lohmann	AG Lohmann

This plasmid (pKS-N004) was transformed into competent *E.coli* cells (p0976). The correct assembly was confirmed with a test digest. In a last GreenGate reaction the final Z-vector was created with the following modules:

Supermodule A	Supermodule B	Destination vector
pGGM-UBQ10:Lh4GR	pGGN-6xOP:amiR-*vps16*	pGG-Z003
AG Schumacher	This work	AG Lohmann

The created plasmid (pKS-Z034) was transformed into competent *E.coli* cells (p0988) to confirm the correct assembly with a test digest. This plasmid was then transformed into *A. tumefaciens* GV3101 (p1002) and used to transform *A. thaliana* Col-0 plants.

DEX:VHA-a3-mCherry

This construct was cloned under my supervision by research assistant Philipp Bellon using the GreenGate system (Lampropoulos et al., 2013). For this construct, the following already existing modules were combined in a GreenGate reaction to create an N supermodule:

Adaptor module	Promoter module	N-module	CDS module	C-module	Terminator module	Resistance module	Destination vector
pGGG-H-A adaptor	pGGA-6xOP	pGGB-N-decoy	pGGC-VHA-a3	pGGD-mCherry	pGGE-rbcs	pGGF-Hygromycin	pGG-N000
AG Lohmann	AG Lohmann	AG Lohmann	AG Schumacher	This work	AG Lohmann	AG Lohmann	AG Lohmann

The resulting plasmid was transformed into competent *E.coli* cells (p1889) and the correct assembly was confirmed with a test digest. In a last GreenGate reaction the final Z-vector was created with the following modules:

Supermodule A	Supermodule B	Destination vector
pGGM-UBQ10:Lh4GR	pGGN-6xOP:VHA-a3-mCherry	pGGZ003
AG Schumacher	This work	AG Lohmann

This plasmid was transformed into competent *E.coli* cells (p1890) and the correct assembly was confirmed with a test digest. It was then transformed into *A. tumefaciens* GV3101 (p1997) and used to transform *A. thaliana* plants expressing VHA-AP2-GFP in the *vha-a2 vha-a3* mutant background.

UBQ:VHA-a3-sfGFP-mRFP

This construct was cloned by research assistant Lotte Bald and PhD student Stefan Scholl using the GreenGate system (Lampropoulos et al., 2013). The pMaM4 plasmid containing sfGFP (Khmelinskii et al., 2012) was provided by the lab of Michael Knop. The coding sequence was amplified using the primers KS-q2235 and KS-q2236. mRFP was amplified from SYP61-pHusion (Luo et al., 2016) with the primers KS-q2233 and KS-q2234. Both primer pairs were designed so that the 3' end of sfGFP and the 5' end of mRFP have a unique overhang that at the same time introduced a linker sequence encoding for 5 amino acids between both fluorophores. The PCR products were digested with Eco31I and ligated into a pre-opened empty pGGD vector creating a D-module with sfGFP and mRFP. The resulting vector pKSD001 (p0820) was sequenced and afterwards used in a GreenGate reaction including the following modules:

Promoter module	N-module	CDS module	C-module	Terminator module	Resistance module	Destination vector
pGGA-UBQ10	pGGB-N-decoy	pGGC-VHA-a3	pGGD-sfGFP-mRFP	pGGE-rbcs	pGGF-BASTA^r	pGG-Z001
AG Lohmann	AG Lohmann	AG Schumacher	This work	AG Lohmann	AG Lohmann	AG Lohmann

The resulting plasmid was transformed into competent *E.coli* cells (p0898) and the correct assembly was confirmed with a test digest. This plasmid was then transformed into *A. tumefaciens* GV3101 (p0901) and used to transform *A. thaliana* Col-0 plants.

Primer list

Table 1: List of primers that were used in this study.

primer number / identifier	primer sequence
pJet1.2for	CGACTCACTATAGGGAGAGCGGC
pJet1.2rev	AAGAACATCGATTTTCCATGGCAG
PrimerA-FW	CTGCAAGGCGATTAAGTTGGGTAAC
PrimerB-RV	GCGGATAACAATTTCACACAGGAAACAG
KS-q2233	TGTGGTCTCATAACGCTAGCATGGCCTCCTCCGAGGACGT
KS-q2234	TATGGTCTCAGCAGTTAGGCGCCGGTGGAGTGGC

KS-q2235	TGTGGTCTCTTCAGTTATGTCCAAGGGTGAAGAGCT
KS-q2236	TGTGGTCTCAGTTAACGGCCTTATAAAGCTCGTCCATTC
KS-q2295	AGCGACGGATATCTGTGTACTTTTCACAGGTCGTGATATG
KS-q2296	AGCGGCGGATATCTGAGTACTTATCAAAGAGAATCAATGA
KS-q2297	GATAAGTACTCAGATATCCGCCGCTCTCTTTTGTATTCCA
KS-q2298	GAAAAGTACACAGATATCCGTCGCTACATATATATTCCTA
KS-q2303	GGGCCCATGGCAAACGTGTCTGTTGC
KS-q2308	GTCGACCTAGGAGGCTCCTTGGAAAGG
KS-q2311	GAGATGCAGAATGATGATTCTGGG
KS-q2312	GCGCGGACCGTGCAATGGAGATCC
KS-q2336	AACAGGTCTCAAACACGAATTCCTGCAGCCCC
KS-q2337	AACAGGTCTCTGCAGGGATCCCCCCATGGCGATGCC

Transformation of competent *E.coli* cells

Competent *E.coli* DH5α cells (stored at -80 °C) were thawed on ice. Afterwards, the plasmid DNA was added (2.5 µL for miniprep DNA and 5 µL for ligation mixes) and incubated for 15 min on ice. After the cells had been heat-shocked for 50 s at 42 °C, 500 µL of LB medium was added. Subsequently, the cells were transferred to a shaking heat block (800 rpm) at 37 °C for at least 60 minutes. Finally, the transformed cells were plated out on LB-agar plates containing the corresponding antibiotic for selection of the transgene.

Transformation of competent *A. tumefaciens* cells (GV3101::pMP90)

Competent *A. tumefaciens* GV3101 cells (stored at -80 °C) were thawed on ice. After 1 – 2 µg plasmid DNA had been added, the tube was gently tapped to mix the solution and incubated for 10 minutes on ice. Subsequently, the cells were frozen in liquid nitrogen for 5 minutes and then incubated for 5 minutes in a heat block set to 37 °C. Following the addition of 800 µL of LB medium the cells were incubated at 30 °C for 2 to 4 hours while shaking at 200 rpm. In the end, the cells were plated out on LB-agar plates containing Gentamycin, Rifampicin and the antibiotic for selection of the transformed plasmid.

Plant material and growth conditions

The plants used in this study were *Arabidopsis thaliana*, ecotype Columbia-0.

Standard growth conditions - Seedlings

After surface sterilization, all seedlings were grown for 5 days in plates containing agar supplemented with ½ MS basal salt mixture and 0.5 % sucrose. The plates were placed in climate chambers set to 22 °C and 16 h light / 8 h darkness cycles.

Standard growth conditions - Plants

Plants were grown on soil in cycles of 16 h light and 8 h darkness. Plants expressing VHA-AP2-GFP in the *vha-a2 vha-3* mutant background were grown under constant light conditions according to Krebs et al., 2010.

Plant transformation

Flowering *Arabidopsis* plants were transformed by the floral dip method according to Clough and Bent, 1998; Zhang et al., 2006. A single colony of *A. tumefaciens* carrying the plasmid of interest was used to inoculate a 5 mL culture and incubated for 24 h at 28 °C. The liquid LB medium was supplemented with Gent, Rif and the corresponding antibiotic of the transferred plasmid. With this, a main culture of 200 mL LB medium was inoculated (1:100) containing the corresponding antibiotics and incubated at 30 °C for 16 h until an OD_{600} between 0.6 and 1.2. The cells were harvested by centrifugation at 5000 rpm for 15 min at 4 °C. The pellet was resuspended in 100 mL infiltration solution. The floral dip was performed by dipping inflorescences into the infiltration solution containing the resuspended *A. tumefaciens* twice for a few seconds. Subsequently, the plants were placed horizontally in plant boxes, covered with autoclave bags and rested for 24 hours before they were transferred to the growth rooms.

For plants expressing VHA-AP2-GFP in *vha-a2 vha-a3* that were transformed with the DEX-inducible VHA-a3-mCherry construct the infiltration solution was directly pipetted on the inflorescences to increase the transformation efficiency.

Genetic crossing of plants

Flowering plants were used to genetically cross two genotypes with each other. Initially, already open flowers of the genotype serving as female were removed. Then, the anthers of this genotype were removed. The remaining stigma was covered entirely with ripe pollen by gently touching it repeatedly with anthers of the second genotype. For each crossing at least 9 flowers were used.

Surface sterilization of seeds

Seeds were surface sterilized for 15 min in a solution of 70 % (v/v) ethanol containing 0.05 % (v/v) Triton X-100. Afterwards, the solution was exchanged by 95 % (v/v) ethanol and the seeds were rinsed for another 10 min. The seeds were then transferred onto a sterile filter paper and left to dry. Sterilized seeds were stratified in the dark at 4 °C for at least 48 h.

Plant lines used in this study

Table 2: List of plant lines and mutants that were used in this study.

Transgenic line	Source
VHP1-GFP (A206K)	Segami et al., 2014
UBQ:2xFYVE-GFP	provided by Joop Vermeer; based on Vermeer et al., 2006
VHA-a1-GFP	Dettmer et al., 2006
VHA-a3-mRFP	Krebs et al., 2010
VMA21-GFP	Neubert et al., 2008
VMA12-mRFP	C. Neubert, unpublished
VHA-a3-mRFP x VMA21-GFP	this study; published in Viotti et al., 2013
gnl1;GNL1 BFA-sens.	Richter et al., 2007
VHA-a1-GFP x VHA-a3-mRFP in *gnl1*;GNL1 BFA-sens.	this study; master thesis of Fabian Fink (Fink, 2012); published in Viotti et al., 2013
pat2-1, *pat2-2*	Feraru et al., 2010
VHA-a3-GFP in *pat2-2*	this study; published in Viotti et al., 2013
siVPS45-10d	Zouhar et al., 2009
amsh3	Isono et al., 2010
atg2-1	Inoue et al., 2006
atg5-1	Thompson et al., 2005; Hofius et al., 2009
atg7-2	Thompson et al., 2005; Hofius et al., 2009
zig1-1 (sgr4-1)	Kato et al., 2002 (Yamauchi et al., 1997)
itt3	Zheng et al., 2014
gfs9-3	Ichino et al., 2014
VHA-AP2-GFP in Col-0	master thesis of Fabian Fink (Fink, 2012)
VHA-AP2-GFP in *vha-a2 vha-a3*	master thesis of Fabian Fink (Fink, 2012)
DEX:VHA-a3-mCherry VHA-AP2-GFP in *vha-a2 vha-a3* (PRV-tool01)	this study; DEX:VHA-a3-mCherry was cloned by Philipp Bellon
GFP-VPS16	this study
DEX:amiR-*vps16*	this study
GFP-VPS16 x DEX:amiR-*vps16*	this study
DEX:amiR-*vps16* x VHA-a3-mRFP	this study
DEX:amiR-*vps16* x VHA-a3-mRFP x VMA21-GFP	this study
VHA-a3-sfGFP-mRFP in Col-0	this study, cloned by Stefan Scholl and Lotte Bald

vha-a2 vha-a3	Krebs et al., 2010
bgo1	this study

Bacterial strains

Escherichia coli (*E. coli*) strain DH5α.

Genotype: F'φ 80ΔlacZΔM15 Δ(lacZYA-argF) U169 recA1 endA1 hsdR17(rk-, mk+) phoA supE44 λ -thi-1 gyrA96relA1.

Agrobacterium tumefaciens (*A. tumefaciens*) strain GV3101::pMP90.

The Ti-plasmid provides Gentamycin (Gent) resistance, the chromosomal encoded resistance is Rifampicin (Rif).

Culturing of bacteria

E. coli DH5α were grown in liquid LB medium supplemented with the respective antibiotic to select for positive transformation as overnight cultures at 37 °C. Newly transformed bacteria were plated out on LB-agar plates and incubated at 37 °C.

A. tumefaciens GV3101 were grown in liquid LB-medium as overnight culture at 28 °C supplemented with Gent, Rif and the respective antibiotic whose resistance is provided by the transformed plasmid. Newly transformed bacteria were plated out on LB-agar plates and incubated at 28 °C for two to three days.

Microscopy

Electron microscopy

The samples that have been observed in this study were high-pressure frozen and freeze-substituted root tips of 5 days old *Arabidopsis thaliana* seedlings of various genetic backgrounds. They were prepared by Corrado Viotti, Stefan Hillmer, Stephanie Gold and myself according to Scheuring et al., 2011; Hillmer et al., 2012. Immunogold labeling was done as previously described (Viotti et al., 2013) using antibodies against endogenous AVP1/VHP1 (dilution 1:3000; CosmoBio; Kobae et al., 2006) or GFP (dilution 1:2000). Specimen were observed using a JEM1400 transmission electron microscope (JEOL) connected to a FastScan F214 digital camera (TVIPS).

Confocal microscopy

Standard CLSM was done using a Leica TCS SP5II microscope (Leica Microsystems) equipped with a Leica HCX PL APO lambda blue 63.0x1.20 UV water immersion objective operating with the Leica Application Suite Advanced Fluorescence software

(LASAF). The microscope was further equipped with two hybrid photodetectors (HyDs, Leica HyD™). In general, images were acquired with a lateral pixel resolution between 50 nm and 96 nm at a speed of 400 Hz with bi-directional scanning and 5-times line averaging. To reduce background fluorescence the pinhole was adjusted between 0.8 and 1.0 airy unit (AU). Super-resolution CLSM was done using a Zeiss LSM880 Airyscan Fast microscope (Zeiss Microscopy).

Table 3: List of fluorophores / dyes and the corresponding lasers that were used in this study as well as excitation wavelengths and detection windows that were applied when using the Leica TCS SP5II microscope.

Fluorophore / dye	Laser	Excitation wavelength	Emission detection window
Propidium iodide	UV-diode	561 nm	650 nm - 700 nm, 615 nm - 675 nm
GFP, sfGFP	VIS-Argon	488 nm	495 nm - 555 nm
BCECF	VIS-Argon	488 nm, 458 nm	495 nm - 555 nm, 500 nm - 560 (pH)
mRFP, mCherry, FM4-64, SNARF-1, Lysotracker-Red DND-99	VIS-DPSS 561	561 nm	570 nm - 680 nm (single fluorophore), 600 nm - 680 nm (two fluorophores)

Post-processing and calculations

All post-processing operations of images were done with Fiji (Fiji Is Just ImageJ, based on ImageJ 1.51d; http://fiji.sc/Fiji; Schindelin et al., 2012).

Basic calculations were performed with Microsoft Office Excel 2007 SP3 MSO from Microsoft Corporation. Advanced calculations, e.g. curve-fitting, correlations analysis and statistics were calculated with OriginPro 2016G (64bit) Sr1 from OriginLab Corporation.

Boxplots presented in this study were generated with OriginPro 2016G (64bit) showing a box indicating the borders of the 25. and 75. percentile, a median line and the average (square). Whiskers indicate outliers with a coefficient of 1.5. Individual data points were usually included.

Pharmacological treatments and staining procedures

Table 4: List of substances (dyes, inhibitors or other chemicals) that were used in this study along with the corresponding working concentrations and standard procedures. * indicates that the dye was used in combination with Pluronic F-127 to enhance loading.

substance	working concentration	procedure
FM4-64	1 µM	5 - 10 min incubation
BCECF	10 µM	2 h staining, 1 h washing
Propidium iodide	10 µg / µL	20 min staining, 20 min washing
SNARF-1 carboxylic acid	10 µM	2 h staining*, 1 h washing
LysoTracker Red DND-99	1 µM	90 min staining, 20 min washing
Pluronic F-127	0.02 %	in combination with staining
Indole-3-acetic acid (IAA)	250 nM, 10 µM	20 h over night
Latrunculin A (LatA)	100 nM, 1 µM	2 h to 3 h
Dimethylsulfoxide (DMSO)		control for DMSO-dissolved chemicals, equal duration
Dexamethazone (DEX)	30 µM	induction as indicated
Concanamycin A (ConcA)	1 µM	3 h or as indicated
Brefeldin A (BFA)	50 µM	3 h
Wortmannin (WM)	33 µM	3 h
Cycloheximide (CHX)	50 µM	1 h (pretreatment)

Acquisition and projection of Z-stacks

Z-stacks were acquired with a maximum step size (Z-axis) of 420 nm. If the pinhole size was reduced below 0.8 AU, the step size was reduced accordingly to a value that is smaller than half of the acquired Z-axis dimension. The stacks were always acquired from the deeper tissue layer towards the outside.

To project acquired Z-stacks the "3D Projection" plugin in Fiji was used. The "Brightest point" method was chosen as projection mode along the "Y-axis". The total rotation was put to 0 degrees while all other default values were kept. Lastly, the "Interpolation" option was activated.

Surface rendering, volume and surface area calculation of vacuoles

In order to calculate the volume and surface area of vacuoles, seedlings were first stained with BCECF and then Z-stacks of individual cells were acquired. Since loading with the luminal dye was very efficient the pinhole and Z-axis step size was reduced as

much as possible to improve Z resolution. To distinguish individual cells, propidium iodide or FM4-64 were optionally used as cell wall or plasma membrane counter staining.

Vacuoles were manually extracted from Z-stacks using the Fiji polygon selection tool in combination with the "clear outside" command for each Z-stack slice. Before rendering, the background noise needs to be reduced and the signal edges of the vacuoles need to be smoothened. For this, two protocols were established.

1) Multi-step protocol (Fiji):

• Duplicate original stack (A) twice, rename the new stacks "2" (B) and "20" (C).

• Perform "Median(3D)" with size of 2 in each dimension on (B) and 20 on (C). For (C), the "Median(3D)" size filter can be reduced down to 15 depending on the quality of the original stack.

• Substracting: (C) - (B) = (D) using the "Image calculator" command.

• Substracting: (B) - (D) = (E) using the "Image calculator" command.

• Perform "Smooth" command twice with (E)

• Use (E) for rendering.

It was verified that when compared, (A) and (E) have the same width of the imaged structures. The purpose is that (E) has now an even surface for rendering that is required for reliable volume and surface calculations.

2) Single-step protocol (Fiji)

The extracted Z-stacks of vacuoles are post-processed with the "Smooth (3D)" command using a calibrated Gaussian with a Sigma value between 0.1 and 0.25, depending on the quality of the Z-stack.

For both protocols, if necessary, background signal must be further reduced applying the "Brightness/Contrast" command.

Surface rendering and volume calculation was done using the "3D viewer" plugin (Schmid et al., 2010). The processed Z-stacks were displayed as surfaces with the color corresponding to the respective channel (BCECF in green, FM4-64 in magenta). In order to render the vacuole volume with the lowest threshold possible, a value above the average background intensity was iteratively determined as threshold. The resampling

factor was always kept at 1. Once rendered, the volume of the object is given in the "Object Properties" of the 3D Viewer "Edit" window.

To determine surface areas, the Z-stacks were processed with the "Isosurface" command of the "BoneJ" plugin (Doube et al., 2010). For surface rendering "BoneJ" utilizes the "3D Viewer", thus the independently computed values are comparable when all rendering settings are kept unchanged for individual rendered objects. Thus, the identical settings for threshold and resampling that were used before were applied for the surface calculation.

4D imaging of vacuoles in root tips

Five days old *Arabidopsis thaliana* seedlings expressing VHP1-GFP (A206K, Segami et al., 2014) were imaged using a Zeiss LSM880 microscope equipped with the Airyscan Fast module. After setting up the appropriate volume dimensions to image the whole epidermal cell layer, consecutive Z-stacks were acquired as fast possible until the cells grew out of the field of view. Each Z-stack of this time series (hyperstack) was then projected as described before. To correct for lateral drift of the specimen, the "StackReg" command of the "Registration" plugin for Fiji was executed on the projected hyperstack using the "Rigid Body" mode. Individual areas of interest were then marked with the rectangular selection tool and manually extracted using the "Duplicate" command.

Vacuole-connectivity Fluorescence Recovery After Photobleaching (vaccFRAP)

Vacuole connectivity measurements were done in epidermal cells of the transition and elongation zone of 5 days old seedling root tips that had been stained with BCECF as described above. FRAP experiments were performed with the "FRAP Wizard" included in the LASAF software. Imaging settings in all measurements were identical. Images of 512 x 512 pixels were acquired with a scan speed of 1400 Hz (bi-directional mode) at a zoom-factor of 6 and 3-times line-averaging. The detection mode of the HyDs was set to "Standard". With these settings individual frames were recorded every 575 ms. To determine the maximum recovery speed (v_{max}) the frame size was reduced to 200 x 400 pixels to acquire images every 239 ms.

The cells containing the vacuoles of interest were randomly selected and placed entirely in the field of view. The Z-foucs was adjusted to their equatorial plane. For bleaching the "Point-Bleach" mode was used. The target area, a vacuole sector that appeared strongly convoluted or isolated, was selected setting a single bleach-point for 300 to 500 ms. For optimal measurements, the bleach point was selected close to the top edge of the field of view. Depending on loading efficiency the bleach laser power was adjusted between 35 to 50 %. The timing of the experiments was set to 4 pre-bleach frames, the single

bleaching frame and the post-bleach frames were set to a number between 25 and 200, depending on the respective genotype. A maximum of 5 FRAP measurements per root was allowed. For each genotype, treatment and biological replicate at least 50 vacuoles were analyzed.

The quantification of the dlFRAP experiments was done with the "FRAP_profiler" plugin (Lynch et al., 2012). First, individual FRAP time series were loaded into Fiji and the entire vacuole area of the cell of interest was marked at the last pre-bleach frame using the rectangular selection tool. This area was added to the "ROI manager". In the same pre-bleach frame the elliptical selection tool was used to mark the vacuole area that was bleached. This area was also added to the ROI manager. Subsequently, the "FRAP_profiler" plugin was started selecting "single exponential recovery" as curve fitting method. As time interval the corresponding time per frame was entered as a unit of seconds (decimal points had to be entered as "."). The measured values for "% mobile phase" and "t1/2" were kept. FRAP measurements with a mobile phase fraction below 30 % were excluded. Experiments with recovery half-times (t1/2) below 60 % of the frame interval were counted as immediately recovered vacuoles (Type I).

MVB diameter calculation

To determine the average diameter of MVB/LEs only EM images of untreated 5 days old *Arabidopsis thaliana* Col-0 seedling root tips were used. First, the scale of the images was adjusted with the "Set Scale" command in Fiji. After this, the horizontal and vertical diameter for each observable MVB/LE was measured with the "straight line" selection tool. Both values were averaged and used to calculate the average mean diameter of n = 210 MVB/LEs.

Quantification of MVB number per cell

Epidermal cells of 5 days old seedlings expressing UBQ10:2xFYVE-GFP (provided by Joop Vermeer, based on Vermeer et al., 2006) were stained with propidium iodide as described above. Z-stacks with an image format of 1024 x 1024 pixels were acquired with the resonant scanner in bi-directional scan mode at approximately 16 kHz and 2-times line-averaging. The pinhole was set to 1 AU and the HyDs were put to "BrightR" mode.

Using Fiji, individual cells were manually extracted from Z-stacks using the polygon selection tool in combination with the "clear outside" command for each Z-stack slice and each detection channel based on the propidium iodide staining. The Z-stacks of 2xFYVE-GFP were then processed with the "Gaussian Blur (3D)" command using a sigma value of 2 for all dimensions. The number of MVB/LEs was determined with the

"3D Objects Counter" plugin (Bolte and Cordelières, 2006) after the threshold was set to a value that excluded background noise. The volume of the corresponding cell was determined using the "3D Viewer" plugin based on the propidium iodide signal outlining the cell.

Quantification of cell elongation

The 2D time lapse data sets of growing root tips were recorded by Melanie Krebs with a Leica TCS SP5II microscope equipped with a 20x objective. The seedlings were mounted in special longterm imaging chambers as described previously (Krebs and Schumacher, 2013; Keinath et al., 2015). Length of cells in the transition and elongation zone were measured using the "straight line" selection tool in Fiji. The number of frames it took for individual cells to increase in length by 2.5-times was counted and multiplied by the frame interval.

MVB tracking and lifetime calculation

Epidermal cells of 5 days old seedlings expressing UBQ10:2xFYVE-GFP (provided by Joop Vermeer, based on Vermeer et al., 2006) were stained with propidium iodide as described above. Z-stacks with an image format of 512 x 512 pixels were acquired at a zoom-factor of 5 with the resonant scanner in bi-directional scan mode at approximately 16 kHz and 4-times line-averaging. The pinhole was set to 2 AU and the HyDs were put to "BrightR" mode. The Z-stacks were processed with the "Gaussian Blur (3D)" command using a sigma value of 2 for all dimensions and projected.

Compartment tracking and lifetime quantification was done with the "TrackMate" plug-in (version 2.8.1) for ImageJ (Tinevez et al., 2016). For spot detection the "LoG detector" filter was applied with an estimated diameter of 0.6. The threshold was adjusted in accordance to the signal intensity (usually set between 15 and 20) in combination with subpixel localization. After spot detection the initial thresholding was done automatically to increase prior spot detection quality. For visualization the "HyperStack Displayer" with uniform color was used. Tracking was done with the simple LAP tracker (linking conditions: maximum distance 20 µm, gap-closing conditions: maximum distance 15 µm and 4 frames, depends on Z-stack interval). The tracking results were transferred to a Microsoft Excel-sheet and sorted for track duration according to frame numbers. Since the maximum allowed lifetime of MVB/LEs from the model calculation was 300 s or 43 frames (7 s per frame i.e. Z-stack), all compartments whose tracks started and ended within the first 43 frames, were excluded. In addition, tracks starting within the last 43 frames and reaching the maximum remaining number of frames were not taken into

account. All other tracks were collected and multiplied with the Z-stack interval of 7 s to receive their lifetime.

FRAP of VHA-a3-mRFP and VHA-a1-GFP in *gnl1*;GNL1 BFA-sens

5 days old *Arabidopsis thaliana* seedlings expressing VHA-a1-GFP and VHA-a3-mRFP in *gnl1*;GNL1 BFA-sens background were first incubated for 3 h in 50 µM BFA and then mounted into special longterm imaging chambers as described previously (Krebs and Schumacher, 2013; Keinath et al., 2015) containing BFA-supplemented ½ MS medium. After recording a prebleach image the region of interest was selected and bleached (3 times scanning, 5-times line averaging, at 100 % laser power with deactivated detectors), reducing the fluorescence intensity of VHA-a1-GFP and VHA-a3-mRFP to approximately 50 %. Subsequently, postbleach images were acquired with the initial prebleach settings at the indicated time points. FRAP was quantified using the LASAF software. To calculate the relative fluorescence intensity for each time point, the mean fluorescence intensity of the indicated region of interest was divided by the mean fluorescence intensity of the prebleach frame.

In order to inhibit *de novo* synthesis of proteins in this experimental setup, the seedlings were pretreated with 50 µM CHX for 1 h before BFA was added. All further media in these experiments contained CHX as well.

Quantification of vacuolar loops

Vacuolar loops were counted manually in the root meristematic zone of 5 days old seedlings expressing VHA-a3-GFP (also VHA-a3-GFP in *pat2-2*) based on their increased fluorescence intensity. For VHA-a3-mRFP and all other investigated genotypes the seedlings were first stained with BCECF as described above. Z-stacks were acquired at a stepsize of 380 nm and a format of 2400 x 1200 pixels (zoom-factor = 1), overlapping to about 10 %.

Line intensity profiles were generated with Fiji by first drawing a line of interest in the respective image using the "Straight line" tool and then executing the "Plot Profile" command.

Super-resolution microscopy - Quantification of provacuole surface area

For these experiments we used 7 days old PRV-tool01 seedlings (UBQ:VHA-AP2-GFP DEX:VHA-a3-mCherry in *vha-a2 vha-a3*) that had been induced for 48 h in liquid ½ MS medium supplemented with 30 µM DEX. Super-resolution microscopy of the PRV-tool01 was performed with a Zeiss LSM880 Airyscan Fast microscope equipped with a C-Apochromat 40x/1.2 W Korr FCS M27 objective. The airyscan mode was set to

superresolution. Z-stacks were recorded in 16-bit with a pixel size of 51 x 51 nm (lateral) and 225 nm Z-axis stepsize. The pixel dwell time was 0.68 µs, line-averaging was set to 2 and the pinhole opened at 109 µm. GFP and mCherry fluorescence was detected with ILEX (interleaved excitation) using the filters BP 495-550 and LP570. The activated beam splitter was MBS 488/561. The airyscan post-processing parameter were for both channels (ChA-T1 and ChA-T2) between 7.8 and 8.0 (3D).

To quantify the total provacuole surface area per cell and compare it to the amount of the corresponding tonoplast surface, individual cells were manually extracted from Z-stacks with Fiji using the polygon selection tool in combination with the "clear outside" command for each Z-stack slice covering the cell of interest. Afterwards, the tonoplast signal of VHA-AP2-GFP was removed from the Z-stacks by substracting the VHA-a3-mCherry fluorescence with the "Image Calculator" plugin of Fiji. All extracted Z-stacks were post-processed with the "Smooth (3D)" command using a calibrated Gaussian with a Sigma value of 0.15. The amount of surface area was calculated with the "3D Objects Counter" plugin. The threshold was adjusted so that all membranes were selected. A minimum size filter of 2000 was set for all measurements. Annotated structures were verified by comparing the calculated surface and volume maps with the corresponding input Z-stack to exclude falsely identified objects. For provacuoles, all annotated structures smaller than 25 µm² were excluded to avoid possible TGN/EE compartments. The surface area measurements of vacuoles and provacuoles for all examined cells were collected in a Microsoft Excel-sheet calculating their relative amount. Further quantification of correlation between provacuole and vacuole surface area, the number of provacuoles per cell and sorting by size was done with OriginPro 2016G 64bit (OriginLabs).

Knockdown efficiency of amiR-*vps16*

To measure the knockdown efficiency of induced amiR-*vps16*, DEX:amiR-*vps16* plants were crossed with plants expressing GFP-VPS16 and their progeny selectively propagated untill both transgenes were homozygous. For each population of the biological replicate 16 5 days old *Arabidopsis thaliana* seedlings expressing GFP-VPS16 in the amiR-*vps16* background were used. The GFP fluorescence in root tips were imaged with a Leica TCS SP5II microscope (Leica Microsystems) equipped with a Leica HCX PL APO CS 20.0x0.70 IMM UV immersion objective. All initially adjusted settings were kept unchanged. The images of 1024 x 1024 pixels were acquired at a zoom-factor of 1 with a line averaging of 5, the HyD was set to standard acquisition mode and the pinhole opened to 2 AU. First, the seedling root tips were imaged, numbered and then each one of them was kept separately in wells filled with either liquid ½ MS medium supplemented with DMSO or DEX. After 96 h of incubation, the seedling root tips were

imaged again. For the analysis, the images of each seedling before and after incubation were compared by measuring the mean fluorescence intensity of the root tip. For this, the polygonal selection tool of Fiji was used in combination with the "Measurement" command. The intensity values before induction were set to 100% and the relative change was determined and averaged for each treatment and replicate. Calculations were done in Microsoft Excel and OriginPro 2016G 64bit (OriginLabs).

Diameter quantification of aberrant vacuoles in *bgo1* mutants

The average diameter of abnormal vacuoles in *bgo1* mutants was measured from transmitted light channel images acquired with the Leica TCS SP5II microscope using the "straight line" selection tool and "Measure" command of Fiji. Before, the VHA-a3-GFP fluorescence as well as the transmitted light of 5 days old *bgo1* seedling root tips was detected with standard settings. For the analysis the images were put side-by-side to identify vacuoles without VHA-a3-GFP labeling. The average aberrant vacuole diameter in the meristematic and differentiation zone of *bgo1* mutants grown on ½ MS agar was compared to those grown on ½ MS medium supplemented with 50 µM $ZnCl_2$. Calculations were done in Microsoft Excel and OriginPro 2016G 64bit (OriginLabs).

pH measurements in vacuoles

Vacuolar pH measurements with BCECF (Krebs et al., 2010) require a calibration curve. For this, 5 days old *Arabidopsis thaliana* Col-0 seedlings were stained with BCECF as described above. Subsequently, at least 15 seedlings were incubated for 10 to 15 minutes in each pH calibration buffer ranging from pH 5.2 to pH 8.0 (with increments of pH 0.4) and imaged. pH imaging was done by sequential scanning in a format of 1024 x 1024 pixels at 700 Hz (bi-directional scanning) with a zoom-factor of 2.5 and 5-times line-averaging. With the first scan BCECF was excited using a laser wavelength of 488 nm and emitted fluorescence was detected between 500 nm and 560 nm. For the second scan the same detection window was applied but BCECF was excited using a laser wavelength of 458 nm.

For each pH calibration step all images were imported to Fiji and combined into two independent image stacks containing all acquired images that were excited at 488 nm and 458 nm, respectively. The image stacks were renamed accordingly to "488" and "458".

Then, the following macro, created by Dr. Melanie Krebs, was used to select and quantify the fluorescent signal and intensities in each pair of images:

```
for (i=1; i<=nSlices; i++)
{selectWindow("488");
run("Duplicate...", "title=488-1");
run("Mean...", "radius=2");
setThreshold(2, 254);
run("Create Selection");
run("Add to Manager");
close();
selectWindow("488");
roiManager("Select", 0);
run("Measure");
run("Select None");
selectWindow("458");
roiManager("Select", 0);
run("Measure");
run("Select None");
roiManager("Delete");
selectWindow("488");
run("Next Slice [>]");
selectWindow("458");
run("Next Slice [>]");}
run("Close All");
```

The obtained values were collected in a Microsoft-Excel sheet to calculate their ratio. All ratio values of the individual pH calibration steps were then averaged. With these values a sigmoidal Boltzmann fit was performed using OriginPro 2016G 64bit (OriginLabs). The function of this fitted curve was used to extrapolate pH values of experimentally obtained ratio values.

For pH measurements in amiR-*vps16* and amiR-*vps16* x VHA-a3-mRFP, seedlings were grown for 5 days on ½ MS agar plates and then transferred into well plates containing liquid ½ MS medium supplemented with either DMSO (control) or DEX (induction). Subsequently, the seedlings were incubated for either 48 h or 96 h. The recorded images of amiR-*vps16* x VHA-a3-mRFP seedlings induced for 96 h were grouped according to the localization of the VHA-a3-mRFP signal that was recorded in an additional scan.

EMS mutagenesis and screening

The mutagenesis of *Arabidopsis thaliana* seeds expressing VHA-a3-GFP (line #1-6) was done with ethyl methane sulfonate (EMS) according to the protocol of Glazebrook and

Weigel (Weigel and Glazebrook, 2006). To approximately use 40000 seeds, 1 g of freshly propagated seeds were used (25 µg / seed). For EMS mutagenesis 135 µl of EMS (ready-to-use solution from SIGMA) were added to a total volume of 45 mL, corresponding to 0.3 % (v/v) EMS. The seeds were incubated in this solution for 15 h over night and rinsed 10 times afterwards. For the last washing step the seeds were incubated for 1 h to let residual EMS diffuse out. The mutagenized seeds were then taken up into 1 L of 0.1 % agarose solution and pipetted onto soil. The soil was prepared in rectangular pots (13 pots per tray, 988 pots in 76 trays) and 1 mL of seed containing solution was equally distributed per pot. To provide sufficient humidity for the seeds and developing seedling within the first week, all trays were covered with transparent film. M1 plants were harvested in pools of approximately 40 plants (each pot corresponds to a single pool). The efficiency of the EMS mutagenesis was assessed by counting the number of clear and aborted seeds in 50 randomly picked siliques of M1 plants (14 % aborted seeds, 7 % clear seeds). Furthermore, the number of abnormal developmental phenotypes of 5 days old M2 seedlings was quantified.

For screening, 364 seeds of an individual M2 family were transferred with a toothpick onto 1/10 MS plates containing 50 µM $ZnCl_2$ (7 plates á 2*26 seeds). VHA-a3-GFP seeds (parent genotype) as well as *vha-a2 vha-a3* seeds were used as controls for each screen experiment. After 12 days of growth under long day conditions M2 seedlings displaying a short root phenotype comparable to that of the *vha-a2 vha-a3* mutants were investigated at a confocal microscope to evaluate the subcellular VHA-a3-GFP signal. Seedlings with abnormal VHA-a3-GFP localization and/or vacuolar shape were transferred to soil and propagated.

Abbreviations

%	percent
°C	degree Celsius
α-SNAP	alpha-soluble NSF attachment protein
µg	micro gram micro
µL	micro litre
µM	micro molar
µm	micrometre(s)
6x OP	6x Operator-Promoter
amiR	artificial micro RNA
A_O	surface area
AP3	adaptor protein-3
Arabidopsis	*Arabidopsis thaliana*
BCECF	2',7'-bis(2-carboxyethyl)-5(6)-carboxyfluorescein
BFA	Brefeldin A
bgo1	*big gloomy orb 1*
bp	base pair(s)
CCV	clathrin-coated vesicle
cDNA	complementary DNA
CDS	coding sequence
CHCR	clathrin heavy chain repeat
CLSM	confocal laser scanning microscopy
Col-0	Columbia-0
ConcA	Concanamycin A

COPI/II	coat protein complex I or coat protein complex II
CORVET	class C core vacuole/endosome tethering
DEX	dexamethasone
DMSO	dimethylsulfoxid
DNA	deoxyribonucleic acid
E.coli	*Escherichia coli*
EM	electron microscopy
e.g.	exempli gratia/ for example
eGFP	enhanced monomeric green fluorescent protein
EMS	ethyl methanesulfonate
ER	Endoplasmic Reticulum
ESCRT	Endosomal Sorting Complex Required for Transport
F	filial generation
FM 4-64	(N-(3-triethylammoniumpropyl)-4-(6-(4-(diethylamino)phenyl)hexatrienyl)-pyridinium dibromide)
FRAP	Fluorescence Recovery After Photobleaching
gDNA	genomic DNA
GDP	Guanosine diphosphate
Golgi	Golgi Apparatus
GTP	Guanosine-5'-triphosphate
h	hour(s)
HOPS	homotypic vacuole fusion and protein sorting
i.e.	*id est* = that is
IEM	immunocytochemistry EM

kb	kilobases
L	liter(s)
LV	lytic vacuole
M	molar
min	minute(s)
ml	milliliter(s)
mM	millimolar
mRFP	monomeric red fluorescent protein
MS	Murashige & Skroog
MVB/LE	multivesicular body/late endosome
ng	nanogram
nM	nanomolar
nm	nanometer(s)
NSF	N-ethylmaleimide-sensitive factor
PCR	polymerase chain reaction
pH	potential of hydrogen/ pondus hydrogenii
PI3K	phosphatidylinositol 3-kinase
PI3P	phosphatidylinositol 3-phosphate
PRV	provacuole
PSV	protein storage vacuole
RNA	ribonucleic acid
rpm	rounds per minute
RT	room temperature (22°C)
s	second(s)

SD	standard deviation
sfGFP	superfolder GFP
SNARE	soluble N-ethylmaleimide-sensitive factor (NSF) attachment receptor
SYP	syntaxin of plants
T-DNA	transfer DNA
TGN/EE	trans-Golgi network/ early endosome
V	Volume
VAMP711	vesicle-associated membrane protein 711
vaccFRAP	vacuole connectivity FRAP
V-ATPase	vacuolar-type proton ATPase
V-PPase	vacuolar-type H^+- pyrophosphatase
VPS16	vacuole protein sorting 16
VTI11	Vesicle transport through interaction with t-SNAREs homolog 11
WM	wortmannin
WT	wild type

References

Amelunxen, F. and Heinze, U. (1984). On the development of the vacuole in the testa cells of Linum seeds. Eur J Cell Biol **35**: 343–354.

Andrés, Z., Pérez-Hormaeche, J., Leidi, E.O., Schlücking, K., Steinhorst, L., McLachlan, D.H., Schumacher, K., Hetherington, A.M., Kudla, J., Cubero, B., and Pardo, J.M. (2014). Control of vacuolar dynamics and regulation of stomatal aperture by tonoplast potassium uptake. Proc. Natl. Acad. Sci. U. S. A. **111**: E1806-14.

Asensio, C.S., Sirkis, D.W., Maas, J.W., Egami, K., To, T.L., Brodsky, F.M., Shu, X., Cheng, Y., and Edwards, R.H. (2013). Self-Assembly of VPS41 Promotes Sorting Required for Biogenesis of the Regulated Secretory Pathway. Dev. Cell **27**: 425–437.

Askani, J.C. (2015). The function of tethering complexes in vacuole development in Arabidopsis thaliana Master Thesis Presented to the Faculty of Biosciences of the Ruprecht-Karls-Universität Heidelberg.

Bagga, S., Sutton, D., Kemp, J.D., and Sengupta-Gopalan, C. (1992). Constitutive expression of the β-phaseolin gene in different tissues of transgenic alfalfa does not ensure phaseolin accumulation in non-seed tissue. Plant Mol. Biol. **19**: 951–958.

Bailey, I.W. (1930). The cambium and its derivative tissues. Zeitschrift für Zellforsch. und Mikroskopische Anat. **10**: 651–682.

Bak, G., Lee, E.-J., Lee, Y., Kato, M., Segami, S., Sze, H., Maeshima, M., Hwang, J.-U., and Lee, Y. (2013). Rapid structural changes and acidification of guard cell vacuoles during stomatal closure require phosphatidylinositol 3,5-bisphosphate. Plant Cell **25**: 2202–16.

Balderhaar, H.J. kleine and Ungermann, C. (2013). CORVET and HOPS tethering complexes - coordinators of endosome and lysosome fusion. J. Cell Sci. **126**: 1307–16.

Barberon, M., Dubeaux, G., Kolb, C., Isono, E., Zelazny, E., and Vert, G. (2014). Polarization of IRON-REGULATED TRANSPORTER 1 (IRT1) to the plant-soil interface plays crucial role in metal homeostasis. Proc. Natl. Acad. Sci. U. S. A. **111**: 8293–8.

Le Bars, R., Marion, J., Le Borgne, R., Satiat-Jeunemaitre, B., and Bianchi, M.W. (2014). ATG5 defines a phagophore domain connected to the endoplasmic reticulum during autophagosome formation in plants. Nat. Commun. **5**: 4121.

Batistič, O., Waadt, R., Steinhorst, L., Held, K., and Kudla, J. (2010). CBL-mediated targeting of CIPKs facilitates the decoding of calcium signals emanating from distinct cellular stores. Plant J. **61**: 211–222.

De Benedictis, M., Bleve, G., Faraco, M., Stigliano, E., Grieco, F., Piro, G., Dalessandro, G., and Di Sansebastiano, G. Pietro (2013). AtSYP51/52 functions diverge in the post-golgi traffic and differently affect vacuolar sorting. Mol. Plant **6**: 916–930.

Bensley, R.R. (1910). On the nature of the canalicular apparatus of animal cells. Biol. Bull. **19**: 179–194.

Berger, F., Hung, C.Y., Dolan, L., and Schiefelbein, J. (1998). Control of cell division in the root epidermis of Arabidopsis thaliana. Dev Biol **194**: 235–245.

Bolte, S. and Cordelieres, F.P. (2006). A guided tour into subcellular colocalisation analysis in light microscopy. J. Microsc. **224**: 13–232.

Bolte, S. and Cordelières, F.P. (2006). A guided tour into subcellular colocalization analysis in light microscopy. J. Microsc. **224**: 213–232.

Bottanelli, F., Foresti, O., Hanton, S., and Denecke, J. (2011). Vacuolar Transport in Tobacco Leaf Epidermis Cells Involves a Single Route for Soluble Cargo and Multiple Routes for Membrane Cargo. Plant Cell **23**: 3007–3025.

Campbell, R.E. et al. (2002). A monomeric red fluorescent protein. Proc. Natl. Acad. Sci. U. S. A. **99**: 7877–82.

Cardona-López, X., Cuyas, L., Marín, E., Rajulu, C., Irigoyen, M.L., Gil, E., Puga, M.I., Bligny, R., Nussaume, L., Geldner, N., Paz-Ares, J., and Rubio, V. (2015). ESCRT-III-Associated Protein ALIX Mediates High-Affinity Phosphate Transporter Trafficking to Maintain Phosphate Homeostasis in Arabidopsis. Plant Cell **27**: 2560–81.

Carter, C., Pan, S., Zouhar, J., Avila, E.L., Girke, T., and Raikhel, N. V (2004). The vegetative vacuole proteome of Arabidopsis thaliana reveals predicted and unexpected proteins. Plant Cell **16**: 3285–303.

Catalano, C.M., Czymmek, K.J., Gann, J.G., and Sherrier, D.J. (2007). Medicago truncatula syntaxin SYP132 defines the symbiosome membrane and infection droplet membrane in root nodules. Planta **225**: 541–550.

Christensen, C. a, Subramanian, S., and Drews, G.N. (1998). Identification of gametophytic mutations affecting female gametophyte development in Arabidopsis. Dev. Biol. **202**: 136–151.

Clough, S.J. and Bent, A.F. (1998). Floral dip: A simplified method for Agrobacterium-mediated transformation of Arabidopsis thaliana. Plant J. **16**: 735–743.

Coonrod, E.M., Graham, L.A., Carpp, L.N., Carr, T.M., Stirrat, L., Bowers, K., Bryant, N.J., and Stevens, T.H. (2013). Homotypic Vacuole Fusion in Yeast Requires Organelle Acidification and Not the V-ATPase Membrane Domain. Dev. Cell **27**: 462–468.

Cui, Y., Shen, J., Gao, C., Zhuang, X., Wang, J., and Jiang, L. (2016a). Biogenesis of Plant Prevacuolar Multivesicular Bodies. Mol. Plant **9**: 774–786.

Cui, Y., Zhao, Q., Gao, C., Ding, Y., Zeng, Y., Ueda, T., Nakano, A., and Jiang, L. (2014). Activation of the Rab7 GTPase by the MON1-CCZ1 Complex Is Essential for PVC-to-Vacuole Trafficking and Plant Growth in Arabidopsis. Plant Cell **26**: 2080–2097.

Cui, Y., Zhao, Q., Xie, H.-T., Wong, W.S., Wang, X., Gao, C., Ding, Y., Tan, Y., Ueda, T., Zhang, Y., and Jiang, L. (2016b). MONENSIN SENSITIVITY 1 (MON1)/CALCIUM CAFFEINE ZINC SENSITIVITY 1 (CCZ1)-mediated Rab7 activation regulates tapetal programmed cell death and pollen development. Plant Physiol.: pp.00988.2016.

D'Ippólito, S., Arias, L.A., Casalongué, C.A., Pagnussat, G.C., and Fiol, D.F. (2017). The DC1-domain protein VACUOLELESS GAMETOPHYTES is essential for

development of female and male gametophytes in Arabidopsis. Plant J.: 261–275.

Dangeard, P. (1923). Recherches de biologie cellulaire. Évolution du systéme vacuolaire chez les végétaux. Le Bot. **15**.

Deeks, M.J., Calcutt, J.R., Ingle, E.K.S., Hawkins, T.J., Chapman, S., Richardson, A.C., Mentlak, D.A., Dixon, M.R., Cartwright, F., Smertenko, A.P., Oparka, K., and Hussey, P.J. (2012). A superfamily of actin-binding proteins at the actin-membrane nexus of higher plants. Curr. Biol. **22**: 1595–1600.

Desfougères, Y., Vavassori, S., Rompf, M., Gerasimaite, R., and Mayer, A. (2016). Organelle acidification negatively regulates vacuole membrane fusion in vivo. Sci. Rep. **6**: 29045.

Dettmer, J., Hong-Hermesdorf, A., Stierhof, Y.-D., and Schumacher, K. (2006). Vacuolar H+-ATPase Activity Is Required for Endocytic and Secretory Traf cking in Arabidopsis. Plant Cell **18**: 715–730.

deVries, H. (1885). Plasmolytische Studien über die Wand der Vakuolen. Jahrb. Bot. **16**: 465–598.

deVries, H. (1877). Untersuchungen über die mechanischen Ursachen der Zellstreckung.

Doube, M., Klosowski, M.M., Arganda-Carreras, I., Cordelières, F.P., Dougherty, R.P., Jackson, J.S., Schmid, B., Hutchinson, J.R., and Shefelbine, S.J. (2010). BoneJ: Free and extensible bone image analysis in ImageJ. Bone **47**: 1076–1079.

Drews, G.N. and Koltunow, A.M.G. (2011). The female gametophyte. Arabidopsis Book **9**: e0155.

Dujardin, F. (1841). Histoire naturelle des zoophytes: Infusiores.

Ebine, K., Inoue, T., Ito, J., Ito, E., Uemura, T., Goh, T., Abe, H., Sato, K., Nakano, A., and Ueda, T. (2014). Plant vacuolar trafficking occurs through distinctly regulated pathways. Curr. Biol. **24**: 1375–1382.

Ebine, K., Okatani, Y., Uemura, T., Goh, T., Shoda, K., Niihama, M., Morita, M.T., Spitzer, C., Otegui, M.S., Nakano, A., and Ueda, T. (2008). A SNARE complex unique to seed plants is required for protein storage vacuole biogenesis and seed development of Arabidopsis thaliana. Plant Cell **20**: 3006–3021.

Esmail, S., Yao, Y., Kartner, N., Li, J., Reithmeier, R.A.F., and Manolson, M.F. (2016). N-Linked Glycosylation Is Required for Vacuolar H+-ATPase (V-ATPase) a4 Subunit Stability, Assembly, and Cell Surface Expression. J. Cell. Biochem. **117**: 2757–2768.

Fasshauer, D., Sutton, R.B., Brunger, A.T., and Jahn, R. (1998). Conserved structural features of the synaptic fusion complex: SNARE proteins reclassified as Q- and R-SNAREs. Proc. Natl. Acad. Sci. U. S. A. **95**: 15781–6.

Feng, Q.-N., Song, S.-J., Yu, S.-X., Wang, J.-G., Li, S., and Zhang, Y. (2017a). AP3 adaptor protein-dependent vacuolar trafficking involves a subpopulation of COPII and HOPS tethering proteins. Plant Physiol.: pp.00584.2017.

Feng, Q.-N., Zhang, Y., and Li, S. (2017b). Tonoplast targeting of VHA-a3 relies on a Rab5-mediated but Rab7-independent vacuolar trafficking route. J. Integr. Plant Biol. **59**: 230–233.

Feraru, E., Paciorek, T., Feraru, M.I., Zwiewka, M., De Groodt, R., De Rycke, R., Kleine-Vehn, J., and Friml, J.J. (2010). The AP-3 β adaptin mediates the biogenesis and function of lytic vacuoles in Arabidopsis. Plant Cell **22**: 2812–24.

Fink, F. (2012). The V-ATPase in Arabidopsis thaliana: A closer look to targeting, new interaction partners and its role for ER acidification.

Finnigan, G.C., Cronan, G.E., Park, H.J., Srinivasan, S., Quiocho, F.A., and Stevens, T.H. (2012). Sorting of the yeast vacuolar-type, proton-translocating ATPase enzyme complex (V-ATPase): Identification of a necessary and sufficient Golgi/endosomal retention signal in Stv1p. J. Biol. Chem. **287**: 19487–19500.

Fratti, R.A., Collins, K.M., Hickey, C.M., and Wickner, W. (2007). Stringent 3Q•1R composition of the SNARE 0-layer can be bypassed for fusion by compensatory SNARE mutation or by lipid bilayer modification. J. Biol. Chem. **282**: 14861–14867.

Frigerio, L., Hinz, G., and Robinson, D.G. (2008). Multiple vacuoles in plant cells: Rule or exception? Traffic **9**: 1564–1570.

Frigerio, L., Virgilio, M. de, Prada, A., Faoro, F., and Vitale, A. (1998). Sorting of Phaseolin to the Vacuole Is Saturable and Requires a Short C-Terminal Peptide. Plant Cell Online **10**: 1031–1042.

Fujiwara, M., Uemura, T., Ebine, K., Nishimori, Y., Ueda, T., Nakano, A., Sato, M.H., and Fukao, Y. (2014). Interactomics of Qa-SNARE in arabidopsis thaliana. Plant Cell Physiol. **55**: 781–789.

Futter, C.E., Pearse, A., Hewlett, L.J., and Hopkins, C.R. (1996). Multivesicular endosomes containing internalized EGF-EGF receptor complexes mature and then fuse directly with lysosomes. J. Cell Biol. **132**: 1011–1023.

Gao, C., Luo, M., Zhao, Q., Yang, R., Cui, Y., Zeng, Y., Xia, J., and Jiang, L. (2014). A Unique plant ESCRT component, FREE1, regulates multivesicular body protein sorting and plant growth. Curr. Biol. **24**: 2556–2563.

Gattolin, S., Sorieul, M., and Frigerio, L. (2011). Mapping of tonoplast intrinsic proteins in maturing and germinating Arabidopsis seeds reveals dual localization of embryonic TIPs to the tonoplast and plasma membrane. Mol. Plant **4**: 180–189.

Gattolin, S., Sorieul, M., Hunter, P.R., Khonsari, R.H., and Frigerio, L. (2009). In vivo imaging of the tonoplast intrinsic protein family in Arabidopsis roots. BMC Plant Biol **9**: 133.

Gavrin, A., Kaiser, B.N., Geiger, D., Tyerman, S.D., Wen, Z., Bisseling, T., and Fedorova, E.E. (2014). Adjustment of Host Cells for Accommodation of Symbiotic Bacteria: Vacuole Defunctionalization, HOPS Suppression, and TIP1g Retargeting in Medicago. Plant Cell **26**: 3809–22.

Goh, T., Uchida, W., Arakawa, S., Ito, E., Dainobu, T., Ebine, K., Takeuchi, M., Sato, K., Ueda, T., and Nakano, A. (2007). VPS9a, the common activator for two distinct types of Rab5 GTPases, is essential for the development of Arabidopsis thaliana. Plant Cell **19**: 3504–3515.

Gomez, L. and Chrispeels, M. (1993). Tonoplast and Soluble Vacuolar Proteins Are Targeted by Different Mechanisms. Plant Cell **5**: 1113–1124.

Graham, L.A., Flannery, A.R., and Stevens, T.H. (2003). Structure and Assembly of the Yeast V-ATPase. J. Bioenerg. Biomembr. **35**: 301–312.

Grebe, M., Xu, J., Möbius, W., Ueda, T., Nakano, A., Geuze, H.J., Rook, M.B., and Scheres, B. (2003). Arabidopsis sterol endocytosis involves actin-mediated trafficking via ARA6-positive early endosomes. Curr. Biol. **13**: 1378–1387.

Griffiths, G. and Simons, K. (1986). The trans Golgi network: sorting at the exit site of the Golgi complex. Science **234**: 438–43.

Grosshans, B.L., Ortiz, D., and Novick, P. (2006). Rabs and their effectors: achieving specificity in membrane traffic. Proc. Natl. Acad. Sci. U. S. A. **103**: 11821–7.

Guerra, F. and Bucci, C. (2016). Multiple Roles of the Small GTPase Rab7. Cells **5**: 34.

Guilliermond, A. (1941). The Cytoplasm of the Plant Cell.: 1–268.

Guilliermond, A. (1929). The Recent Development of our Idea of the Vacuome of Plant Cells. Am. J. Bot. **16**: 1–22.

Haas, T.J., Sliwinski, M.K., Martínez, D.E., Preuss, M., Ebine, K., Ueda, T., Nielsen, E., Odorizzi, G., and Otegui, M.S. (2007). The Arabidopsis AAA ATPase SKD1 is involved in multivesicular endosome function and interacts with its positive regulator LYST-INTERACTING PROTEIN5. Plant Cell **19**: 1295–1312.

Han, S.W., Alonso, J.M., and Rojas-Pierce, M. (2015). Regulator of Bulb Biogenesis1 (RBB1) is involved in vacuole bulb formation in Arabidopsis. PLoS One **10**: 1–20.

Hao, L., Liu, J., Zhong, S., Gu, H., and Qu, L.-J. (2016). AtVPS41-mediated endocytic pathway is essential for pollen tube-stigma interaction in Arabidopsis. Proc. Natl. Acad. Sci. U. S. A. **113**: 6307–6312.

Hara-Nishimura, I. (1998). Transport of Storage Proteins to Protein Storage Vacuoles Is Mediated by Large Precursor-Accumulating Vesicles. Plant Cell Online **10**: 825–836.

Hause, G., Samaj, J., Menzel, D., and Baluska, F. (2006). Fine Structural Analysis of Brefeldin A-Induced Compartment Formation After High-Pressure Freeze Fixation of Maize Root Epidermis: Compound Exocytosis Resembling Cell Plate Formation during Cytokinesis. Plant Signal. Behav. **1**: 134–9.

Herman, E.M. (2008). Endoplasmic reticulum bodies: solving the insoluble. Curr. Opin. Plant Biol. **11**: 672–679.

Herman, E.M., Li, X., Su, R.T., Larsen, P., Hsu, H., and Sze, H. (1994). Vacuolar-Type H+ -ATPases Are Associated with the Endoplasmic Reticulum and Provacuoles of Root Tip Cells. Plant Physiol. **106**: 1313–1324.

Hicks, G.R., Rojo, E., Hong, S., Carter, D.G., and Raikhel, N. V (2004). Geminating pollen has tubular vacuoles, displays highly dynamic vacuole biogenesis, and requires VACUOLESS1 for proper function. Plant Physiol. **134**: 1227–1239.

Higaki, T., Kutsuna, N., Okubo, E., Sano, T., and Hasezawa, S. (2006). Actin microfilaments regulate vacuolar structures and dynamics: Dual observation of actin microfilaments and vacuolar membrane in living tobacco BY-2 cells. Plant Cell Physiol. **47**: 839–852.

Hilling, B. and Amelunxen, F. (1985). On the development of the vacuole. II. Further evidence for endoplasmic reticulum origin. Eur J Cell Biol **38**: 195–200.

Hillmer, S., Viotti, C., and Robinson, D.G. (2012). An improved procedure for low-

temperature embedding of high-pressure frozen and freeze-substituted plant tissues resulting in excellent structural preservation and contrast. J. Microsc. **247**: 43–47.

Hirano, T., Munnik, T., and Sato, M.H. (2016). Inhibition of phosphatidylinositol 3,5-bisphosphate production has pleiotropic effects on various membrane trafficking routes in *Arabidopsis*. Plant Cell Physiol. **58**: pcw164.

Hofius, D., Schultz-Larsen, T., Joensen, J., Tsitsigiannis, D.I., Petersen, N.H.T., Mattsson, O., Jørgensen, L.B., Jones, J.D.G., Mundy, J., and Petersen, M. (2009). Autophagic Components Contribute to Hypersensitive Cell Death in Arabidopsis. Cell **137**: 773–783.

Hörtensteiner, S., Martinoia, E., and Amrhein, N. (1992). Reappearance of hydrolytic activities and tonoplast proteins in the regenerated vacuole of evacuolated protoplasts. Planta **187**: 113–121.

Hunter, P.R., Craddock, C.P., Di Benedetto, S., Roberts, L.M., and Frigerio, L. (2007). Fluorescent reporter proteins for the tonoplast and the vacuolar lumen identify a single vacuolar compartment in Arabidopsis cells. Plant Physiol. **145**: 1371–1382.

Ichino, T., Fuji, K., Ueda, H., Takahashi, H., Koumoto, Y., Takagi, J., Tamura, K., Sasaki, R., Aoki, K., Shimada, T., and Hara-Nishimura, I. (2014). GFS9/TT9 contributes to intracellular membrane trafficking and Flavonoid accumulation in Arabidopsis thaliana. Plant J. **80**: 410–423.

Iizuka, R., Yamagishi-Shirasaki, M., and Funatsu, T. (2011). Kinetic study of de novo chromophore maturation of fluorescent proteins. Anal. Biochem. **414**: 173–178.

Inoue, Y., Suzuki, T., Hattori, M., Yoshimoto, K., Ohsumi, Y., and Moriyasu, Y. (2006). AtATG genes, homologs of yeast autophagy genes, are involved in constitutive autophagy in Arabidopsis root tip cells. Plant Cell Physiol. **47**: 1641–1652.

Isono, E., Katsiarimpa, A., Müller, I.K., Anzenberger, F., Stierhof, Y.-D., Geldner, N., Chory, J., and Schwechheimer, C. (2010). The deubiquitinating enzyme AMSH3 is required for intracellular trafficking and vacuole biogenesis in Arabidopsis thaliana. Plant Cell **22**: 1826–1837.

Jia, T., Gao, C., Cui, Y., Wang, J., Ding, Y., Cai, Y., Ueda, T., Nakano, A., and Jiang, L. (2013). ARA7(Q69L) expression in transgenic Arabidopsis cells induces the formation of enlarged multivesicular bodies. J. Exp. Bot. **64**: 2817–2829.

Kalinowska, K., Nagel, M.-K., Goodman, K., Cuyas, L., Anzenberger, F., Alkofer, A., Paz-Ares, J., Braun, P., Rubio, V., Otegui, M.S., and Isono, E. (2015). Arabidopsis ALIX is required for the endosomal localization of the deubiquitinating enzyme AMSH3. Proc. Natl. Acad. Sci. U. S. A. **112**: E5543-51.

Karnahl, M., Park, M., Mayer, U., Hiller, U., and Jürgens, G. (2017). ER assembly of SNARE complexes mediating formation of partitioning membrane in *Arabidopsis* cytokinesis. Elife **6**: 1–10.

Kartner, N., Yao, Y., Bhargava, A., and Manolson, M.F. (2013). Topology, glycosylation and conformational changes in the membrane domain of the vacuolar H+-ATPase a subunit. J. Cell. Biochem. **114**: 1474–1487.

Karunakaran, S. and Fratti, R.A. (2013). The Lipid Composition and Physical

Properties of the Yeast Vacuole Affect the Hemifusion-Fusion Transition. Traffic **14**: 650–662.

Kato, T., Morita, M.T., Fukaki, H., Yamauchi, Y., Uehara, M., Niihama, M., and Tasaka, M. (2002). SGR2, a phospholipase-like protein, and ZIG/SGR4, a SNARE, are involved in the shoot gravitropism of Arabidopsis. Plant Cell **14**: 33–46.

Katsiarimpa, A., Anzenberger, F., Schlager, N., Neubert, S., Hauser, M.-T., Schwechheimer, C., and Isono, E. (2011). The Arabidopsis Deubiquitinating Enzyme AMSH3 Interacts with ESCRT-III Subunits and Regulates Their Localization. Plant Cell **23**: 3026–3040.

Katsiarimpa, A., Kalinowska, K., Anzenberger, F., Weis, C., Ostertag, M., Tsutsumi, C., Schwechheimer, C., Brunner, F., Hückelhoven, R., and Isono, E. (2013). The deubiquitinating enzyme AMSH1 and the ESCRT-III subunit VPS2.1 are required for autophagic degradation in Arabidopsis. Plant Cell **25**: 2236–52.

Katsiarimpa, A., Muñoz, A., Kalinowska, K., Uemura, T., Rojo, E., and Isono, E. (2014). The ESCRT-III-interacting deubiquitinating enzyme AMSH3 is essential for degradation of ubiquitinated membrane proteins in arabidopsis thaliana. Plant Cell Physiol. **55**: 727–736.

Keinath, N.F., Waadt, R., Brugman, R., Schroeder, J.I., Grossmann, G., Schumacher, K., and Krebs, M. (2015). Live Cell Imaging with R-GECO1 Sheds Light on flg22- and Chitin-Induced Transient [Ca2+]cyt Patterns in Arabidopsis. Mol. Plant **8**: 1188–1200.

Khmelinskii, A. et al. (2012). Tandem fluorescent protein timers for in vivo analysis of protein dynamics. Nat. Biotechnol. **30**: 708–714.

Kim, S., Naylor, S. a., and DiAntonio, a. (2012a). PNAS Plus: Drosophila Golgi membrane protein Ema promotes autophagosomal growth and function. Proc. Natl. Acad. Sci. **109**: E1072–E1081.

Kim, S., Wairkar, Y.P., Daniels, R.W., and DiAntonio, A. (2010). The novel endosomal membrane protein Ema interacts with the class C Vps-HOPS complex to promote endosomal maturation. J. Cell Biol. **188**: 717–734.

Kim, S.H., Kwon, C., Lee, J.H., and Chung, T. (2012b). Genes for plant autophagy: Functions and interactions. Mol. Cells **34**: 413–423.

Klinger, C.M., Klute, M.J., and Dacks, J.B. (2013). Comparative Genomic Analysis of Multi-Subunit Tethering Complexes Demonstrates an Ancient Pan-Eukaryotic Complement and Sculpting in Apicomplexa. PLoS One **8**: 1–15.

Klionsky, D.J. et al. (2008). Guidelines for the use and interpretation of assays for monitoring autophagy in higher eukaryotes.: 151–175.

Kobae, Y., Mizutani, M., Segami, S., and Maeshima, M. (2006a). Immunochemical Analysis of Aquaporin Isoforms in Arabidopsis Suspension-Cultured Cells. Biosci. Biotechnol. Biochem. **70**: 980–987.

Kobae, Y., Mizutani, M., Segami, S., and Maeshima, M. (2006b). Immunochemical analysis of aquaporin isoforms in Arabidopsis suspension-cultured cells. Biosci. Biotechnol. Biochem. **70**: 980–987.

Kolb, C., Nagel, M.-K., Kalinowska, K., Hagmann, J., Ichikawa, M., Anzenberger, F., Alkofer, A., Sato, M.H., Braun, P., and Isono, E. (2015). FYVE1 is essential for

vacuole biogenesis and intracellular trafficking in Arabidopsis. Plant Physiol. **167**: 1361–1373.

Krebs, M., Beyhl, D., Görlich, E., Al-Rasheid, K. a S., Marten, I., Stierhof, Y.-D., Hedrich, R., and Schumacher, K. (2010). Arabidopsis V-ATPase activity at the tonoplast is required for efficient nutrient storage but not for sodium accumulation. Proc. Natl. Acad. Sci. U. S. A. **107**: 3251–6.

Krebs, M. and Schumacher, K. (2013). Live Cell Imaging of Cytoplasmic and Nuclear Ca2+ Dynamics in Arabidopsis Roots. Cold Spring Harb. Protoc. **2013**: pdb.prot073031.

Kriegel, A. et al. (2015). Job Sharing in the Endomembrane System: Vacuolar Acidification Requires the Combined Activity of V-ATPase and V-PPase. Plant Cell **27**: tpc.15.00733.

Krüger, F., Krebs, M., Viotti, C., Langhans, M., Schumacher, K., and Robinson, D.G. (2013). PDMP induces rapid changes in vacuole morphology in Arabidopsis root cells. J. Exp. Bot. **64**: 529–540.

Kümmel, D. and Ungermann, C. (2014). Principles of membrane tethering and fusion in endosome and lysosome biogenesis. Curr. Opin. Cell Biol. **29**: 61–66.

Künzl, F., Früholz, S., Fäßler, F., Li, B., and Pimpl, P. (2016). Receptor-mediated sorting of soluble vacuolar proteins ends at the trans-Golgi network/early endosome. Nat. Plants **2**: 16017.

Lampropoulos, A., Sutikovic, Z., Wenzl, C., Maegele, I., Lohmann, J.U., and Forner, J. (2013). GreenGate - A novel, versatile, and efficient cloning system for plant transgenesis. PLoS One **8**: e83043.

Larson, E.R., Domozych, D.S., and Tierney, M.L. (2014). SNARE VTI13 plays a unique role in endosomal trafficking pathways associated with the vacuole and is essential for cell wall organization and root hair growth in arabidopsis. Ann. Bot. **114**: 1147–1159.

Lauber, M.H., Waizenegger, I., Steinmann, T., Schwarz, H., Mayer, U., Hwang, I., Lukowitz, W., Jürgens, G., Entwicklungsgenetik, L., Tübingen, U., Tübingen, D.-, and Republic, F. (1997). KNOLLE Protein Is a Cytokinesis-specific Syntaxin. **139**: 1485–1493.

Lee, H., Sparkes, I., Gattolin, S., Dzimitrowicz, N., Roberts, L.M., Hawes, C., and Frigerio, L. (2013). An Arabidopsis reticulon and the atlastin homologue RHD3-like2 act together in shaping the tubular endoplasmic reticulum. New Phytol. **197**: 481–489.

Lee, Y., Kim, E.-S., Choi, Y., Hwang, I., Staiger, C.J., Chung, Y.-Y., and Lee, Y. (2008a). The Arabidopsis phosphatidylinositol 3-kinase is important for pollen development. Plant Physiol. **147**: 1886–97.

Lee, Y.Y., Bak, G., Choi, Y., Chuang, W.-I., Cho, H.-T., and Lee, Y.Y. (2008b). Roles of phosphatidylinositol 3-kinase in root hair growth. Plant Physiol. **147**: 624–635.

Li, M., Rong, Y., Chuang, Y.-S., Peng, D., and Emr, S.D. (2015). Ubiquitin-Dependent Lysosomal Membrane Protein Sorting and Degradation. Mol. Cell **57**: 467–478.

Limpens, E., Ivanov, S., van Esse, W., Voets, G., Fedorova, E., and Bisseling, T. (2009). Medicago N2-fixing symbiosomes acquire the endocytic identity marker

Rab7 but delay the acquisition of vacuolar identity. Plant Cell **21**: 2811–2828.

Lipka, V., Kwon, C., and Panstruga, R. (2007). SNARE-ware: the role of SNARE-domain proteins in plant biology. Annu. Rev. Cell Dev. Biol. **23**: 147–174.

Löfke, C., Dünser, K., and Kleine-Vehn, J. (2013). Epidermal patterning genes impose non-cell autonomous cell size determination and have additional roles in root meristem size control. J. Integr. Plant Biol. **55**: 864–875.

Löfke, C., Dünser, K., Scheuring, D., and Kleine-Vehn, J. (2015). Auxin regulates SNARE-dependent vacuolar morphology restricting cell size. Elife **2015**.

Luo, Y., Scholl, S., Doering, A., Zhang, Y., Irani, N.G., Di, S., Neumetzler, L., Krishnamoorthy, P., Houtte, I. Van, and Mylle, E. (2016). V-ATPase-activity in the TGN / EE is required for exocytosis and recycling in Arabidopsis. Nat. plants **1**: 1–24.

Lupanga, U. (2017). A tale of two routes: The role of subunit a in targeting and regulation of the V-ATPase in Arabidopsis thaliana.

Lynch, A.M., Grana, T., Cox-Paulson, E., Couthier, A., Cameron, M., Chin-Sang, I., Pettitt, J., and Hardin, J. (2012). A Genome-wide functional screen shows MAGI-1 Is an L1CAM-Dependent Stabilizer of Apical Junctions in C. Elegans. Curr. Biol. **22**: 1891–1899.

Ma, B., Qian, D., Nan, Q., Tan, C., An, L., and Xiang, Y. (2012). Arabidopsis vacuolar H+-ATPase (V-ATPase) B subunits are involved in actin cytoskeleton remodeling via binding to, bundling, and stabilizing F-actin. J. Biol. Chem. **287**: 19008–19017.

Maîtrejean, M. and Vitale, A. (2011). How are tonoplast proteins degraded? Plant Signal. Behav. **6**: 1809–1812.

De Marchis, F., Bellucci, M., and Pompa, A. (2013). Unconventional pathways of secretory plant proteins from the endoplasmic reticulum to the vacuole bypassing the Golgi complex. Plant Signal. Behav. **8**: 1–5.

Martinoia, E., Meyer, S., De Angeli, A., and Nagy, R. (2012). Vacuolar Transporters in Their Physiological Context. Annu. Rev. Plant Biol **63**: 183–213.

Marty (1999). Plant vacuoles. Plant Cell **11**: 587–600.

Marty, F. (1978). Cytochemical studies on GERL, provacuoles, and vacuoles in root meristematic cells of Euphorbia. Proc. Natl. Acad. Sci. U. S. A. **75**: 852–856.

Matile, P. (1966). Enzyme der Vakuolen aus Wurzelzellen von Maiskeimlingen. Ein Beitrag zur funktioneilen Bedeutung der Vakuole bei der intrazellulären Verdauung. Z. Naturforschg. **21**: 871–878.

Matile, P. and Moor, H. (1968). Vacuolation: Origin and development of the lysosomal apparatus in root-tip cells. Planta **80**: 159–175.

van Meer, G., Voelker, D.R., and Feigenson, G.W. (2008). Membrane lipids: where they are and how they behave. Nat. Rev. Mol. Cell Biol. **9**: 112–124.

Merkulova, E.A., Guiboileau, A., Naya, L., Masclaux-Daubresse, C., and Yoshimoto, K. (2014). Assessment and optimization of autophagy monitoring methods in arabidopsis roots indicate direct fusion of autophagosomes with vacuoles. Plant Cell Physiol. **55**: 715–726.

Mesquita, J.F. (1969). Electron microscope study of the origin and development of the vacuoles in root-tip cells of Lupinus albus L. J. Ultrastruct. Res. **26**: 242–250.

Meyen, F.J.F. (1938). Neues System der Pflanzen-Physiologie.

Michaeli, S., Avin-Wittenberg, T., and Galili, G. (2014). Involvement of autophagy in the direct ER to vacuole protein trafficking route in plants. Front. Plant Sci. **5**: 134.

Milo, R. and Phillips, R. (2015). Cell Biology by the numbers (Garland Science).

Murray, J.T., Panaretou, C., Stenmark, H., Miaczynska, M., and Backer, J.M. (2002). Role of Rab5 in the recruitment of hVps34/p150 to the early endosome. Traffic **3**: 416–427.

Neubert, C. (2012). Assembly and quality control of the V- ATPase in Arabidopsis. Dissertation.

Neubert, C., Graham, L.A., Black-Maier, E.W., Coonrod, E.M., Liu, T.Y., Stierhof, Y.D., Seidel, T., Stevens, T.H., and Schumacher, K. (2008). Arabidopsis has two functional orthologs of the yeast V-ATPase assembly factor Vma21p. Traffic **9**: 1618–1628.

Niemes, S., Labs, M., Scheuring, D., Krueger, F., Langhans, M., Jesenofsky, B., Robinson, D.G., and Pimpl, P. (2010). Sorting of plant vacuolar proteins is initiated in the ER. Plant J. **62**: 601–614.

Niihama, M., Takemoto, N., Hashiguchi, Y., Tasaka, M., and Morita, M.T. (2009). ZIP genes encode proteins involved in membrane trafficking of the TGNPVC/Vacuoles. Plant Cell Physiol. **50**: 2057–2068.

Niihama, M., Uemura, T., Saito, C., Nakano, A., Sato, M.H., Tasaka, M., and Morita, M.T. (2005). Conversion of functional specificity in Qb-SNARE VTI1 homologues of Arabidopsis. Curr. Biol. **15**: 555–560.

Nováková, P. et al. (2014). SAC phosphoinositide phosphatases at the tonoplast mediate vacuolar function in Arabidopsis. Proc. Natl. Acad. Sci. U. S. A. **111**: 2818–23.

Paez Valencia, J., Goodman, K., and Otegui, M.S. (2016). Endocytosis and Endosomal Trafficking in Plants. Annu. Rev. Plant Biol. **67**: 309–335.

Paris, N., Stanley, C.M., Jones, R.L., and Rogers, J.C. (1996). Plant-Cells Contain 2 Functionally Distinct Vacuolar Compartments. Cell **85**: 563–572.

Park, M., Touihri, S., Müller, I., Mayer, U., and Jürgens, G. (2012). Sec1/Munc18 Protein Stabilizes Fusion-Competent Syntaxin for Membrane Fusion in Arabidopsis Cytokinesis. Dev. Cell **22**: 989–1000.

Pedrazzini, E., Caprera, A., Fojadelli, I., Stella, A., Rocchetti, A., Bassin, B., Martinoia, E., and Vitale, A. (2016). The Arabidopsis tonoplast is almost devoid of glycoproteins with complex N -glycans, unlike the rat lysosomal membrane. J. Exp. Bot.: erv567.

Pedrazzini, E., Komarova, N.Y., Rentsch, D., and Vitale, A. (2013). Traffic Routes and Signals for the Tonoplast. Traffic **14**: 622–628.

Peters, C., Bayer, M.J., Bühler, S., Andersen, J.S., Mann, M., and Mayer, a (2001). Trans-complex formation by proteolipid channels in the terminal phase of

membrane fusion. Nature **409**: 581–8.

Pfeffer, W. (1890). Zur Kenntnis der Plasmahaut und der Vacuolen. Abh. Math.-Phys. Kl. Ges. Wiss. Leipzig.

Powers, R.E., Wang, S., Liu, T.Y., and Rapoport, T.A. (2017). Reconstitution of the tubular endoplasmic reticulum network with purified components. Nature.

Ratajczak, R., Hinz, G., and Robinson, D.G. (1999). Localization of pyrophosphatase in membranes of cauliflower inflorescence cells. Planta **208**: 205–211.

Richter, S., Geldner, N., Schrader, J., Wolters, H., Stierhof, Y.-D., Rios, G., Koncz, C., Robinson, D.G., and Jürgens, G. (2007). Functional diversification of closely related ARF-GEFs in protein secretion and recycling. Nature **448**: 488–492.

Richter, S., Kientz, M., Brumm, S., Nielsen, M.E., Park, M., Gavidia, R., Krause, C., Voss, U., Beckmann, H., Mayer, U., Stierhof, Y.D., and Jürgens, G. (2014). Delivery of endocytosed proteins to the cell-division plane requires change of pathway from recycling to secretion. Elife **2014**.

Rink, J., Ghigo, E., Kalaidzidis, Y., and Zerial, M. (2005). Rab conversion as a mechanism of progression from early to late endosomes. Cell **122**: 735–749.

Rivera-Serrano, E.E., Rodriguez-Welsh, M.F., Hicks, G.R., and Rojas-Pierce, M. (2012). A Small Molecule Inhibitor Partitions Two Distinct Pathways for Trafficking of Tonoplast Intrinsic Proteins in Arabidopsis. PLoS One **7**: 1–11.

Rojo, E., Gillmor, C.S., Kovaleva, V., Somerville, C.R., and Raikhel, N. V. (2001). VACUOLELESS1 Is an Essential Gene Required for Vacuole Formation and Morphogenesis in Arabidopsis. Dev. Cell **1**: 303–310.

Rojo, E., Zouhar, J., Kovaleva, V., Hong, S., and Raikhel, N. V (2003). The AtC-VPS protein complex is localized to the tonoplast and the prevacuolar compartment in arabidopsis. Mol. Biol. Cell **14**: 361–9.

Ruthardt, N., Gulde, N., Spiegel, H., Fischer, R., and Emans, N. (2005). Four-dimensional imaging of transvacuolar strand dynamics in tobacco BY-2 cells. Protoplasma **225**: 205–215.

Rutherford, S. and Moore, I. (2002). The Arabidopsis Rab GTPase family: Another enigma variation. Curr. Opin. Plant Biol. **5**: 518–528.

Sanderfoot, A.A. (2001). Disruption of Individual Members of Arabidopsis Syntaxin Gene Families Indicates Each Has Essential Functions. Plant Cell Online **13**: 659–666.

Sanderfoot, A., Kovaleva, V., Bassham, D., and Raikhel, N. (2001). Interactions between syntaxins identify at least five SNARE complexes within the Golgi/prevacuolar system of the Arabidopsis cell. Mol. Biol. Cell **12**: 3733–3743.

Sanmartín, M., Ordóñez, A., Sohn, E.J., Robert, S., Sánchez-Serrano, J.J., Surpin, M.A., Raikhel, N. V, and Rojo, E. (2007). Divergent functions of VTI12 and VTI11 in trafficking to storage and lytic vacuoles in Arabidopsis. Proc. Natl. Acad. Sci. U. S. A. **104**: 3645–3650.

Di Sansebastiano, G.P., Paris, N., Marc-Martin, S., and Neuhaus, J.M. (2001). Regeneration of a lytic central vacuole and of neutral peripheral vacuoles can be visualized by green fluorescent proteins targeted to either type of vacuoles. Plant

Physiol. **126**: 78–86.

Scheuring, D., Löfke, C., Krüger, F., Kittelmann, M., Eisa, A., Hughes, L., Smith, R.S., Hawes, C., Schumacher, K., and Kleine-Vehn, J. (2016). Actin-dependent vacuolar occupancy of the cell determines auxin-induced growth repression. Proc. Natl. Acad. Sci. U. S. A. **113**: 452–7.

Scheuring, D., Viotti, C., Krüger, F., Künzl, F., Sturm, S., Bubeck, J., Hillmer, S., Frigerio, L., Robinson, D.G., Pimpl, P., Schumacher, K., and Ku, F. (2011). Multivesicular Bodies Mature from the Trans-Golgi Network/Early Endosome in Arabidopsis. Plant Cell **23**: 1–20.

Schindelin, J. et al. (2012). Fiji: an open-source platform for biological-image analysis. Nat Meth **9**: 676–682.

Schleiden, M.J. (1842). Grundzüge der wissenschaftlichen Botanik.

Schmid, B., Schindelin, J., Cardona, A., Longair, M., and Heisenberg, M. (2010). A high-level 3D visualization API for Java and ImageJ. BMC Bioinformatics **11**: 274.

Schumacher, K. (2014). pH in the plant endomembrane system-an import and export business. Curr. Opin. Plant Biol. **22**: 71–76.

Schwab, R., Ossowski, S., Riester, M., Warthmann, N., and Weigel, D. (2006). Highly Specific Gene Silencing by Artificial MicroRNAs in Arabidopsis[W][OA]. Plant Cell **18**: 1121–1133.

Segami, S., Makino, S., Miyake, A., Asaoka, M., and Maeshima, M. (2014). Dynamics of vacuoles and H+-pyrophosphatase visualized by monomeric green fluorescent protein in Arabidopsis: artifactual bulbs and native intravacuolar spherical structures. Plant Cell **26**: 3416–34.

Seguí-Simarro, J.M. and Staehelin, L.A. (2006). Cell cycle-dependent changes in Golgi stacks, vacuoles, clathrin-coated vesicles and multivesicular bodies in meristematic cells of Arabidopsis thaliana: A quantitative and spatial analysis. Planta **223**: 223–236.

Sheahan, M.B., Rose, R.J., and McCurdy, D.W. (2007). Actin-filament-dependent remodeling of the vacuole in cultured mesophyll protoplasts. Protoplasma **230**: 141–152.

Shimada, T., Koumoto, Y., Li, L., Yamazaki, M., Kondo, M., Nishimura, M., and Hara-Nishimura, I. (2006). AtVPS29, a putative component of a retromer complex, is required for the efficient sorting of seed storage proteins. Plant Cell Physiol. **47**: 1187–1194.

Shirakawa, M., Ueda, H., Shimada, T., Koumoto, Y., Shimada, T.L., Kondo, M., Takahashi, T., Okuyama, Y., Nishimura, M., and Hara-Nishimura, I. (2010). Arabidopsis Qa-SNARE SYP2 proteins localized to different subcellular regions function redundantly in vacuolar protein sorting and plant development. Plant J. **64**: 924–935.

Silady, R.A., Ehrhardt, D.W., Jackson, K., Faulkner, C., Oparka, K., and Somerville, C.R. (2008). The GRV2/RME-8 protein of Arabidopsis functions in the late endocytic pathway and is required for vacuolar membrane flow. Plant J. **53**: 29–41.

Singh, M.K., Krüger, F., Beckmann, H., Brumm, S., Vermeer, J.E.M., Munnik, T., Mayer, U., Stierhof, Y.D., Grefen, C., Schumacher, K., and J??rgens, G. (2014).

Protein delivery to vacuole requires SAND protein-dependent Rab GTPase conversion for MVB-vacuole fusion. Curr. Biol. **24**: 1383–1389.

Sniegowski, J.A., Lappe, J.W., Patel, H.N., Huffman, H.A., and Wachter, R.M. (2005). Base catalysis of chromophore formation in Arg96 and Glu222 variants of green fluorescent protein. J Biol Chem **280**: 26248–26255.

Spallanzani, L. (1776). Opuscoli di fisica animale e vegetabile.

Sparkes, I., Hawes, C., and Frigerio, L. (2011). FrontiERs: Movers and shapers of the higher plant cortical endoplasmic reticulum. Curr. Opin. Plant Biol. **14**: 658–665.

Stachowiak, J.C., Brodsky, F.M., and Miller, E. a (2013). A cost-benefit analysis of the physical mechanisms of membrane curvature. Nat. Cell Biol. **15**: 1019–27.

Starai, V.J., Hickey, C.M., and Wickner, W. (2008). HOPS proofreads the trans-SNARE complex for yeast vacuole fusion. Mol. Biol. Cell **19**: 2500–2508.

Strasser, B., Iwaszkiewicz, J., Michielin, O., and Mayer, A. (2011). The V-ATPase proteolipid cylinder promotes the lipid-mixing stage of SNARE-dependent fusion of yeast vacuoles. EMBO J. **30**: 4126–4141.

Strasser, R. (2014). Biological significance of complex N-glycans in plants and their impact on plant physiology. Front. Plant Sci. **5**: 1–6.

Strasser, R. (2016). The tonoplast – where sweetness is dispensable. J. Exp. Bot. **67**: 1607–16079.

Surpin, M., Zheng, H., Morita, M.T., Saito, C., Avila, E., Blakeslee, J.J., Bandyopadhyay, A., Kovaleva, V., Carter, D., Murphy, A., Tasaka, M., and Raikhel, N. (2003). The VTI family of SNARE proteins is necessary for plant viability and mediates different protein transport pathways. Plant Cell **15**: 2885–2899.

Swanson, S.J. and Jones, R.L. (1996). Gibberellic Acid Induces Vacuolar Acidification in Barley Aleurone. Plant Cell **8**: 2211–2221.

Taiz, L. (1992). The Plant Vacuole. J. Exp. Biol. **172**: 113–122.

Takáč, T., Pechan, T., Šamajova, O., Ovečka, M., Richter, H., Eck, C., Niehaus, K., and Šamaj, J. (2012). Wortmannin treatment induces changes in arabidopsis root proteome and Post-Golgi compartments. J. Proteome Res. **11**: 3127–3142.

Takáč, T., Pechan, T., Šamajová, O., and Šamaj, J. (2013). Vesicular trafficking and stress response coupled to PI3K inhibition by LY294002 as revealed by proteomic and cell biological analysis. J. Proteome Res. **12**: 4435–4448.

Thiam, A.R., Farese, R. V, and Walther, T.C. (2013). The biophysics and cell biology of lipid droplets. Nat. Rev. Mol. Cell Biol. **14**: 775–86.

Thompson, A.R., Doelling, J.H., Suttangkakul, A., and Vierstra, R.D. (2005). Autophagic nutrient recycling in Arabidopsis directed by the ATG8 and ATG12 conjugation pathways. Plant Physiol. **138**: 2097–2110.

Tinevez, J.-Y., Perry, N., Schindelin, J., Hoopes, G.M., Reynolds, G.D., Laplantine, E., Bednarek, S.Y., Shorte, S.L., and Eliceiri, K.W. (2016). TrackMate: an open and extensible platform for single-particle tracking. Methods.

Tominaga, M., Kimura, A., Yokota, E., Haraguchi, T., Shimmen, T., Yamamoto, K., Nakano, A., and Ito, K. (2013). Cytoplasmic Streaming Velocity as a Plant Size Determinant. Dev. Cell **27**: 345–352.

Twell, D. (2011). Male gametogenesis and germline specification in flowering plants. Sex. Plant Reprod. **24**: 149–160.

Uemura, T., Morita, M.T., Ebine, K., Okatani, Y., Yano, D., Saito, C., Ueda, T., and Nakano, A. (2010). Vacuolar/pre-vacuolar compartment Qa-SNAREs VAM3/SYP22 and PEP12/SYP21 have interchangeable functions in Arabidopsis. Plant J. **64**: 864–873.

Uemura, T. and Ueda, T. (2014). Plant vacuolar trafficking driven by RAB and SNARE proteins. Curr. Opin. Plant Biol. **22**: 116–121.

Uemura, T., Ueda, T., Ohniwa, R.L., Nakano, A., Takeyasu, K., and Sato, M.H. (2004). Systematic analysis of SNARE molecules in Arabidopsis: dissection of the post-Golgi network in plant cells. Cell Struct. Funct. **29**: 49–65.

Uemura, T., Yoshimura, S.H., Takeyasu, K., and Sato, M.H. (2002). Vacuolar membrane dynamics revealed by GFP-AtVam3 fusion protein. Genes to Cells **7**: 743–753.

Vermeer, J.E.M., Van Leeuwen, W., Tobeña-Santamaria, R., Laxalt, A.M., Jones, D.R., Divecha, N., Gadella, T.W.J., and Munnik, T. (2006). Visualization of PtdIns3P dynamics in living plant cells. Plant J. **47**: 687–700.

Vernoud, V. (2003). Analysis of the Small GTPase Gene Superfamily of Arabidopsis. Plant Physiol. **131**: 1191–1208.

Viotti, C. et al. (2010). Endocytic and secretory traffic in Arabidopsis merge in the trans-Golgi network/early endosome, an independent and highly dynamic organelle. Plant Cell **22**: 1344–1357.

Viotti, C. (2014). ER and vacuoles: never been closer. Front. Plant Sci. **5**: 20.

Viotti, C. et al. (2013). The endoplasmic reticulum is the main membrane source for biogenesis of the lytic vacuole in Arabidopsis. Plant Cell **25**: 3434–3449.

Voigt, B. et al. (2005). Actin-based motility of endosomes is linked to the polar tip growth of root hairs. Eur. J. Cell Biol. **84**: 609–621.

Vukašinović, N. and Žárský, V. (2016). Tethering Complexes in the Arabidopsis Endomembrane System. Front. cell Dev. Biol. **4**: 46.

Wang, J., Cai, Y., Miao, Y., Lam, S.K., and Jiang, L. (2009). Wortmannin induces homotypic fusion of plant prevacuolar compartments. J. Exp. Bot. **60**: 3075–3083.

Wang, P. and Hussey, P.J. (2015). Interactions between plant endomembrane systems and the actin cytoskeleton. Front. Plant Sci. **6**: 422.

Weigel, D. and Glazebrook, J. (2006). EMS Mutagenesis of Arabidopsis Seed. CSH Protoc. **2006**.

Welters, P., Takegawa, K., Emr, S.D., and Chrispeels, M.J. (1994). AtVPS34, a phosphatidylinositol 3-kinase of Arabidopsis thaliana, is an essential protein with homology to a calcium-dependent lipid binding domain. Proc. Natl. Acad. Sci. U. S. A. **91**: 11398–402.

Went, F.A.F.C. (1888). Die Vermehrung der normalen Vakuolen durch Teilung. Jahrb. Bot. **19**: 295–356.

Whitley, P., Hinz, S., and Doughty, J. (2009). Arabidopsis FAB1/PIKfyve proteins are essential for development of viable pollen. Plant Physiol. **151**: 1812–1822.

Wickner, W. (2010). Membrane fusion: five lipids, four SNAREs, three chaperones, two nucleotides, and a Rab, all dancing in a ring on yeast vacuoles. Annu. Rev. Cell Dev. Biol. **26**: 115–136.

Wiltshire, E.J. and Collings, D.A. (2009). New dynamics in an old friend: Dynamic tubular vacuoles radiate through the cortical cytoplasm of red onion epidermal cells. Plant Cell Physiol. **50**: 1826–1839.

Winter, V. and Hauser, M.T. (2006). Exploring the ESCRTing machinery in eukaryotes. Trends Plant Sci. **11**: 115–123.

Wolfenstetter, S., Wirsching, P., Dotzauer, D., Schneider, S., and Sauer, N. (2012). Routes to the Tonoplast: The Sorting of Tonoplast Transporters in Arabidopsis Mesophyll Protoplasts. Plant Cell **24**: 215–232.

Woollard, A.A. and Moore, I. (2008). The functions of Rab GTPases in plant membrane traffic. Curr. Opin. Plant Biol. **11**: 610–619.

Xie, Z. and Klionsky, D.J. (2007). Autophagosome formation: core machinery and adaptations. Nat Cell Biol **9**: 1102–1109.

Xing, S., Mehlhorn, D.G., Wallmeroth, N., Asseck, L.Y., Kar, R., Voss, A., Denninger, P., Schmidt, V.A.F., Schwarzländer, M., Stierhof, Y.-D., Grossmann, G., and Grefen, C. (2017). Loss of GET pathway orthologs in *Arabidopsis thaliana* causes root hair growth defects and affects SNARE abundance. Proc. Natl. Acad. Sci.: 201619525.

Xu, N., Gao, X.Q., Zhao, X.Y., Zhu, D.Z., Zhou, L.Z., and Zhang, X.S. (2011). Arabidopsis AtVPS15 is essential for pollen development and germination through modulating phosphatidylinositol 3-phosphate formation. Plant Mol. Biol. **77**: 251–260.

Yamauchi, Y., Fukaki, H., Fujisawa, H., and Tasaka, M. (1997). Mutations in the SGR4, SGR5 and SGR6 loci of Arabidopsis thaliana alter the shoot gravitropism. Plant Cell Physiol. **38**: 530–5.

Yamazaki, M., Shimada, T., Takahashi, H., Tamura, K., Kondo, M., Nishimura, M., and Hara-Nishimura, I. (2008). Arabidopsis VPS35, a retromer component, is required for vacuolar protein sorting and involved in plant growth and leaf senescence. Plant Cell Physiol. **49**: 142–156.

Yan, Y. and Backer, J.M. (2007). Regulation of class III (Vps34) PI3Ks. Biochem. Soc. Trans. **35**: 239–41.

Yano, K., Hattori, M., and Moriyasu, Y. (2007). A novel type of autophagy occurs together with vacuole genesis in miniprotoplasts prepared from tobacco culture cells. Autophagy **3**: 215–221.

Zhang, X., Henriques, R., Lin, S.-S., Niu, Q.-W., and Chua, N.-H. (2006). Agrobacterium-mediated transformation of Arabidopsis thaliana using the floral dip method. Nat. Protoc. **1**: 641–646.

Zheng, H. and Staehelin, L.A. (2011). Protein storage vacuoles are transformed into lytic vacuoles in root meristematic cells of germinating seedlings by multiple, cell type-specific mechanisms. Plant Physiol. **155**: 2023–2035.

Zheng, J., Han, S.W., Munnik, T., and Rojas-Pierce, M. (2014a). Multiple vacuoles in impaired tonoplast trafficking3 mutants are independent organelles. Plant Signal. Behav. **9**: e972113.

Zheng, J., Han, S.W., Rodriguez-Welsh, M.F., and Rojas-Pierce, M. (2014b). Homotypic Vacuole Fusion Requires VTI11 and Is Regulated by Phosphoinositides. Mol. Plant **7**: 1026–1040.

Zirkle, C. (1937). The Plant Vacuole. Bot. Rev. **III**: 01–30.

Zirkle, C. (1932). Vacuoles in primary meristems. Zeitschrift f{ü}r Zellforsch. und Mikroskopische Anat. **16**: 26–47.

Zouhar, J., Rojo, E., and Bassham, D.C. (2009). AtVPS45 is a positive regulator of the SYP41/SYP61/VTI12 SNARE complex involved in trafficking of vacuolar cargo. Plant Physiol. **149**: 1668–78.

Acknowledgements

First of all, I would like to thank Prof. Dr. Karin Schumacher for her excellent supervision of my work and my development as a scientist. She always had time to discuss results and future experiments but also knew how to challenge me when I was making myself a home in my comfort zone. Moreover, I could travel to so many cities, Madrid, Lecce, Kyoto and Prague, to present my work to other scientists. For these memorable journeys I am very thankful, too.

Second of all, I would like to thank Prof. Dr. Jan Lohmann, Prof. Dr. Marius Lemberg and Prof Dr. Alexis Maizel for being very helpful and supportive TAC members over the years. In addition, I thank Prof. Dr. Thomas Greb for being my fourth examiner. Furthermore, I would like to thank Dr. Sebastian Wolf for his support in planning and conducting my EMS mutagenesis screen as well as discussing strategies to identify interesting mutants.

I am very grateful to Dr. Melanie Krebs, who had great influence on me and my work. At any time she was interested to discuss experiments with me and was very helpful when I needed any advice. Also, I want to thank her for proofreading my results part. It was always such a great pleasure to work and chat with her.

A huge "Thank You!" to Dr. Anne Kriegel for the outstanding years we had together with a lot of ups and a few downs. Her permanent good mood was annoyingly contagious and sometimes saved my day. One highlight that I will never forget is from our lab-retreat where she told us about the famous "Angstbohnen" during a hiking trip.

I also want to thank Ines Steins for taking so great care of all lab-related things which had nothing to do with science. She was always incredibly kind no matter how often I asked her how many holidays I have left.

Many thanks to Jana Christin Askani for being such an organized and hardworking student as well as proofreading the results part. Due to her endurance the HOPS project became a project at all and is now a great story.

When it comes to important lab members I must not forget Fabian Fink, a kind friend who was always so helpful, especially when I had to harvest dozens of trays in the blazing heat of the green house during summer time. Together with Stefan Scholl (Thank you too, pHteven!) we spent an amazing time at the bench with a lot of funny music and even more jokes.

My heartfelt thanks to Dr. Nana Keinath for so much kindness and support during her time in the lab as well as her invaluable career advices.

During my time as a PhD student I enjoyed to supervise many students and there are a few who left a lasting impression on me, too. First and foremost I would like to express my gratitude to Leonie Martin, a great student, hardworking HiWi and unbelievably kind and inspiring person. Another great student was Ailisa Blum, with amazing skills when it came to the preparation of two-cell-stage Arabidopsis embryos and motivating her supervisor.

From the past and present I want to thank all people of the AG Schumacher: Dr. Corrado Viotti, Dr. Stefan Hillmer, Dr. David Scheuring, Dr. Zaida Andrés, Dr. Upendo Lupanga, Dr. Raina Waadt, Dr. Esther Jawurek, Dr. Christoph Neubert, Beate Schöfer, Steffi Gold, Barbara Jesenofski, Görkem Patir, Simon Delang, Philipp Bellon and Oliver Artz.

This last section is dedicated to my family and friends:

I am deeply grateful to my dear parents and brother who were always patient with me and supported me with their love and advice especially when times were rough.

The same holds true for my girlfriend, Johanna, who not only proofread every word of this thesis and helped me to shorten overly complicated sentences, but also endured me and my moods patiently almost every day.

Last but not least, many thanks to Sebastian Sorge and Benjamin Trageser for being great friends since we met during the Bachelor studies.